
Measurements of Atmospheric Turbulence Effects on Tail Rotor Acoustics

Martin J. Hagen, Gloria K. Yamauchi,
David B. Signor, and Marianne Mosher

September 1994



National Aeronautics and
Space Administration

Measurements of Atmospheric Turbulence Effects on Tail Rotor Acoustics

Martin J. Hagen, California Polytechnic State University, San Luis Obispo, California
Gloria K. Yamauchi, David B. Signor, and Marianne Mosher, Ames Research Center,
Moffett Field, California

September 1994



National Aeronautics and
Space Administration

Ames Research Center
Moffett Field, California 94035-1000

Measurements of Atmospheric Turbulence Effects on Tail Rotor Acoustics

MARTIN J. HAGEN,* GLORIA K. YAMAUCHI, DAVID B. SIGNOR, AND MARIANNE MOSHER

Ames Research Center

Summary

Results from an outdoor hover test of a full-scale Lynx tail rotor are presented. The investigation was designed to further the understanding of the acoustics of an isolated tail rotor hovering out-of-ground effect in atmospheric turbulence, without the effects of the main rotor wake or other helicopter components. Measurements include simultaneous rotor performance, noise, inflow, and far-field atmospheric turbulence. Results with grid-generated inflow turbulence are also presented. The effects of atmospheric turbulence ingestion on rotor noise are quantified. In contradiction to current theories, increasing rotor inflow and rotor thrust were found to increase turbulence ingestion noise.

This is the final report of Task 13A—Helicopter Tail Rotor Noise, of the NASA/United Kingdom Defense Research Agency cooperative Aeronautics Research Program.

Notation

a	speed of sound, m/s
A	autocorrelation coefficient
b	number of blades (4)
c	blade chord (0.18 m)
C_T/σ	rotor thrust coefficient divided by rotor solidity, rotor thrust/ $R\rho(\Omega R)^2 bc$
dBA	A-weighted Sound Pressure Level (referenced to 20 μ Pa)
d	separation distance between rods in the turbulence-generating grid (7.6 cm)
M_{tip}	rotor tip Mach number, $\Omega R/a$
N	number of data samples per hot-film time record (2048)
OASPL	Over-all Sound Pressure Level, dB (referenced to 20 μ Pa)

O_r	observer radial distance nondimensionalized by R
R	rotor radius (1.105 m)
u'	rms turbulence velocity, $\sqrt{\frac{1}{N} \sum_{i=1}^N (U_i - \bar{u})^2}$, m/s
\bar{u}	average velocity, $\frac{1}{N} \sum_{i=1}^N U_i$, m/s
U	velocity measured by hot-film probe, m/s
U_∞	atmospheric wind speed measured by cup anemometer, m/s
V_{rot}	inflow velocity measured by pitot probe, m/s
x	distance downstream from grid, cm
x_0	position of maximum grid-generated turbulence ($5 \leq \frac{x_0}{d} \leq 15$), cm
z	height above ground, m
z_{hub}	height of rotor hub above ground, (6.1 m)
Δt	hot-film signal sample spacing (0.0125 s)
γ	atmospheric wind direction measured from rotor axis (positive, clockwise looking down), deg
Λ	eddy length, m
Ω	rotor rotational speed, rad/s
ρ	air density, kg/m ³
τ	autocorrelation delay, $\tau = j\Delta t$, s
θ	rotor collective pitch, deg

*California Polytechnic State University, San Luis Obispo, California.

Subscripts

f	denotes far-field hot-film parameter
n	denotes near-field hot-film parameter

Introduction

Turbulence ingestion noise is an important source of helicopter noise, particularly in the absence of impulsive noise sources (ref. 1), and can be a significant source of broadband noise when a helicopter is in hover or vertical ascent (ref. 2). Turbulence ingestion noise is generated when a rotor blade interacts with atmospheric turbulence or the turbulent wakes of preceding blades (ref. 2). For a lifting, hovering rotor, however, the wake of the preceding blade will convect out of the path of the following blades, leaving the atmospheric turbulence as a major contributor to the sound radiated by a hovering rotor. The manner in which ingested atmospheric turbulence is manifested as rotor noise is explained as follows. A lifting rotor accelerates the air and stretches atmospheric eddies passing through the rotor. The velocity fluctuations in the eddies cause fluctuations of the local pressure, lift, and drag of the rotor blades. These unsteady forces are the acoustic source of atmospheric turbulence ingestion noise. A blade-eddy interaction produces broadband noise. Multiple interactions with a single eddy produce correlated disturbances. The blades of a hovering tail rotor can chop an atmospheric eddy over 500 times. The exact number of chops depends on the number of blades, rotor rpm, eddy size, and rotor inflow velocity. For a hovering main rotor, the blades chop a single atmospheric eddy 10 to 200 times. Acoustic spectra from a tail rotor chopping atmospheric turbulence will be narrow band. Acoustic spectra from a main rotor chopping atmospheric turbulence will contain both narrow band and broadband components.

In order to determine the effects of atmospheric turbulence ingestion on rotor acoustics, numerous characteristics of the atmosphere must be measured simultaneously, in addition to the rotor-radiated noise. To date, no single experiment has included acquisition of all the necessary but difficult measurements. Unlike the controlled environment in a wind tunnel, the atmosphere is inherently unsteady and at times unstable. A large number of assorted sensors located at various altitudes would be required to thoroughly document the changing atmospheric conditions.

Complete characterization of the atmospheric turbulence was beyond the scope of this experiment. The objective of this experimental investigation was to correlate a few basic features of atmospheric turbulence with the sound radiated by a full-scale Lynx tail rotor in hover. This report presents measurements of simultaneous rotor performance, noise, inflow, and far-field atmospheric turbulence. Results with grid-generated turbulence are also presented. Some of these results have been documented in reference 3; however, the present report covers a wider range of test conditions and includes two additional microphone locations.

In addition, this is the final report of Task 13A—Helicopter Tail Rotor Noise, of the NASA/United Kingdom Defense Research Agency cooperative Aeronautics Research Program. A brief summary of the program is provided in appendix A.

The authors thank Prof. A. R. George of Cornell University for his invaluable advice and recommendations regarding the analysis of the data. The support of this test program by Dr. Charles Smith of NASA Ames is also appreciated.

Description of Experiment

Model

A full-scale Lynx tail rotor was used for this investigation. This rotor consists of four constant-chord, untwisted blades (fig. 1). Nominal rotor speed was 1850 rpm. The rotor hub has conventional flapping and feathering hinges and was installed 6.1 m above the ground. The tail rotor was mounted on the NASA Ames Tail Rotor Test Rig (TRTR), shown in figure 2, at the Outdoor Aerodynamic Research Facility. The rotor drive motor, drive shaft, and right-angle gearbox are mounted inside the horizontal boom, which is mounted on the main vertical support. Additional information about the TRTR and Lynx rotor can be found in references 4 and 5.

Rotor Measurements

A strain-gauge balance was used to measure the mean rotor thrust, torque, and vertical force. The balance was mounted between the horizontal support tube and the gearbox mounting bracket (fig. 3). Rotor balance accuracy is shown in table 1. Balance data were acquired using a low-pass filter set at 10 Hz. Mean blade flapwise bending moments were measured at 30%, 40% and 70% radial

Table 1. Rotor balance accuracy

	Combined loading condition	
	Positive thrust and torque	Negative thrust and torque
Calculated thrust accuracy (% maximum thrust)	± 1	± 2
Calculated torque accuracy (% maximum torque)	± 2	± 4

positions (fig. 1). Bending moment data were acquired using a low-pass filter set at 100 Hz. Mean balance and blade bending moment data were computed from 15 s of data.

Flow Measurements

The rotor inflow was measured with a single-element hot-film anemometer and a pitot-static probe. Data from the pitot-static probe were low-pass filtered with the filter set at 10 Hz; averaged values were computed from 15 s of data. The hot-film and pitot-static probe were mounted on a tower and remained fixed relative to the rotor. The hot-film was horizontal and parallel to the rotor plane.

A 3.6- by 3.6-m turbulence-generating grid was installed upstream of the rotor for several runs. The grid consisted of 1.3 cm diameter rods arranged in 7.6 cm square cells. The grid changed the character of the ingested turbulence by introducing small-scale turbulence. Figure 4 shows the locations of the hot-film probe and grid with respect to the rotor. According to Hinze (ref. 6) and Batchelor (ref. 7), grid-generated turbulence becomes homogeneous in a uniform freestream for $x/d \geq 10$, where x is the distance downstream from the grid and d is the cell width. At $x/d = 10$, maximum turbulence velocity is expected. The hot-film and rotor plane were positioned at $x/d = 9.5$ and $x/d = 16.7$, respectively. The flow into the grid is recognized as non-uniform since the rotor inflow has spanwise variations in axial velocity. However, the methods of Batchelor (ref. 7) were used to position the grid upstream of the rotor; therefore, the turbulence at the rotor plane is assumed to be approximately homogeneous. Figure 5 shows the installation of the grid.

A second single-element hot-film was mounted on a tower located upstream and to the side of the tail rotor. The hot-film was horizontal and parallel to the rotor plane. The

probe was 4.7 m above the ground and remained fixed. This probe was used to measure the atmospheric turbulence in the far-field. Figure 6 shows the location of the far-field tower with respect to the rotor.

Constant temperature anemometer bridges powered the hot-film probes. The anemometer signals were linearized. The near-field probe signal was low-pass filtered (filter set at 40 Hz) to remove the blade passage frequency before being digitized. A dynamic signal analyzer with an anti-aliasing filter was used to digitize the data from both probes. Figure 7 shows the hot-film data acquisition system. No averaging or windowing was used. The data were recorded for 25.6 s at 80 samples/s. The probes were calibrated before the experiment, but not before every run. A second calibration performed after the completion of the experiment revealed very little change in the probes' conversion constants and offsets. The data were reduced using the average of the results from the two calibrations.

Atmospheric wind speed and direction were measured using a cup anemometer and a weather vane located on a third tower roughly 46 m upstream of the rotor, 55 m from the rotor axis, and 10 m above the ground. Additionally, the weather station at Naval Air Station Moffett Field recorded several atmospheric parameters hourly. Measurements included air temperature, wind speed, wind direction, barometric pressure, humidity, and cloud conditions. These measurements were recorded 12.8 m above sea level, at a location approximately 1500 m south-east of the Outdoor Aerodynamic Research Facility.

Acoustic Measurements

Five microphones were typically used to acquire acoustic data. The microphones were placed in an array about the rotor at distances of 2.5, 4.5, and 10 rotor radii away from the hub. The microphone locations are tabulated in table 2 and shown in figure 6. All but one of the microphones (mic 8) were at the same height as the rotor. Acoustic foam was used to substantially reduce reflected rotor noise off the ground, near-field tower, and TRTR (figs. 2 and 5). Wind screens were placed over each microphone to reduce wind-generated noise.

Table 2. Microphone locations

Microphone	O_r	γ (deg)	$(z-z_{hub})/R$
2	2.5	225	0.0
6	4.5	270	0.0
8	2.5	180	-1.77
9	4.5	0	0.0
11	10.0	0	0.0

All microphones were calibrated daily using a piston-phone. Two microphone calibrations were recorded each day. The conversion constants from the two recorded calibrations were then averaged; this averaged value served as the conversion constant for each microphone for that particular day. The error associated with this method is on the order of ± 1 dB. The data were recorded for 30 s using a 14-track FM tape recorder with a tape speed of 30 ips, giving a frequency range of 20 kHz. Spectra from the acoustic time histories were generated by a dynamic signal analyzer using the rotor 1/rev as an external trigger. The fluctuation in rotor speed was less than 0.2 percent of full-scale, that is, no more than 2 to 4 rpm. All acoustic data were reduced using a time record of 0.256 s per average (approximately 8 revolutions per average based on a nominal rpm of 1850), a span of 3.125 kHz, and a bandwidth of 5.86 Hz. Each spectrum represents 25 averages (no overlap) of power spectra made with a Hanning window. A schematic of the acoustic data acquisition set-up is shown in figure 8.

The measurements of rotor noise include gear noise from the right-angle gearbox located immediately upstream of the rotor hub. Gear noise, as described by Dale (ref. 8), appears in the spectra as discrete frequency spikes at some sidebands of the integer harmonics of the gear mesh frequency (37/rev) modulated by the rotor blade passage frequency ($k*37 \pm n*4$ per rev, k and n are integers). The probable cause is modulation of the gear mesh frequency by quasi-periodic disturbances on the rotor blades. Noise was not produced at all sidebands. Gear noise was removed from the spectra for sidebands of the first three

harmonics of the gear mesh frequency. The following procedure was used to remove the gear noise. A low-order polynomial curve was fit through the 80% dB levels of a noise spectrum. Next, frequencies ($k*37 \pm n*4$ per rev) contaminated with gear noise were identified. Amplitudes at these contaminated frequencies were removed if the amplitude exceeded the polynomial curve fit value. The amplitude was then replaced with an interpolated value using frequencies (with amplitudes less than the curve fit value) adjacent to the contaminated frequency. This procedure generally reduced amplitudes at three or four spectral lines centered at the contaminated frequency. Figure 9 shows a typical correction to an acoustic spectrum.

Configuration and Test Envelope

Data acquisition times were planned for morning hours when the wind speed at the site was low, generally below 2 m/s (with some data acquired between 2 and 6 m/s), in order to simulate hover and obtain high quality acoustic data. The low winds led to generally low turbulence intensities.

The test configuration consisted of the TRTR with the microphone array and the near-field and far-field towers. Data were also acquired prior to the installation of the towers. In addition, the turbulence grid was installed for some of the data acquisition runs. The ranges of test parameters are shown in table 3.

Table 3. Ranges of test parameters

Configuration:	No tower; no grid	Tower; no grid	Tower; grid
Rotor collective pitch, θ	-9° to 15°	3° to 15°	3° to 15°
C_T/σ	-0.0296 to 0.0789	0.0038 to 0.0758	0.0041 to 0.0760
Rotor tip Mach number, M_{tip}	0.52 to 0.63	0.52 to 0.62	0.62
Atmospheric wind direction, γ	*	-28° to 59°	-17° to 59°
Atmospheric wind speed, U_∞ (m/s)	0.0 to 2.67	0.38 to 5.74	1.27 to 3.57
Far-field eddy length, Λ_f (m)		0.8 to 12.8	1.0 to 14.1
Average inflow velocity, \bar{u}_n (m/s)		2.24 to 8.71	2.84 to 11.40

*Includes conditions for which $U_\infty \leq 1.0$ m/s regardless of atmospheric wind direction and conditions for which $-30^\circ \leq \gamma \leq 60^\circ$ regardless of atmospheric wind speed.

Data Quality

In analyzing the large amount of acoustic and turbulence data, every effort was made to exclude questionable data. Criteria for excluding data and quality of the data are discussed below.

Atmospheric Measurements

The data were limited to those conditions acquired with wind directions of $-30^\circ \leq \gamma \leq 60^\circ$ (fig. 6) for the runs in which the near-field tower was present. This avoided blockage effects from the near-field tower and the TRTR on the rotor and hot-film measurements. For those runs conducted prior to the near-field tower installation, the data were limited to the same wind direction envelope or those conditions in which the ambient wind speed was less than 1.0 m/s, regardless of wind direction.

In an attempt to compute near- and far-field transverse eddy lengths, a second movable probe was installed at each tower. The movable probe was then traversed upward and away from the fixed probe. Data were typically acquired at seven discrete probe separation distances (0–3 m) while holding rotor conditions constant. The transverse eddy length was then computed from the cross-correlation coefficients of the two probes at each tower. This method proved to be inadequate for calculating an accurate transverse eddy length. Data recorded simultaneously from a rake of probes at each tower would have been preferred. Therefore, for this paper, data from only the fixed probe is presented for each tower and no estimate of transverse eddy length is presented.

The longitudinal eddy length at each tower was obtained from respective fixed probe autocorrelations. Autocorrelations were only performed on time histories which appeared stochastic. The autocorrelation is defined as

$$A_j = \frac{1}{N-j} \sum_{i=1}^{N-j} (U_i - \bar{u})(U_{i+j} - \bar{u})$$

The eddy lengths are defined by

$$\Lambda_n = \bar{u}_n \Delta t \sum_{j=0}^{q-1} \frac{A_{nj}}{A_{n0}}$$
$$\Lambda_f = \frac{\bar{u}_f}{\cos \gamma} \Delta t \sum_{j=0}^{q-1} \frac{A_{fj}}{A_{f0}}$$

where q is the lowest integer for which A_q is negative. The far-field eddy lengths were computed using the $(\cos \gamma)$ term to account for wind direction. Figure 10 presents a typical hot-film time history and the corresponding normalized autocorrelation and frequency spectrum. As stated earlier, the probe signals were

recorded for 25.6 s. A time record of perhaps thirty minutes for the far-field probes would have been better for determining if the flow was stationary, since the far-field contains turbulent eddies which are complex, large-scale structures. Because the time record lengths were insufficient to obtain statistically accurate autocorrelations and integral times, the integral scales presented should be considered only as rather coarse estimates.

In addition, a higher sampling rate for the hot-film probes would have been preferable, especially for the near-tower probe. Since the probe signals were sampled at 80 samples/s and the near-tower signal was low-pass filtered at 40 Hz before being recorded, the frequency content beyond 40 Hz is not available. This prevents a determination of the turbulence spectrum above 40 Hz and precludes a determination of the filter effect on the turbulence level or length scale. In a similar experiment, however, Paterson and Amiet (ref. 9) found the error in overall rms turbulence level due to low-pass filtering to be less than 10%. Instrumentation limitations dictated that only a fixed number of samples (2,048) could be acquired per data point, leading to the chosen compromise between record length and sample rate.

As a means of verifying the rotor inflow velocity measured by the hot-film, a pitot-static probe was placed in the rotor inflow. The probe was slightly (4%) closer to the blade tip than the hot-film (fig. 4). Rotor inflow surveys performed by Simonich, et al. (ref. 10) indicate that the magnitude of the inflow velocity increases with distance from the center of rotation to roughly 60% of the blade radius, so the probe is expected to experience somewhat higher inflow velocities than the hot-film. Figure 11 supports this; the slope of the curve is greater than unity, and therefore the inflow velocity measured by the hot-film is considered consistent with that measured by the pitot-static probe.

Acoustic Measurements

As stated earlier, data are limited to a narrow range of wind directions for those runs in which the near-field tower was present to minimize the influence of the near-field tower on the rotor inflow. However, acoustic reflections from the tower were a concern since not all of the tower could be treated with foam and the foam does not completely eliminate reflections. Data were acquired early in the experimental program without the tower installed. These data are limited to the same wind direction envelope, or to those conditions in which the ambient wind speed was less than 1.0 m/s regardless of wind direction. Comparisons are made of acoustic spectra with and without the tower in figure 12. Rotor and atmospheric conditions are similar, but not exact. Note

that the rotor rpm is 1.5% higher for the condition with the tower present. All microphone spectra, especially the in-plane (mic 6) microphone spectrum, exhibit slightly higher floors at the higher frequencies in addition to higher blade passage harmonic peaks with the tower present. Because of the inherent difficulty in obtaining closely matched atmospheric conditions with and without the tower present, only one comparison is possible among the data set to assess the influence of the tower. Hence, the effect of the tower cannot be quantified precisely; however, figures 12(d) and 12(e) show that the presence of the tower does not dramatically change the character of the acoustic spectra of the on-axis microphones, where turbulence ingestion noise is most dominant. The off-axis microphones were positioned closer to the tower which may account for the larger difference in the spectra with the tower present. We conclude, then, that the turbulence ingestion noise measured by the on-axis microphones is not significantly influenced by the presence of the tower.

Another structure which may have disrupted the inflow to the rotor is the horizontal rotor support structure shown in figure 5. For positive thrust, the horizontal support is immediately upstream of the rotor. The support could generate disturbances in the flow which produce noise similar to noise produced by ingested atmospheric turbulence. This possibility was investigated by looking at the acoustic spectra for a low wind, negative thrust condition, and a corresponding positive thrust condition. For a negative thrust condition, the horizontal support is in the wake of the rotor rather than in the inflow. Figures 13(a) and 13(b) show the spectra for microphones 2 and 8 located 45° from the rotor axis for $C_T/\sigma = \pm 0.01$, respectively. These data were acquired prior to the installation of the near-field tower. Data from the on-axis microphones were contaminated by the wake of the rotor flowing past the microphones. Although there are differences in the magnitudes of some of the peaks, the character of the spectra are similar for the positive and negative thrust conditions. Thus even when the horizontal support is not in the rotor inflow, turbulence ingestion noise exists. Since there are no other structures which could disturb the inflow of the rotor for a negative thrust condition, the turbulence ingestion noise is attributed to atmospheric turbulence. Therefore, any turbulence ingestion noise caused by the horizontal support for positive thrust conditions is reasoned to be small compared to the atmospheric turbulence ingestion noise.

Data consistency and repeatability are important qualities of any experiment but can be difficult to achieve in an outdoor test. The atmospheric conditions usually remained fairly steady during a run, although the occurrence of a wind gust or changes in ambient noise levels during data acquisition were possible. The

degree of data repeatability is shown in figures 14–16. Figures 14(a) and 14(b) present spectra from a single run for an off-axis (mic 2) and on-axis (mic 9) microphone, respectively. Figures 15 and 16 are similar to figure 14 except for differing rotor conditions. Runs for this experiment typically lasted 20 to 30 minutes. Rotor rotational velocity was adjusted between data point acquisitions as necessary to maintain a specified value of M_{tip} , and is the only rotor operating control which was varied in a given run. As the legends on figures 14–16 indicate, the atmospheric wind speed and direction change slightly within a run. The on-axis microphone results are very repeatable. The off-axis microphone shows more variation, especially at the higher frequencies. Figures 14–16 thus represent the amount of scatter to be expected in the acoustic spectra.

Results and Discussion

Data characterizing the atmospheric turbulence are discussed first. The sensitivity of the acoustic measurements to basic characteristics of the atmospheric turbulence are then discussed. Appendix B provides descriptions of the parameters tabulated in appendix C. The results tabulated in appendix C are for the range of test conditions shown in table 3.

Atmospheric Measurements

Quantifying the magnitude of turbulence ingestion noise for this test requires detailed knowledge of the atmospheric turbulence structure, which is very complicated. The structure depends upon the wind profile and upstream conditions, terrain roughness and shear, fluxes of moisture and thermal energy, cloud cover, and other factors. Depending on these factors the turbulence velocities can be moderately or severely anisotropic (especially in stable, stratified conditions). In addition, inhomogeneous large eddy structures often include significant intermittency (refs. 11 and 12). Finally, the rotor distorts the environmental turbulence (ref. 13).

The upstream wind conditions at the Outdoor Aerodynamic Research Facility generally begin over San Francisco Bay. From the shoreline, the upstream wind flows over a kilometer of terrain consisting of long grass with some shrubs, isolated trees, and berms. Although the atmosphere appeared to be stably stratified at higher altitudes, the atmosphere at the rotor height was likely neutral or slightly unstable during the testing periods due to mechanical mixing from terrain roughness. The general character of the turbulence at any location in the atmospheric boundary layer is determined by the stability of the atmosphere relative to the turbulence

generated by shear stress. If the atmosphere is neutral to slightly buoyant the turbulence will be similar to that in an aerodynamic boundary layer. Following Panofsky and Dutton (ref. 14), atmospheric buoyancy was checked for conditions during this test by estimating the Turner classes of the flow from the Moffett Field weather and solar data to find the approximate Monin-Obukhov lengths and Richardson numbers. The range of estimated Monin-Obukhov lengths was approximately -10 to -25 m and the range of Richardson numbers was approximately -0.06 to -0.25 , indicating near neutral to slightly unstable conditions. This was consistent with the hot-film measurements and indicates that the assumption of isotropic turbulence is a reasonable first approximation far from the rotor.

Far-field— Far-field turbulence length scales are shown in figure 17 as a function of the atmospheric wind speed. The wind speed component measured by the far-field probe has been adjusted for wind direction in order to arrive at the total magnitude. The eddy lengths at the lowest wind speeds are low because there is little mechanical mixing of the atmospheric boundary layer. The eddy lengths initially increase with increasing wind speed, but become less dependent on wind speed at moderate wind speeds. At higher wind speeds, the length scales are of the order of the measurement height (4.7 m), consistent with length scales that are expected for a neutral to slightly buoyant boundary layer.

The measured atmospheric rms turbulence velocities, u'_f , corresponding to the eddy lengths in figure 17 are shown in figure 18. The primary cause for u'_f increasing with wind speed is development of the boundary layer with increasing wind speed.

Near-field— The stretching of the eddies as they are accelerated through the rotor is shown in figure 19. The grid was not installed for these conditions. The amount of eddy stretching is one measure of how the rotor alters the surrounding atmospheric turbulence prior to ingesting the turbulence. The length and speed of the ingested eddies determines the number of times the eddy will be chopped by the rotor blades. While the ratio of near- to far-field longitudinal eddy lengths for most points shown in figure 19 is greater than unity, a significant number are not. This is because the measurements were made in an Eulerian sense, not Lagrangian—individual eddies were not tracked as they traveled from the far-field and became distorted by the rotor. Therefore, the eddies entering the rotor should in general be longer than the far-field eddies, but there can be exceptions. Length scales of the ingested eddies are shown in figure 20 as a function of the inflow velocity. The scatter in the data is large; no discernible

effects of M_{tip} or rotor collective pitch on eddy length were observed.

Figure 21 shows ingested rms turbulence velocity as a function of atmospheric wind speed. The rms turbulence velocity increases with increasing atmospheric wind speed for the range of this experiment. There is no discernible effect of rotor operating condition on rms turbulence velocity.

Acoustic Measurements

Acoustics results are shown for the five observer positions (table 2 and fig. 6). The primary measurement locations, microphones 9 and 11, were on the rotor axis 4.5 and 10 rotor radii from the rotor, respectively. Measurements at these locations show the greatest effect of atmospheric turbulence ingestion. Microphones 2 and 8 were placed 45° from the rotor axis; microphone 6 was placed 90° (in-plane) from the rotor axis. Background noise measurements were typically at least 20 dB below the acoustic measurements of the rotor.

General characteristics of the measured noise are discussed first. Next, atmospheric effects on measured noise are presented. Variations in ingested rms turbulence velocity, ingested eddy length, atmospheric wind speed, and inflow velocity are investigated to determine their influence on the rotor noise. Effects of varying rotor thrust are then discussed, followed by a discussion of the effects of inserting a turbulence-generating grid upstream of the rotor.

General characteristics— Figure 9 shows an averaged spectrum from microphone 9 with and without the gear noise removed. The mean ambient wind for this condition is essentially zero; however, zero mean ambient wind does not preclude the existence of turbulence. The near-field tower was not installed for this condition. Several aspects of this spectrum are characteristic of the noise measured in this experiment. The spectrum contains numerous distinct rotor blade passage harmonics rising above the broadband noise. For a hovering rotor, two mechanisms which produce peaks at the blade passage frequency harmonics are steady loading noise and turbulence ingestion noise. Peaks from steady loading noise diminish with increasing frequency much faster than in this example. The peaks in the measured spectrum are very narrow at the lower frequencies and increase in width as the frequency increases; this is a characteristic of turbulence ingestion noise (ref. 15). Another possible cause of widening peaks is unsteadiness in the rotor speed; however, as explained earlier, the rotor speed was found to be very steady. Also, the peaks identified with the gear noise do not widen at the higher frequencies.

Therefore, the widening of the peaks in the spectrum is most likely caused by turbulence ingestion. Additional spectra from microphone 9 acquired for various rotor and atmospheric conditions exhibit similar characteristics. In contrast, spectra from microphone 6 (in-plane location) exhibit different characteristics, as shown in figure 22(a). The amplitudes of the first 2 or 3 blade passage harmonics are larger and can be attributed to thickness noise. Amplitudes diminish quickly for the first 3 or 4 harmonics; generally, levels of all harmonics above about the fourth are lower at this location. The existence of distinct and broadening peaks in the spectra out to 2 kHz indicate some noise is radiating from the turbulence ingestion; however, this noise is about 40 dB below the fundamental and thus contributes little to the sound level in the plane of the rotor either in OASPL or dBA measurements. The spectrum shown in figure 22(b) is from microphone 11, the other on-axis microphone. Figures 22(c) and 22(d) represent microphones 2 and 8, respectively, which are 45° from the rotor axis. Figures 22(b)–(d) are similar in character to the microphone 9 spectra.

Atmospheric turbulence effects– Variations in atmospheric turbulence are expected to cause changes in sound measurements when turbulence ingestion is a major sound-producing mechanism. The structure of the inflow turbulence incident on the rotor will influence the nature of the blade lift fluctuations and thus the radiated sound. If the time records of the probes were long enough to obtain a statistical average and short enough for the turbulence characteristics to be quasi-stationary, the near- and far-field measured turbulence characteristics should be clearly related. As shown in figures 17–21, however, much scatter exists in the turbulence measurements. In this section, therefore, acoustic measurements will be related to estimates of turbulence characteristics made in the near-field.

When a rotor interacts with atmospheric turbulence, the turbulence produces fluctuating pressures on the rotor blades leading to fluctuating lift and drag. These pressure fluctuations radiate away from the rotor as sound. Most likely, the fluctuating lift will be greater than the fluctuating drag. If this happens, more sound will radiate perpendicular to the blade in the direction of the rotor axis than parallel to the blade close to the plane of the rotor. Also, higher rms turbulence velocities are expected to produce higher pressure fluctuations and higher radiated sound levels than lower rms turbulence velocities would produce. Figure 23 shows the effects of rms turbulence velocity in the near-field, u'_n , on the sound radiated by the rotor for two values of M_{tip} . The turbulence-generating grid was not present. The metric dBA was chosen over OASPL because dBA gives more weight to frequencies between 1 and 4 kHz. Turbulence ingestion noise in this

frequency range, where humans are most sensitive, is more significant than thickness or steady loading noise. There appears to be little or no trend with rms turbulence velocity for any of the microphones for either M_{tip} , especially the in-plane microphone (fig. 23(c)). At this location, thickness noise dominates the radiated noise and is manifested mainly in the first few rotor harmonics. The off-axis microphones (figs. 23(a) and (b)) tend to have more scatter per collective than the on-axis microphones (figs. 23(d) and (e)). Although figure 23 does not reveal a significant correlation of sound level with u'_n , power spectra can reveal more detailed information. Figure 24 shows spectra from two points in figure 23 with a collective pitch of 7°, $M_{tip} = 0.52$, and two different values of u'_n . All other conditions for the two points are similar, except the atmospheric wind speed. The wind speeds are 0.7 and 3.9 m/s corresponding to the smaller and larger values of u'_n , respectively. The on-axis microphones (figs. 24(d) and (e)) show that with higher u'_n , the amplitude of the lower frequency rotor blade passage harmonics is greater than for the lower u'_n case; the amplitudes of the higher frequency harmonics are about the same. Also, with higher rms turbulence velocities, the broadband noise floor increases, about 2 dB at the lower frequencies and about 5 dB at the higher frequencies shown. The off-axis microphones (figs. 24(a) and (b)) show similar features as the on-axis microphones, but to a lesser degree. The in-plane microphone (fig. 24(c)) does not appear to be significantly influenced by the change in u'_n .

Eddy length may also affect the turbulence ingestion noise produced by a rotor. The rotor will chop a long eddy for a longer period than a short eddy, which could produce more tonal noise. Figure 25 shows measurements from all microphones for $M_{tip} = 0.52$ and 0.62; no grid was present. For a fixed collective, no distinct effect of eddy length is observed. Levels increase with increasing rotor collective pitch. Scatter in the data per collective is greatest for the off-axis microphones (figs. 25(a) and (b)), followed by the on-axis microphones (figs. 25(d) and (e)) and in-plane microphone (fig. 25(c)). Figure 26 shows spectra from two points in figure 25 with 7° collective pitch, $M_{tip} = 0.52$, and two values of the near-field eddy length, Λ_n . All other conditions are similar. No significant difference between the two spectra is observed for any of the microphones. Because of the high rotational velocity of this tail rotor (blade passage frequencies of 102–124 Hz) and the ingested eddy size (2 to 20 m), the rotor is expected to chop the eddy 80 to 800 times. Chopping an eddy 80 times is sufficient to produce fairly coherent sound; increasing the number of chops above 80 may have insignificant effect on the coherence. Thus noise produced by the tail rotor chopping of the longest eddies

may be only slightly more coherent than the noise produced by the rotor chopping the shortest eddies in this experiment.

The atmospheric wind speed is the other basic characteristic of the atmospheric turbulence that was measured. The rms turbulence velocities exhibit some correlation with wind speed (fig. 21). Figure 27 shows acoustic measurements for $M_{tip} = 0.52$ and 0.62 without the grid present. Results are similar to those observed in figure 23. Again, levels increase with increasing rotor collective pitch.

Rotor inflow– Measured sound levels correlate more strongly with the rotor inflow velocity than with any other parameter or atmospheric quantity measured. At microphone locations on the rotor axis and at 45° off the rotor axis, sound levels measured in dBA increase with increasing rotor inflow velocity without the grid present (fig. 28). In the plane of the rotor (fig. 28(c)), some trend of increasing sound levels with increasing inflow velocity occurs; however, the slope is not as steep as for the other microphone locations. Also, in the rotor plane where thickness noise radiates strongly the tip Mach number influences the sound level more than at the other microphone locations. The strong dependence on rotor inflow velocity suggests that an obstruction to the inflow might be causing noise by producing disturbances that the rotor chops. This possibility was eliminated by examining sound data acquired with the rotor thrusting in the opposite direction (negative C_T/σ). The previous discussion concerning figure 13 shows that no obstruction contributed significantly to the sound levels for the off-axis microphones.

Rotor thrust– Increasing rotor thrust will obviously increase the loading noise of the rotor; however, according to current theories (refs. 13 and 16), pressure disturbances on the rotor blade (and hence radiated sound) due to turbulence ingestion are independent of the steady lift of the rotor blade. In these theories, increasing rotor thrust increases the eddy length distortion, producing longer longitudinal eddies. With the same energy in the eddy distributed over a longer eddy, the expected effect on noise is to produce more blade-to-blade correlation. The total acoustic energy remains the same and is more concentrated at the blade passage harmonics because of the increase in blade intersections with a given eddy. In all the measurements examined above, however, the sound level in dBA increased with increasing rotor collective. As explained earlier, the metric dBA was chosen to emphasize the frequency range of turbulence ingestion noise rather than steady loading noise. The collective pitch directly influences the rotor C_T/σ , a more direct measure of how the rotor interacts with the air.

Figure 29 shows sound pressure level measured in dBA as a function of C_T/σ . The grid was not present. For the microphones most influenced by turbulence ingestion noise (locations out of the rotor plane), the sound level increases with increasing C_T/σ . In the plane of the rotor the sound levels increase with increasing C_T/σ , but not as steeply as at the locations out of the rotor plane. Figure 30 shows spectra from two points in figure 29 for $M_{tip} = 0.62$. Spectra are shown for collectives of 3° and 15° corresponding to C_T/σ of 0.004 and 0.076, respectively. Except at the in-plane microphone location (fig. 30(c)), amplitudes of the low-order blade passage harmonics increase 5 to 10 dB from low to high thrust. The increase is less at the in-plane location. Loading noise dominates the low-order harmonics at the out-of-plane locations and thickness noise dominates at the in-plane location. Amplitudes of higher frequency harmonics increase 10 to 15 dB at all locations with increased thrust. Measurements in dBA (fig. 29) also increase 10 to 15 dB. The broadband floor is a few dB higher at the higher frequencies. These observations indicate turbulence ingestion as the mechanism associated with the higher harmonics.

Turbulence grid– A grid in a fluid stream creates eddies with length scales on the order of the grid spacing. These eddies decay far downstream of the grid. In this test, the rotor was in the near downstream region of the grid where the small, grid-generated eddies had partially decayed but the larger atmospheric eddies had not yet been significantly affected by the introduction of the grid-generated small-scale turbulence. Inserting the grid changed the turbulence ingested by the rotor. Although the exact nature of this change was not documented, the grid added small-scale turbulence to the existing atmospheric turbulence. This change in turbulence is expected to increase the broadband floor of the noise spectra in the higher end of the spectrum examined in this investigation. Figure 31 shows measurements for $M_{tip} = 0.62$ with and without the grid present for $\theta = 3^\circ, 7^\circ$, and 15° . Except in the plane of the rotor, noise measurements with the grid present are consistently higher. Measured values of u'_n are not available for conditions with the grid, but Batchelor (ref. 7) provides an equation for estimating the rms turbulence velocity downstream of a grid:

$$\left(\frac{\bar{u}}{u'}\right)^2 = 134 \left(\frac{x}{d} - \frac{x_0}{d}\right)$$

The calculated rms turbulence velocities range from 0.067 to 0.26, 0.12 to 0.36, and 0.19 to 0.53 for $\theta = 3^\circ, 7^\circ$, and 15° , respectively. The error in estimating x_0/d has been included in these calculations, i.e., $5 \leq x_0/d \leq 15$. Figure 32 shows spectra, with and without the grid, representing two points in figure 31 for a collective pitch of 3° . For microphones out of the rotor plane, amplitudes

of the rotor blade passage harmonics are 3 to 5 dB higher for most harmonics when the grid is present. The amplitude of the broadband floor is also higher with the grid, about 3 dB at low frequencies and increasing with increasing frequency.

Concluding Remarks

This investigation examined some of the effects of atmospheric turbulence ingestion on hovering tail rotor acoustics. The presentation of dBA levels and power spectra provide overall and detailed information concerning changes in radiated sound due to various atmospheric parameters. Because of the large scatter in the turbulence data, these changes cannot be precisely quantified. The data, however, clearly indicate a strong dependence of measured sound levels on the rotor inflow velocity and thrust level. This trend is somewhat unexpected and warrants further investigation.

Specific remarks about the presented data are as follows:

1. The atmosphere is assumed to be isotropic far from the rotor.
2. Far-field rms turbulence velocities generally increase with increasing atmospheric windspeed.
3. The maximum longitudinal eddy length stretching ratio is approximately nine.
4. Near-field rms turbulence velocity increases with atmospheric windspeed. There is no discernable effect of rotor operating condition on the rms turbulence velocity.
5. The widening of peaks with increasing frequency in the measured spectrum is attributed to turbulence ingestion noise.
6. Noise measurements made along the rotor axis indicate that with higher near-field rms turbulence velocity, the amplitude of the lower frequency rotor blade passage harmonics is about the same. Also, with higher near-field rms turbulence velocity, the broadband noise floor increases, about 2 dB at the lower frequencies and about 5 dB at the higher frequencies.
7. No distinct effect of eddy length on measured noise was observed.
8. No distinct effect of atmospheric windspeed on measured noise was observed.
9. Sound levels measured in dBA increase with increasing rotor inflow velocity and rotor thrust. Current theories do not account for the influence of rotor thrust on turbulence ingestion noise.
10. The addition of small scale turbulence caused by installing a grid upstream of the rotor increased the sound levels measured in dBA for locations out of the rotor plane. Also, for locations out of the rotor plane, the amplitude of the broadband floor in the measured spectrum is higher with the grid.

References

1. George, A. R.: Helicopter Noise: State-of-the-Art. *J. Aircraft*, vol. 15, no. 11, Nov. 1978, pp. 707–715.
2. Janakiram, R. D.: Aerodynamics of Rotorcraft. AGARD Report No. 781, Nov. 1990.
3. Signor, D. B.; Yamauchi, G. K.; Mosher, M.; Hagen, M. J.; and George, A. R.: Effects of Ingested Atmospheric Turbulence on Measured Tail Rotor Acoustics. AHS 48th Annual Forum, Washington D. C., June 1992.
4. Signor, D.; Yamauchi, G.; Smith, C.; and Hagen, M.: Performance and Loads Data from an Outdoor Hover Test of a Lynx Tail Rotor. NASA TM-101057, June 1989.
5. Gregory, N.; and Wilby, P. G.: NPL 9615 and NACA 0012, A Comparison of Aerodynamic Data. NASA CP-1261, 1973.
6. Hinze, J. O.: Turbulence, McGraw Hill, Inc., 1975, pp. 259-277.
7. Batchelor, G. K.: The Theory of Homogeneous Turbulence, Cambridge University Press, 1967, pp. 133-168.
8. Dale, A. K.: Gear Noise and The Sideband Phenomenon. ASME Design Engineering Tech. Conf., Cambridge, Mass., Oct. 7–10, 1984.
9. Paterson, R. W.; and Amiet, R. K.: Noise of a Model Helicopter Rotor Due to Ingestion of Turbulence. NASA CR-3213, Nov. 1979.
10. Simonich, J. C.; Schlinker, R. H.; and Amiet, R. K.: Experimental Assessment of Helicopter Rotor Turbulence Ingestion Noise in Hover. NASA CR-181792, June 1989.
11. Thomson, D. W.; and Henderson, H. W.: Definition of Local Atmospheric Attractors using Measurements Made with Surface-based Remote Sensing Systems. First Experimental Chaos Conference, Arlington, Va., Oct. 1–3, 1991.
12. Wilson, D. K.: Propagation of Sound Through the Fluctuating Atmosphere. Second International Congress on Recent Developments in Air- & Structure-Borne Sound and Vibration, Auburn, Ala., March 4–6, 1992.
13. Simonich, J. C.; Amiet, R. K.; Schlinker, R. H.; and Greitzer, E. M.: Helicopter Rotor Noise Due to Ingestion of Atmospheric Turbulence. NASA CR-3973, May 1986.
14. Panofsky, H. A.; and Dutton, J. A.: Atmospheric Turbulence, John Wiley & Sons, 1984, pp. 87, 139-140.
15. Homicz, G. F.; and George, A. R.: Broadband and Discrete Frequency Radiation for Subsonic Rotors. *Journal of Sound and Vibration*, vol. 36, no. 2, 1974, pp. 151–177.
16. Amiet, R. K., Noise Produced by Turbulent Flow Into a Rotor: Theory Manual for Noise Calculation. NASA CR-181788, June 1989.
17. Owen, T. B.; and Beauchamp, A. R.: Aero-Acoustic Measurements on a Lynx Tail Rotor in the RAE 24ft Wind Tunnel. RAE-TM-Aero-1972 (X84-70842), July 1983.
18. Norman, T. R.; and Yamauchi, G. K.: Full-Scale Investigation of Aerodynamic Interactions Between a Rotor and A Fuselage. AHS 47th Annual Forum, Phoenix, Ariz., May 1991.

Appendix A—Program Summary

In 1980 the Royal Aircraft Establishment (RAE) and NASA Ames Research Center initiated a joint effort to study helicopter tail rotor noise. The program was designated Task 13A—Helicopter Tail Rotor Noise, and was part of the larger NASA/United Kingdom Ministry of Defence (MOD) Procurement Executive Joint Aeronautical Programme. The RAE was renamed the Defense Research Agency (DRA) in 1992.

The helicopter tail rotor noise program was to consist of a series of tests using a full-scale Lynx tail rotor, culminating with a test in the NASA Ames 40- by 80-Foot Wind Tunnel including both a Bell 412 main rotor and the Lynx tail rotor operating simultaneously but independently.

The first test was conducted by the RAE in their 24-Foot Wind Tunnel (ref. 17) with the primary objective of documenting the baseline acoustics and performance of the Lynx tail rotor in forward flight. A secondary objective was to compare acoustic data obtained in the planned Ames 40- by 80-Foot Wind Tunnel with acoustic data from the RAE 24-Foot Wind Tunnel. The RAE test matrix and microphone positions were specified to match the future 40- by 80-Foot Wind Tunnel tests. The effects of rotor operating conditions on noise were determined, but data scatter prohibited reliable determination of polar noise distributions.

The second test, which consisted of operating the Lynx tail rotor in hover, was conducted at the NASA Ames Outdoor Aerodynamic Research Facility. Test objectives included measuring isolated rotor performance in hover and exploration of the effects of atmospheric turbulence

on rotor acoustics. The performance and loads data from the second test are presented in reference 4. The effects of ingested atmospheric turbulence on tail rotor acoustics are documented in reference 3. The microphone locations for this second test were based on the locations used in the first test. Data were collected over the ranges of collective pitch and rotor rotational velocity that were to be used in the subsequent 40- by 80-Foot Wind Tunnel test. The primary acoustics conclusion is that atmospheric turbulence is the dominant noise source near the rotor axis for a hovering tail rotor.

The third test in the program consisted of a Bell 412 main rotor operating in the 40- by 80-Foot Wind Tunnel. The primary test objective was to measure the full-scale rotor/fuselage aerodynamic interactions. The measured interactions are documented in reference 18. This test was necessary so that the aerodynamics of the main rotor with fuselage could be understood prior to adding the tail rotor to the test configuration.

The last two proposed tests were to be the isolated Lynx tail rotor in the 40- by 80-Foot Wind Tunnel, and the Bell 412 main rotor with the Lynx tail rotor operating in the 40- by 80-Foot Wind Tunnel.

The last two tests were not conducted. The decision was made to terminate Task 13A due to the helicopter tail rotor noise program being more than ten years in duration, changing priorities within the National Full-Scale Aerodynamic Complex (NFAC), the backlog of tests scheduled for the NFAC, and the scheduled acoustic modification of the 40- by 80-Foot Wind Tunnel test section.

Appendix B—Description of Measured Parameters

Parameter	Description	Units
Coll	collective pitch	deg
Config	A : near-field tower not installed, grid not installed B : near-field tower installed, grid not installed C : near-field tower installed, grid installed	
Cq/s	torque coefficient divided by rotor solidity	
Ct/s	thrust coefficient divided by rotor solidity	
Datm (= γ)	wind direction relative to the rotor axis	deg
EL f	far-field eddy length derived from hot-film measurement	m
EL n	near-field eddy length derived from hot-film measurement	m
F 30*	flapwise bending moment, $r/R=0.30$	N-m
F 40*	flapwise bending moment, $r/R=0.40$	N-m
F 70*	flapwise bending moment, $r/R=0.70$	N-m
Flap**	blade flap angle	deg
FM	figure of merit	
Hum	relative humidity	%
M2 dBA	A-weighted sound pressure level measured at microphone 2	dBA
M2 SPL	overall sound pressure level measured at microphone 2	dB
M6 dBA	A-weighted sound pressure level measured at microphone 2	dBA
M6 SPL	overall sound pressure level measured at microphone 6	dB
M8 dBA	A-weighted sound pressure level measured at microphone 8	dBA
M8 SPL	overall sound pressure level measured at microphone 8	dB
M9 dBA	A-weighted sound pressure level measured at microphone 9	dBA
M9 SPL	overall sound pressure level measured at microphone 9	dB
M11 dBA	A-weighted sound pressure level measured at microphone 11	dBA
M11 SPL	overall sound pressure level measured at microphone 11	dB
Mtip	tip Mach number	
Opaque	level of sky opaqueness: 1-minimum, 10-maximum	
Patm	barometric pressure	bar
PDT	Pacific daylight time	hr:min
Rho	air density	kg/m ³
RPM	rotor angular speed	rev/min
Sky Cov	amount of cloud coverage: 1-minimum, 10-maximum	
Temp	ambient temperature	°C
U f	far-field average wind speed measured by hot-film	m/s
U n	near-field average wind speed measured by hot-film	m/s
U' f	far-field turbulent velocity measured by hot-film	m/s
U' n	near-field turbulent velocity measured by hot-film	m/s
Vatm (= V_{∞})	far-field wind speed measured by cup anemometer	m/s
Vrot	rotor inflow velocity measured by pitot-static probe	m/s
*	positive, upper surface in compression	
**	positive, blade flaps toward gearbox	

Appendix C—Measured Parameters

Mtip RPM Config	Coll Ct/s Cq/s	FM Flap Vrot	F 30 F 40 F 70	Vatm Datm Rho	Patm Hum Temp	U n U' n EL n	U f U' f EL f	Sky Cov Opaque PDT	M2 dBA			M6 dBA			M2 SPL			M6 SPL		
									M8 dBA	M9 dBA	M11 dBA	M2 dBA	M8 dBA	M9 dBA	M11 dBA	M2 SPL	M8 SPL	M11 SPL		
RUN 27																				
0.60 1736 A	PT 8 15 0.0744 0.01324	0.49 2.12	-25.2 -13.8 -4.7	1.88 40 1.28	1.02 35 5.7				105.6 104.3	98.0 104.5 98.6		110.8 109.3	107.4 107.0 101.8							
RUN 27																				
0.63 1823 A	PT 10 15 0.0746 0.01332	0.49 1.65	-26.8 -14.2 -4.9	2.18 24 1.28	1.02 35 5.7				106.3 104.8	101.9 104.8 99.1		113.3 109.2	112.8 107.6 102.1							
RUN 28																				
0.52 1503 A	PT 3 9 0.0359 0.00540	0.41 1.48	-36.8 -21.7 -3.7	1.45 1 1.28	1.02 35 5.6				96.3 95.9	87.4 94.5 89.2		98.5 99.7	104.7 96.7 91.9							
RUN 28																				
0.56 1619 A	PT 5 9 0.0353 0.00538	0.40 1.30	-42.4 -24.0 -2.8	1.49 40 1.28	1.02 35 5.6				100.0 100.4	90.8 98.7 92.9		103.1 103.8	104.3 100.9 95.6							
RUN 28																				
0.60 1736 A	PT 7 9 0.0349 0.00537	0.39 1.33	-46.9 -25.7 -2.7	1.87 41 1.28	1.02 35 5.6				100.3 100.0	94.5 99.6 94.0		106.0 104.8	105.1 102.4 97.0							
RUN 28																				
0.63 1820 A	PT 9 9 0.0340 0.00535	0.38 1.30	-50.2 -27.1 -3.1	2.55 39 1.28	1.02 35 5.1				91.9 110.5	98.9 100.7 95.3		98.2 114.2	110.3 103.6 98.3							

Mtlp RPM Config	Coll C/s Cq/s	FM Flap Vrot	F 30 F 40 F 70	Vatm Datm Rho	Patm Hum Temp	U n U' n EL n	U f U' f EL f	Sky Cov Opaque PDT	M2 dBA M8 dBA	M6 dBA M9 dBA M11 dBA	M2 SPL M8 SPL	M6 SPL M9 SPL M11 SPL
RUN 29	PT 3											
0.52	4	0.10	-46.8	2.53	1.02					85.4		103.6
1503	0.0085	0.37	-27.8	-1	35				91.6	88.9	95.4	92.6
A	0.00245		-2.7	1.28	5.2				90.7	83.3	96.1	86.8
RUN 29	PT 5											
0.56	4	0.11	-52.1	2.67	1.02					88.7		103.8
1620	0.0087	0.41	-29.9	-12	35				93.8	88.7	101.0	93.8
A	0.00243		-2.4	1.28	5.2				93.4	85.0	99.1	88.8
RUN 29	PT 7											
0.60	4	0.12	-57.0	2.63	1.02					94.1		106.1
1735	0.0094	0.47	-31.7	-24	35				95.3	92.3	104.0	97.2
A	0.00247		-2.1	1.28	5.2				94.0	86.8	98.6	90.0
RUN 32	PT 3											
0.52	-9	0.28	-61.9	0.60	1.02					89.3		106.2
1509	-0.0293	0.02	-38.7	-111	38				97.4	N/A	100.3	N/A
A	0.00580		-3.2	1.27	6.7				97.7	82.5	100.5	111.8
RUN 32	PT 5											
0.56	-9	0.28	-68.4	0.43	1.02					91.5		106.8
1623	-0.0294	0.04	-41.3	-114	38				97.4	90.8	104.8	113.1
A	0.00582		-2.7	1.27	6.7				98.0	82.6	102.9	111.4
RUN 32	PT 7											
0.60	-9	0.28	-75.7	0.37	1.02					95.6		106.9
1739	-0.0296	0.00	-44.2	-155	38				102.0	93.4	107.5	114.3
A	0.00589		-2.3	1.27	7.2				102.1	84.8	103.1	114.0

Mtip RPM Config	Coll Ct/s Cq/s	FM Flap Vrot	F 30 F 40 F 70	Vatm Datm Rho	Patm Hum Temp	U n U' n EL n	U f U' f EL f	Sky Cov Opaque PDT	M2 dBA M8 dBA	M6 dBA M9 dBA M11 dBA	M2 SPL M8 SPL	M6 SPL M9 SPL M11 SPL
RUN 32	PT 9											
0.62	-9	0.28	-78.4	0.77	1.02							
1798	-0.0294	0.08	-45.3	176	38				102.1	93.4	106.7	116.6
A	0.00591		-2.2	1.27	7.0				100.8	85.8	102.4	114.0
RUN 33	PT 3											
0.52	-5	0.11	-54.2	0.16	1.02							
1507	-0.0107	0.76	-33.6	-131	38				93.8	87.5	97.0	103.0
A	0.00313		-3.0	1.27	6.4				94.1	79.5	98.2	100.5
RUN 33	PT 5											
0.56	-5	0.12	-61.0	0.01	1.02							
1621	-0.0109	0.70	-36.4	63	38				95.7	91.5	102.9	106.5
A	0.00315		-2.8	1.27	6.3				96.1	81.4	100.7	102.0
RUN 33	PT 7											
0.60	-5	0.12	-66.7	0.01	1.02							
1739	-0.0109	0.76	-38.7	98	38				96.9	90.2	105.7	106.3
A	0.00311		-2.7	1.27	6.3				96.4	82.8	99.0	102.1
RUN 33	PT 9											
0.63	-5	0.12	-71.3	0.01	1.02							
1825	-0.0110	0.76	-40.3	112	38				98.1	92.1	104.9	108.1
A	0.00312		-2.3	1.27	6.3				98.3	84.5	101.4	103.9
RUN 36	PT 5											
0.56	-3	0.03	-58.4	0.43	1.02							
1621	-0.0038	0.46	-34.2	-119	38				93.4	89.6	102.0	105.0
A	0.00234		-2.4	1.27	6.4				93.6	84.3	99.1	87.7

Mtip RPM Config	Coll Ct/s Cq/s	FM Flap Vrot	F 30 F 40 F 70	Vatm Datm Rho	Patm Hum Temp	U n U' n EL n	U f U' f EL f	Sky Cov Opaque PDT	M2 dBA M8 dBA	M6 dBA M9 dBA M11 dBA	M2 SPL M8 SPL	M6 SPL M9 SPL M11 SPL
RUN 39	PT 3											
0.52	15	0.53	-21.1	0.42	1.02					91.5		106.9
1505	0.0772	1.51	-12.5	-26	55				99.8	96.2	102.2	99.2
A	0.01314		-4.0	1.27	6.7				99.0	91.1	103.5	94.3
RUN 39	PT 5											
0.56	15	0.52	-23.3	0.82	1.02					94.2		107.5
1623	0.0772	1.56	-13.4	-36	55				101.9	98.0	105.6	101.4
A	0.01326		-4.3	1.27	6.7				100.2	93.2	106.9	96.6
RUN 39	PT 7											
0.60	15	0.52	-24.3	0.92	1.02					98.5		109.3
1739	0.0787	1.53	-13.5	-34	55				105.7	102.5	110.9	105.1
A	0.01359		-4.4	1.27	6.7				109.0	98.1	111.7	100.6
RUN 39	PT 9											
0.63	15	0.52	-26.5	0.98	1.02					102.9		114.0
1825	0.0789	1.18	-14.1	-46	55				107.3	104.4	113.6	107.3
A	0.01370		-4.4	1.27	6.8				110.3	99.4	112.3	102.0
RUN 44	PT 3											
0.52	11	0.47	-33.7	0.24	1.02					89.7		105.8
1508	0.0500	1.00	-20.0	-90	55				100.5	95.0	102.5	97.2
A	0.00763		-2.9	1.27	6.8				100.8	89.3	103.1	91.7
RUN 44	PT 5											
0.56	11	0.45	-37.9	0.00	1.02					91.8		105.6
1624	0.0483	1.00	-21.7	-89	55				102.7	98.7	105.4	101.2
A	0.00752		-2.9	1.27	6.8				104.5	92.8	107.7	95.9

Mtip RPM Config	Coll Ct/s Cq/s	FM Flap Vrot	F 30 F 40 F 70	Vatm Datm Rho	Patm Hum Temp	U n U' n EL n	U f U' f EL f	Sky Cov Opaque PDT	M2 dBA			M6 dBA			M2 SPL			M6 SPL		
									M8 dBA	M8 dBA	M8 dBA	M9 dBA	M9 dBA	M11 dBA	M8 SPL	M8 SPL	M11 SPL	M9 SPL	M9 SPL	M11 SPL
RUN 44																				
PT 7																				
0.60	11	0.46	-41.5	0.06	1.02									96.6				107.4		
1741	0.0495	0.99	-23.0	27	55									99.8				103.0		
A	0.00767		-2.9	1.27	6.8									93.4				95.9		
RUN 44																				
PT 9																				
0.63	11	0.46	-44.8	0.21	1.02									100.4				111.7		
1826	0.0493	0.70	-24.0	121	55									100.5				103.2		
A	0.00764		-2.8	1.27	6.7									95.0				98.5		
RUN 45																				
PT 3																				
0.52	5	0.20	-46.8	0.91	1.02									86.8				104.1		
1505	0.0134	0.67	-28.2	166	55									95.4				99.7		
A	0.00254		-1.8	1.27	6.4									95.8				87.9		
RUN 46																				
PT 9																				
0.63	13	0.48	-36.9	0.86	1.02									91.0				102.3		
1831	0.0616	0.75	-19.6	178	55									104.9				111.7		
A	0.01018		-3.3	1.27	8.2									96.0				99.3		
RUN 47																				
PT 3																				
0.52	4	0.14	-47.7	0.88	1.02									86.4				104.4		
1508	0.0105	0.78	-28.9	-117	55									88.5				91.9		
A	0.00246		-2.0	1.27	7.3									83.7				86.7		
RUN 47																				
PT 5																				
0.56	4	0.14	-53.3	0.82	1.02									88.7				104.5		
1624	0.0105	0.74	-31.1	-114	55									94.7				101.0		
A	0.00250		-1.8	1.27	7.4									83.7				98.4		
														92.3				88.0		

Mtlp RPM Config	Coll Ct/s Cq/s	FM Flap Vrot	F 30 F 40 F 70	Vatm Datm Rho	Patm Hum Temp	U n U' n EL n	U f U' f EL f	Sky Cov Opaque PDT	M2 dBA M8 dBA	M6 dBA M9 dBA M11 dBA	M2 SPL M8 SPL	M6 SPL M9 SPL M11 SPL
RUN 47	PT 7											
0.60	4	0.14	-58.4	0.91	1.02					94.2		106.1
1741	0.0103	0.76	-33.1	-123	55				95.1	91.8	104.5	96.7
A	0.00247		-1.6	1.27	7.6					86.0		89.1
RUN 47	PT 9											
0.63	4	0.13	-63.3	0.86	1.02					89.4		101.3
1832	0.0102	0.68	-34.8	-119	55				95.3	93.2	104.4	99.9
A	0.00247		-1.3	1.27	8.0				95.6	87.8	100.1	92.2
RUN 48	PT 3											
0.52	3	0.07	-47.7	0.40	1.02					86.3		104.2
1513	0.0062	0.79	-29.3	-138	55				92.1	87.8	95.1	91.0
A	0.00217		-2.5	1.27	8.8				91.8	82.2	95.8	85.4
RUN 48	PT 5											
0.56	3	0.07	-54.5	0.59	1.02					89.3		104.1
1629	0.0061	0.65	-32.0	-133	55				98.2	93.1	102.1	95.7
A	0.00219		-1.8	1.26	9.2				96.2	87.9	100.2	90.0
RUN 48	PT 7											
0.60	3	0.06	-61.1	0.73	1.02					93.9		105.7
1748	0.0055	0.67	-34.5	-155	55				95.9	91.7	104.7	97.0
A	0.00217		-1.5	1.26	9.4				97.3	86.0	100.7	89.5
RUN 136	PT 1											
0.62	11	0.44	-45.2	1.06	1.02	6.68	1.38	0		103.0		112.7
1847	0.0485	-0.85	-24.7	47	50	0.046	0.140	0	104.8	104.7	111.9	107.5
B	0.00786	7.23	-3.7	1.20	22.8	3.6	1.6	08:06	106.9	98.4	108.7	101.0

Mtlp RPM Config	Coll C/s Cq/s	FM Flap Vrot	F 30 F 40 F 70	Vatm Datm Rho	Patm Hum Temp	U n U' n EL n	U f U' f EL f	Sky Cov Opaque PDT	M2 dBA			M6 dBA			M2 SPL			M6 SPL				
									M8 dBA	M8 dBA	M8 SPL	M9 dBA	M9 dBA	M11 dBA	M9 SPL	M9 SPL	M11 SPL	M2 SPL	M8 SPL	M2 SPL	M9 SPL	M11 SPL
RUN 136																		PT 2				
0.62	11	0.43	-46.1	1.13	1.02	6.78	1.29	0						102.9				112.7				
1848	0.0483	-1.01	-25.0	56	50	0.048	0.178	0						104.6				107.3				
B	0.00786	7.17	-3.6	1.20	23.1	9.0	5.9	08:10	104.6	107.2	108.6	98.5					101.1					
RUN 136																		PT 3				
0.62	11	0.43	-46.0	1.20	1.02	6.95		0						102.6				113.0				
1856	0.0481	-1.00	-24.9	55	50	0.076		0						103.3				106.3				
B	0.00784	7.41	-3.7	1.20	23.1	17.7		08:10	103.5	106.4	108.6	97.4					99.8					
RUN 136																		PT 7				
0.62	11	0.42	-47.3	1.19	1.02	6.74	1.70	0						102.6				112.5				
1850	0.0473	-1.26	-25.3	54	50	0.074	0.189	0						105.3				107.6				
B	0.00782	7.79	-3.3	1.19	23.8	8.9	2.1	08:50	105.3	107.9	109.6	99.2					101.3					
RUN 141																		PT 1				
0.52	5	0.16	-48.2	1.04	1.02	3.44	1.19	0						90.4				106.7				
1551	0.0133	1.01	-28.7	-6	46	0.065	0.130	0						91.2				94.6				
B	0.00308	3.21	-2.6	1.20	23.6	5.6	1.8	08:05	95.4	95.0	99.5	86.0					89.2					
RUN 141																		PT 2				
0.52	5	0.15	-48.0	1.49	1.02	3.27	1.50	0														
1551	0.0126	1.01	-28.8	359	46	0.077	0.154	0						96.1				98.4				
B	0.00309	3.43	-3.0	1.19	24.1	1.6	5.3	08:15	95.3					99.9								
RUN 141																		PT 3				
0.52	5	0.14	-47.7	1.61	1.02	3.27	1.33	0						90.1				106.4				
1551	0.0125	1.00	-28.7	27	46	0.106	0.199	0						91.6				94.2				
B	0.00310	3.34	-3.1	1.19	24.1	2.0	6.0	08:15	96.8	95.7	99.9	86.0					88.9					

Mtip RPM Config	Coll Ct/s Cq/s	FM Flap Vrot	F 30 F 40 F 70	Vatm Datm Rho	Patm Hum Temp	U n U' n EL n	U f U' f EL f	Sky Cov Opaque PDT	M2 dBA			M6 dBA			M2 SPL			M6 SPL					
									M8 dBA	M8 dBA	M8 dBA	M9 dBA	M9 dBA	M11 dBA	M8 SPL	M8 SPL	M8 SPL	M9 SPL	M9 SPL	M11 SPL			
RUN 141																							
0.52 1552 B	PT 4 5 0.0119 0.00307	0.14	-48.3	1.61	1.02	3.64	1.73	0			90.8					106.6							
		0.93	-29.0	35	46	0.098	0.215	0	98.1		92.3		99.7		95.6								
		4.07	-3.2	1.19	24.1	2.5	5.8	08:20	95.5		87.1		99.3		90.2								
RUN 141																							
0.52 1552 B	PT 5 5 0.0119 0.00308	0.13	-47.4	1.53	1.02	3.35	1.28	0			90.6					106.5							
		0.97	-28.7	30	46	0.081	0.180	0	97.7		92.3		100.1		95.3								
		4.15	-3.3	1.19	24.1	10.1	4.0	08:25	95.9		86.8		100.7		89.6								
RUN 141																							
0.52 1552 B	PT 7 5 0.0120 0.00308	0.14	-46.8	1.40	1.02	3.28	1.53	0			90.2					106.2							
		0.97	-28.5	13	46	0.072	0.251	0	96.8		92.3		98.3		94.9								
		4.41	-3.4	1.19	24.1	4.3	2.9	08:45	94.5		86.8		98.8		89.6								
RUN 145																							
0.52 1534 B	PT 1 5 0.0139 0.00288	0.18	-46.8	1.52	1.01	3.61	2.01	4			86.2					102.3							
		0.51	-27.7	-13	45	0.064	0.069	4	94.8		91.1		97.0		94.2								
		1.00	-2.8	1.22	16.2	1.9	1.7	05:00	93.9		85.3		97.7		88.1								
RUN 145																							
0.52 1536 B	PT 5 5 0.0135 0.00281	0.18	-47.0	1.54	1.01	3.64	1.54	4			85.9					102.2							
		0.42	-27.8	-28	45	0.080	0.113	4	93.4		90.3		95.4		94.0								
		2.18	-3.1	1.22	16.9	8.7	1.9	05:25	93.1		84.5		96.6		87.7								
RUN 145																							
0.52 1537 B	PT 6 5 0.0134 0.00282	0.18	-47.2	1.20	1.01	3.50	1.38	4			86.1					102.2							
		0.39	-27.8	-22	45	0.058	0.023	4	94.5		89.8		96.8		93.7								
		1.60	-3.1	1.22	16.9	2.0	0.8	05:35	93.8		84.0		97.9		87.2								

Mtip RPM Config	Coll Ct/s Cq/s	FM Flap Vrot	F 30 F 40 F 70	Vatm Datm Rho	Patm Hum Temp	U n U' n EL n	U f U' f EL f	Sky Cov Opaque PDT	M2 dBA M8 dBA	M6 dBA M9 dBA M11 dBA	M2 SPL M8 SPL	M6 SPL M9 SPL M11 SPL
RUN 147												
0.52	PT 2	0.29	-45.0	0.77	1.01	4.02		3		90.4		106.5
1552	0.0241	0.54	-26.7	3	45	0.033		3	96.9	92.2	99.2	94.5
B	0.00413	3.99	-3.1	1.19	24.8	7.6		08:00	96.1	86.8	99.4	89.2
RUN 147												
0.52	PT 3	0.29	-45.0	0.48	1.01	3.96	0.84	3		90.3		106.5
1554	0.0240	0.54	-26.6	3	45	0.083	0.073	3	97.2	92.9	99.9	95.8
B	0.00413	4.34	-3.1	1.19	24.8	7.2	0.8	08:00	96.7	87.3	100.1	90.4
RUN 147												
0.52	PT 4	0.29	-43.9	0.54	1.01	3.79	0.68	3		90.5		106.3
1556	0.0240	0.54	-26.5	32	45	0.039	0.160	3	96.1	92.2	98.0	95.1
B	0.00417	4.35	-3.3	1.19	24.8	8.6	2.3	08:00	95.6	86.8	99.4	89.7
RUN 147												
0.52	PT 5	0.28	-44.0	0.66	1.01	3.98	0.64	3		90.6		106.4
1556	0.0235	0.52	-26.6	29	45	0.074	0.129	3	97.4	92.8	100.0	95.2
B	0.00417	4.38	-3.3	1.19	24.8	9.8	1.5	08:05	97.2	87.6	100.5	90.1
RUN 147												
0.52	PT 6	0.27	-44.2	0.77	1.01	4.09	0.61	3		90.5		106.4
1557	0.0231	0.52	-26.7	20	45	0.039	0.114	3	95.8	91.9	97.6	94.4
B	0.00412	4.85	-3.3	1.18	25.7	2.8	1.3	08:10	95.7	86.2	99.0	88.9
RUN 147												
0.52	PT 7	0.28	-43.8	0.38	1.01	3.89	0.91	3		90.6		106.4
1557	0.0236	0.54	-26.5	-27	45	0.074	0.148	3	96.2	92.3	97.9	94.8
B	0.00418	4.79	-3.3	1.18	26.0	15.7	2.1	08:15	95.0	86.7	98.8	89.4

Mtip RPM Config	Coll Ct/s Cq/s	FM Flap Vrot	F 30 F 40 F 70	Vatm Datm Rho	Patm Hum Temp	U n U' n EL n	U f U' f EL f	Sky Cov Opaque PDT	M2 dBA M8 dBA	M6 dBA M9 dBA M11 dBA	M2 SPL M8 SPL	M6 SPL M9 SPL M11 SPL
RUN 152	PT 4											
0.61	3	0.03	-64.5	3.48	1.01	3.36	2.86	3		97.9		109.1
1850	0.0041	0.35	-35.7	52	45	0.191	0.329	3	98.0	93.7	105.3	98.3
B	0.00250	3.27	-3.6	1.15	34.0	9.6	4.2	13:40	95.7	88.6	98.8	93.9
RUN 152	PT 5											
0.61	3	0.03	-65.0	3.27	1.01	3.27		3		97.7		108.9
1850	0.0041	0.34	-35.8	54	45	0.164		3	98.9	94.9	105.7	98.8
B	0.00251	3.37	-3.6	1.15	34.0	7.7		13:40	96.7	89.3	99.7	93.9
RUN 152	PT 7											
0.61	3	0.03	-64.7	3.46	1.01	3.37	2.92	3		97.5		108.8
1849	0.0038	0.37	-35.8	48	45	0.226	0.193	3	97.7	94.3	105.1	98.7
B	0.00251	4.08	-3.7	1.15	33.9	5.4	6.6	14:00	95.6	88.8	99.4	93.7
RUN 154	PT 1											
0.62	3	0.04	-107.7	2.58	1.02		2.98	1		95.6		107.0
1842	0.0044	0.95	-60.3	48	68		0.569	1	98.5	95.2	106.1	100.5
C	0.00235	3.31	-2.8	1.20	21.2		6.5	11:05	97.5	89.3	101.1	93.3
RUN 154	PT 3											
0.62	3	0.04	-108.6	2.62	1.02		2.30	1		95.8		107.0
1842	0.0041	0.88	-59.1	58	68		0.362	1	98.4	96.2	105.7	100.5
C	0.00237	3.43	-3.1	1.20	20.8		7.6	11:15	98.9	89.4	101.8	93.2
RUN 157	PT 2											
0.62	7	0.28	-95.9	2.37	1.02		2.41	4		93.7		103.7
1849	0.0230	1.23	-52.3	50	46		0.342	3	106.1	101.2	109.3	103.8
C	0.00409	5.35	-2.8	1.19	24.6		4.2	09:25	104.2	95.1	105.8	96.9

Mtip RPM Config	Coll Ct/s Cq/s	FM Flap Vrot	F 30 F 40 F 70	Vatm Datm Rho	Patm Hum Temp	U n U' n EL n	U f U' f EL f	Sky Cov Opaque PDT	M6 dBA M9 dBA M11 dBA	M2 SPL M8 SPL	M6 SPL M9 SPL M11 SPL
RUN 157 PT 3											
0.62	7	0.27	-97.4	2.45	1.02		2.77	4	94.0		103.8
1849	0.0226	1.19	-52.8	44	46		0.347	3	101.6	110.1	104.4
C	0.00411	5.52	-2.9	1.19	24.6		7.4	09:30	95.7	106.0	97.6
RUN 157 PT 4											
0.62	7	0.27	-97.1	2.15	1.02		2.26	4	94.0		103.6
1849	0.0232	1.19	-51.7	46	46		0.290	3	101.5	109.6	103.9
C	0.00413	5.13	-3.0	1.19	24.6		2.6	09:35	95.6	106.4	97.9
RUN 157 PT 5											
0.62	7	0.27	-99.1	2.47	1.02		2.37	4	93.8		103.5
1849	0.0227	1.24	-52.3	57	46		0.252	3	101.3	109.5	104.1
C	0.00412	5.21	-3.0	1.19	24.6		4.8	09:40	95.2	105.2	97.3
RUN 162 PT 2											
0.62	3	0.06	-41.2	1.27	1.02		1.19	8	94.8		105.9
1830	0.0057	0.20	-72.1	-17	73		0.115	6	93.5	106.5	98.4
C	0.00222	2.95	-2.2	1.22	17.4		2.8	07:20	86.6	98.8	90.2
RUN 162 PT 3											
0.62	3	0.06	-50.2	1.35	1.02		1.55	8	94.9		105.8
1829	0.0055	0.25	-56.4	-7	73		0.211	6	94.9	106.5	99.1
C	0.00220	3.16	-2.5	1.22	17.4		4.7	07:25	88.3	100.5	91.6
RUN 162 PT 4											
0.62	3	0.05	-47.2	1.38	1.02		1.16	9	94.9		105.8
1830	0.0051	0.10	-78.4	16	73		0.198	6	94.1	106.4	99.0
C	0.00219	3.22	-2.3	1.22	17.4		3.2	07:35	87.6	99.8	91.6

Mtlp RPM Config	Coll Ct/s Cq/s	FM Flap Vrot	F 30 F 40 F 70	Vatm Datm Rho	Patm Hum Temp	U n U' n EL n	U f U' f EL f	Sky Cov Opaque PDT	M2 dBA M8 dBA	M6 dBA M9 dBA M11 dBA	M2 SPL M8 SPL	M6 SPL M9 SPL M11 SPL
RUN 162	PT 5											
0.62	3	0.05	-45.5	1.80	1.02		1.51	9		94.9		105.8
1829	0.0049	0.17	-78.4	35	73		0.241	6	98.9	94.1	106.3	98.9
C	0.00219	3.17	-2.5	1.22	17.4		5.6	07:40	96.8	87.4	99.5	91.4
RUN 162	PT 6											
0.62	3	0.05	-38.8	1.63	1.02		1.62	9		95.2		105.9
1830	0.0048	0.61	-78.4	37	73		0.151	6	99.4	94.7	106.6	99.3
C	0.00221	3.24	-3.2	1.22	18.1		1.4	07:45	97.7	88.0	116.1	91.8
RUN 162	PT 7											
0.62	3	0.04	-41.3	1.61	1.02		1.71	9		94.7		105.8
1830	0.0046	0.33	-81.5	30	73		0.217	6	97.0	93.9	106.3	99.1
C	0.00221	3.13	-2.8	1.22	18.1		6.4	07:50	96.7	87.1	116.3	91.2
RUN 163	PT 2											
0.62	7	0.27	-65.6	2.49	1.02		1.99	9		97.6		107.3
1847	0.0228	0.67	-58.0	16	73		0.316	6	107.1	102.8	110.6	105.3
C	0.00410	5.12	-3.0	1.20	21.3		4.1	08:25	105.4	96.2	106.8	98.0
RUN 163	PT 3											
0.62	7	0.28	-76.6	1.78	1.02		1.67	9		97.8		107.4
1846	0.0235	0.64	-53.3	18	73		0.323	6	106.9	102.4	110.3	105.6
C	0.00414	4.91	-3.0	1.20	22.1		3.8	08:30	106.9	95.8	108.3	98.1
RUN 163	PT 4											
0.62	7	0.27	-73.9	2.38	1.02		1.60	9		97.6		107.1
1844	0.0232	0.59	-53.3	29	73		0.385	6	107.4	102.3	110.5	105.1
C	0.00414	5.08	-3.0	1.20	22.6		2.8	08:35	104.8	95.6	106.3	97.6

Mtip RPM Config	Coll Ct/s Cq/s	FM Flap Vrot	F 30 F 40 F 70	Vatm Datm Rho	Patm Hum Temp	U n U' n EL n	U f U' f EL f	Sky Cov Opaque PDT	M2 dBA			M6 dBA			M2 SPL			M6 SPL		
									M8 dBA	M8 dBA	M8 dBA	M9 dBA	M9 dBA	M9 dBA	M8 SPL	M8 SPL	M8 SPL	M9 SPL	M9 SPL	M11 SPL
RUN 163																				
0.62	PT 5	7	0.27	-74.7	2.36	1.02	2.36	9				97.5						107.0		
1848	0.0228	0.63	-53.3	41	73		0.151	6	106.5			103.1			110.1			105.7		
C	0.00412	5.44	-3.1	1.20	22.8		1.9	08:40	104.1			96.3			106.7			98.5		
RUN 163																				
0.62	PT 6	7	0.27	-67.2	2.65	1.02	1.74	9				100.8						110.4		
1849	0.0226	0.66	-53.3	35	73		0.273	6	107.4			102.2			110.8			105.5		
C	0.00412	5.39	-3.6	1.20	22.8		3.0	08:45	106.4			95.9			108.1			98.3		
RUN 163																				
0.62	PT 7	7	0.28	-68.8	2.15	1.02	1.04	9				100.5						110.3		
1850	0.0236	0.50	-58.0	28	73		0.241	6	104.8			101.2			108.9			104.4		
C	0.00418	4.47	-3.0	1.20	22.9		2.6	08:50	103.8			94.5			105.7			97.0		
RUN 164																				
0.62	PT 1	7	0.30	-92.9	1.77	1.02	0.81	8				98.7						108.2		
1848	0.0239	0.16	-44.6	42	73		0.203	6	105.1			100.7			109.5			103.5		
C	0.00395	4.68	-2.5	1.21	21.8		1.3	09:50	103.2			94.3			105.3			96.4		
RUN 164																				
0.62	PT 3	7	0.30	-94.1	1.77	1.02	0.79	8				100.4						110.4		
1847	0.0240	0.31	-50.6	2	73		0.150	6	106.1			101.9			110.2			104.9		
C	0.00400	3.95	-3.3	1.21	21.8		0.9	10:00	104.9			95.4			106.6			97.6		
RUN 164																				
0.62	PT 5	7	0.28	-120.8	2.33	1.02	1.84	7				99.5						107.8		
1847	0.0229	-0.12	-50.7	51	73		0.281	6	107.4			102.3			110.5			104.7		
C	0.00394	4.79	-2.6	1.21	21.8		10.4	10:10	104.7			96.0			106.1			98.1		

Mtlp RPM Config	Coll Ct/s Cq/s	FM Flap Vrot	F 30 F 40 F 70	Vatm Datm Rho	Patm Hum Temp	U n U' n EL n	U f U' f EL f	Sky Cov Opaque PDT	M2 dBA			M6 dBA			M2 SPL			M6 SPL		
									M8 dBA	M9 dBA	M11 dBA	M8 dBA	M9 dBA	M11 dBA	M8 SPL	M9 SPL	M11 SPL			
RUN 164																				
0.62	PT 6	7	-105.2	2.60	1.02		1.73	7				100.8						110.3		
1847	0.0225	-0.18	-49.4	35	73		0.359	6	106.2			101.7			110.2			104.9		
C	0.00394	5.17	-3.0	1.20	23.8		7.7	10:15	105.6			95.3			107.0			97.4		
RUN 165																				
0.62	PT 1	15	-44.0	2.98	1.02		2.30	7				102.8						109.2		
1849	0.0760	-0.03	-19.4	52	73		0.314	6	114.0			110.4			116.8			112.5		
C	0.01374	8.44	-5.2	1.20	23.9		4.3	10:50	111.8			103.9			113.5			106.0		
RUN 165																				
0.62	PT 2	15	-44.6	3.44	1.02		2.70	7				102.1						109.0		
1844	0.0754	0.03	-19.4	53	73		0.215	6	115.0			110.0			117.4			112.1		
C	0.01375	8.65	-5.4	1.20	23.9		5.6	10:55	111.5			103.3			113.2			105.3		
RUN 165																				
0.62	PT 3	15	-42.9	3.57	1.02		2.64	7				102.4						108.7		
1848	0.0751	-0.04	-18.5	51	73		0.476	6	115.5			110.0			118.1			112.3		
C	0.01369	8.41	-5.8	1.20	23.9		10.5	11:00	111.2			103.1			113.2			105.2		
RUN 165																				
0.62	PT 4	15	-12.6	3.31	1.02		2.51	7				102.0						108.7		
1848	0.0748	-0.12	-48.0	55	73		0.269	6	114.1			109.8			117.0			111.9		
C	0.01366	8.53	-5.6	1.20	23.9		7.3	11:05	111.0			103.3			112.8			105.2		
RUN 165																				
0.62	PT 5	15	-21.0	3.34	1.02		2.88	7				105.5						111.9		
1848	0.0752	0.00	-39.7	59	73		0.204	6	112.8			109.6			116.2			111.7		
C	0.01368	8.27	-5.3	1.20	23.9		2.7	11:10	111.1			103.5			113.0			105.4		

Mtip RPM Config	Coll Ct/s Cq/s	FM Flap Vrot	F 30 F 40 F 70	Vatm Datm Rho	Patm Hum Temp	U n U' n EL n	U f U' f EL f	Sky Cov Opaque PDT	M2 dBA M8 dBA	M6 dBA M9 dBA M11 dBA	M2 SPL M8 SPL	M6 SPL M9 SPL M11 SPL
RUN 168 PT 1												
0.62	5	0.15	-95.9	2.76	1.02	4.18	1.73	5		98.8		109.5
1850	0.0121	0.51		58	68	0.238	0.270	4	102.8	99.0	106.8	102.4
B	0.00285	4.65	-2.8	1.18	27.9	12.9	8.0	12:20	99.7	93.2	102.2	97.0
RUN 168 PT 2												
0.62	5	0.14	-66.8	3.04	1.02	4.31	1.88	5		98.4		109.6
1849	0.0118	0.33		57	68	0.219	0.262	4	102.4	98.2	106.3	101.5
B	0.00285	4.24	-2.9	1.18	27.9	11.8	7.8	12:25	99.3	92.7	101.6	96.0
RUN 168 PT 3												
0.62	5	0.15	-88.9	2.96	1.02	4.22	1.96	5		99.2		109.6
1849	0.0118	0.29		56	68	0.116	0.309	4	104.2	99.6	107.3	102.8
B	0.00284	4.37	-2.8	1.18	27.9	13.2	5.5	12:30	101.2	94.0	103.3	97.6
RUN 168 PT 5												
0.61	5	0.14	-113.6	3.05	1.02	4.37	1.85	5		98.9		109.6
1849	0.0112	0.24		55	68	0.173	0.269	4	101.8	98.4	106.0	101.7
B	0.00282	4.74	-2.7	1.18	29.3	5.0	2.0	12:40	99.0	92.9	101.9	96.2
RUN 168 PT 6												
0.61	5	0.14	-22.8	3.12	1.02	3.97	1.68	5		98.9		109.6
1849	0.0115	0.23		59	68	0.199	0.303	4	102.4	98.1	106.3	102.0
B	0.00284	4.47	-2.7	1.18	29.3	5.5	6.7	12:45	98.8	92.3	100.9	95.9
RUN 168 PT 7												
0.61	5	0.14	-34.8	3.10	1.02	4.23	2.21	5		99.0		109.5
1849	0.0113	0.24		57	68	0.175	0.167	4	101.3	98.6	105.6	101.8
B	0.00284	4.37	-2.9	1.18	29.3	5.7	2.5	12:50	99.1	93.0	101.7	96.7

Mtip RPM Config	Coll Ct/s Cq/s	FM Flap Vrot	F 30 F 40 F 70	Vatm Datm Rho	Patm Hum Temp	U n U' n EL n	U f U' f EL f	Sky Cov Opaque PDT	M2 dBA M8 dBA	M6 dBA M9 dBA M11 dBA	M2 SPL M8 SPL	M6 SPL M9 SPL M11 SPL
RUN 169 PT 1												
0.52	7	0.25	-39.3	3.67	1.02	4.90	2.38	4		91.4		105.7
1566	0.0213	0.98		48	68	0.195	0.205	3	99.5	96.9	101.5	99.9
B	0.00399	5.34	-3.3	1.18	28.5	3.3	3.6	13:15	97.5	91.2	101.1	94.3
RUN 169 PT 2												
0.52	7	0.23	-61.1	3.85	1.02	4.69	2.59	4		91.0		105.6
1566	0.0200	1.01		46	68	0.186	0.334	3	99.2	96.7	101.0	99.4
B	0.00392	5.50	-3.6	1.18	28.5	10.0	12.2	13:20	97.2	91.1	101.2	93.7
RUN 169 PT 3												
0.52	7	0.22	-53.1	3.69	1.02	4.81	2.41	4		91.1		103.6
1566	0.0190	1.00		51	68	0.130	0.307	3	101.0	96.5	102.5	99.6
B	0.00389	5.72	-3.7	1.18	28.5	8.2	6.1	13:25	98.1	91.1	101.2	94.1
RUN 169 PT 4												
0.52	7	0.22	-79.7	3.40	1.02	4.81	2.61	4		91.9		106.4
1566	0.0196	0.96		43	68	0.171	0.186	3	102.4	96.2	103.3	98.9
B	0.00394	5.35	-3.6	1.18	28.5	7.6	2.2	13:30	97.7	91.1	100.5	93.8
RUN 169 PT 5												
0.52	7	0.19	-56.2	4.70	1.02	5.39	3.01	4		91.8		106.1
1565	0.0174	0.91		38	68	0.252	0.353	3	100.5	96.6	102.7	99.6
B	0.00383	6.62	-3.5	1.18	28.5	10.9	9.7	14:00	97.2	91.6	100.9	94.8
RUN 169 PT 6												
0.52	7	0.19	-81.2	5.01	1.02	5.40	3.65	4		91.1		106.1
1565	0.0172	0.91		34	68	0.282	0.289	3	101.3	96.7	103.9	99.9
B	0.00381	6.61	-3.6	1.18	28.5	16.0	2.4	14:05	97.5	91.9	100.8	95.5

Mtip RPM Config	Coll Ct/s Cq/s	FM Flap Vrot	F 30 F 40 F 70	Vatm Datm Rho	Patm Hum Temp	U n U' n EL n	U f U' f EL f	Sky Cov Opaque PDT	M2 dBA			M6 dBA			M2 SPL			M6 SPL					
									M8 dBA	M8 dBA	M8 dBA	M9 dBA	M9 dBA	M9 dBA	M8 SPL	M8 SPL	M8 SPL	M9 SPL	M9 SPL	M9 SPL			
RUN 169																							
0.52	PT 7	7	-87.0	5.74	1.02	5.08	3.53	4				91.3						106.1					
1565	0.0183	0.88		36	68	0.290	0.475	3	101.6			97.1			104.1			100.3					
B	0.00387	5.81	-3.7	1.18	28.5	3.3	7.1	14:10	98.0			92.1			101.6			95.7					
RUN 170																							
0.62	PT 6	7	38.3	1.89	1.02	5.75	1.23				100.1							109.5					
1842	0.0219	0.79		57	70	0.322	0.259		96.8			111.2			99.9			114.0					
B	0.00391	5.23	-2.9	1.20	22.7	28.0	5.9		92.5			95.3			94.7			97.2					

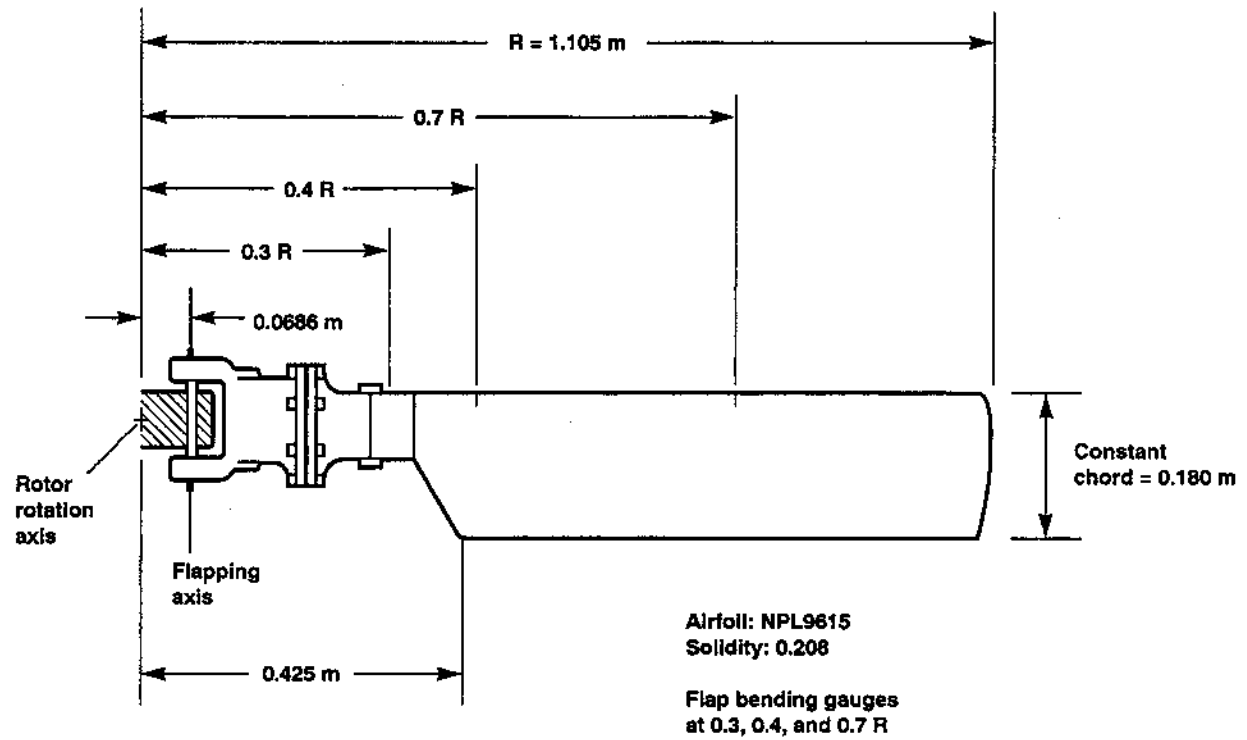


Figure 1. Tail rotor blade.

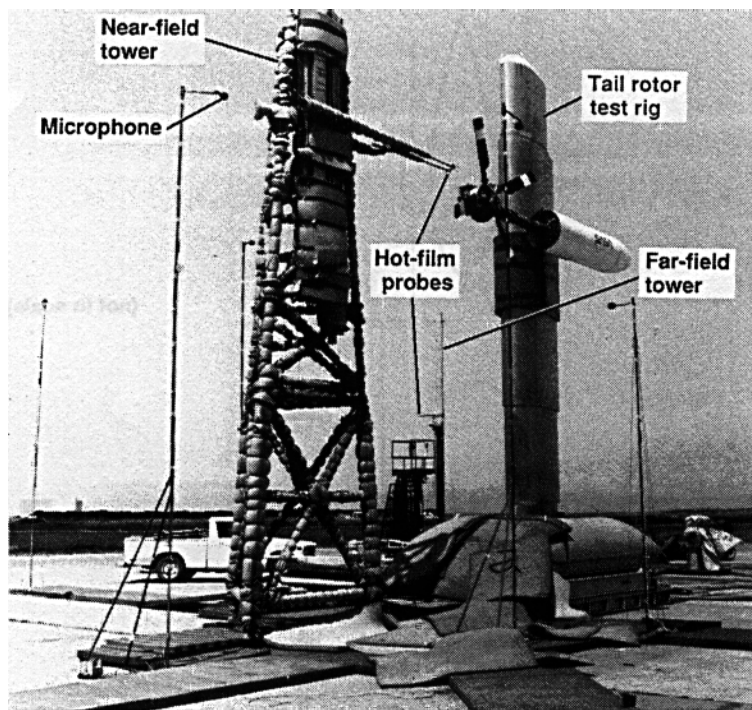


Figure 2. Experimental setup.

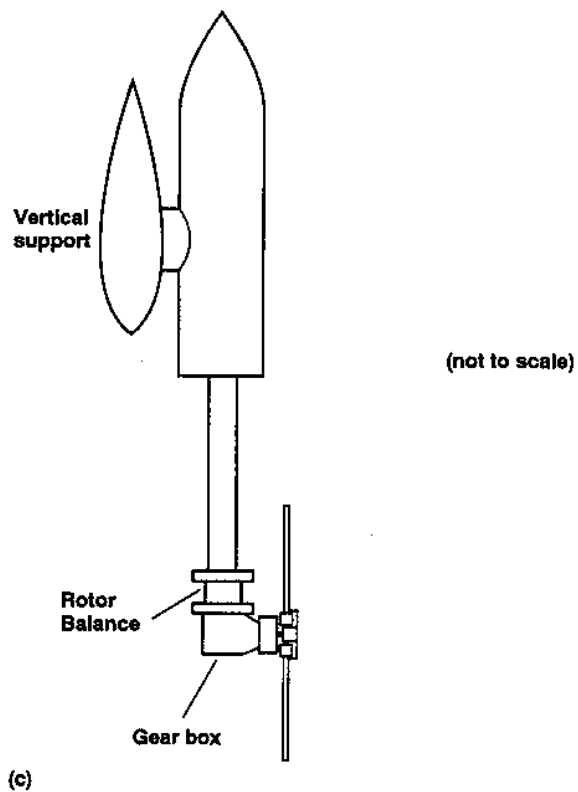
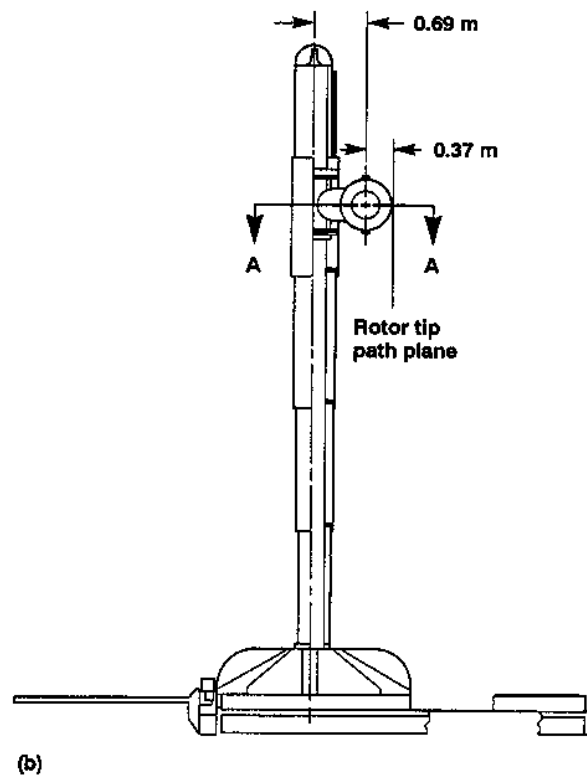
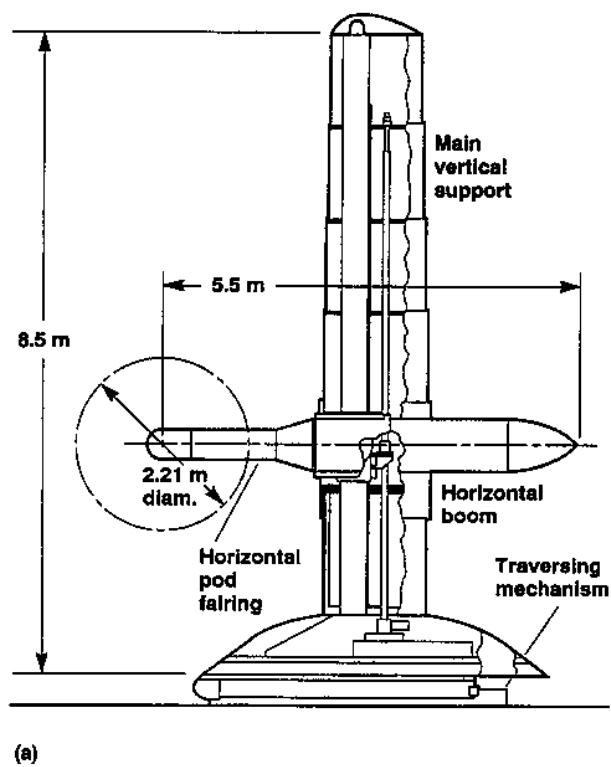


Figure 3. Tail rotor test rig. (a) Front view, (b) side view, (c) section A-A.

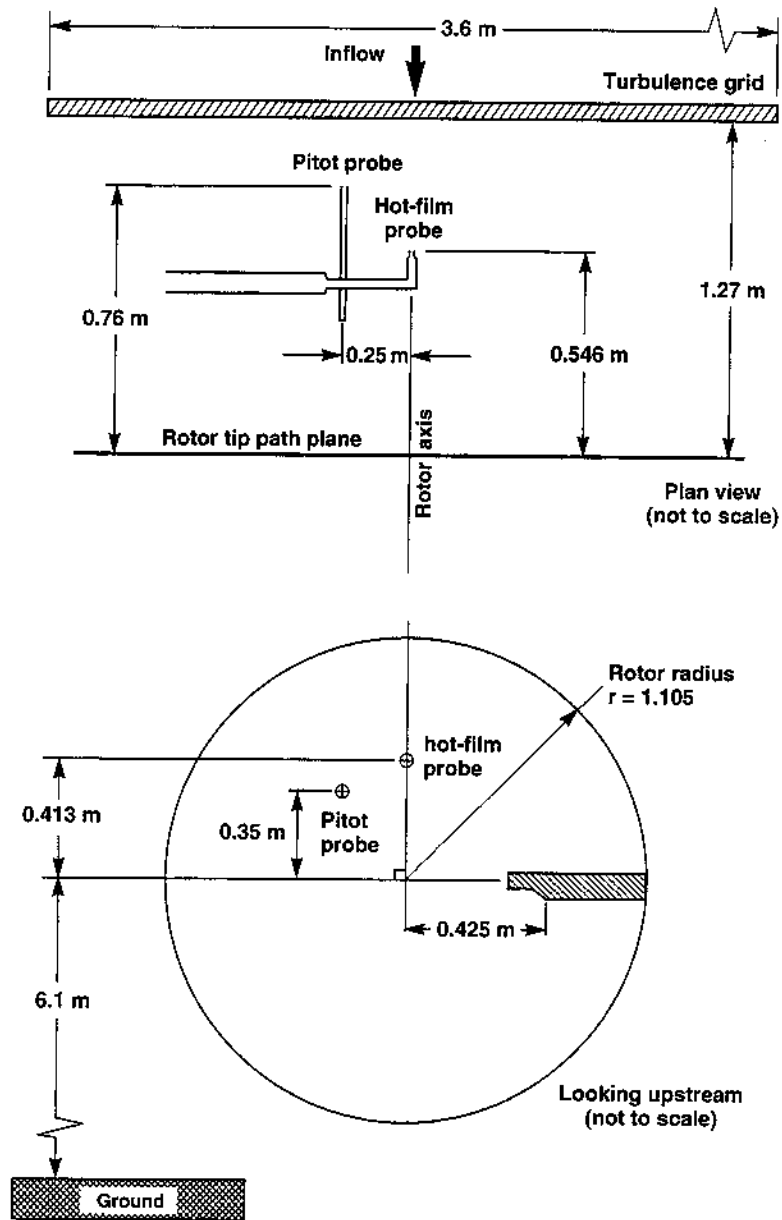


Figure 4. Near-field hot-film probe and grid location.

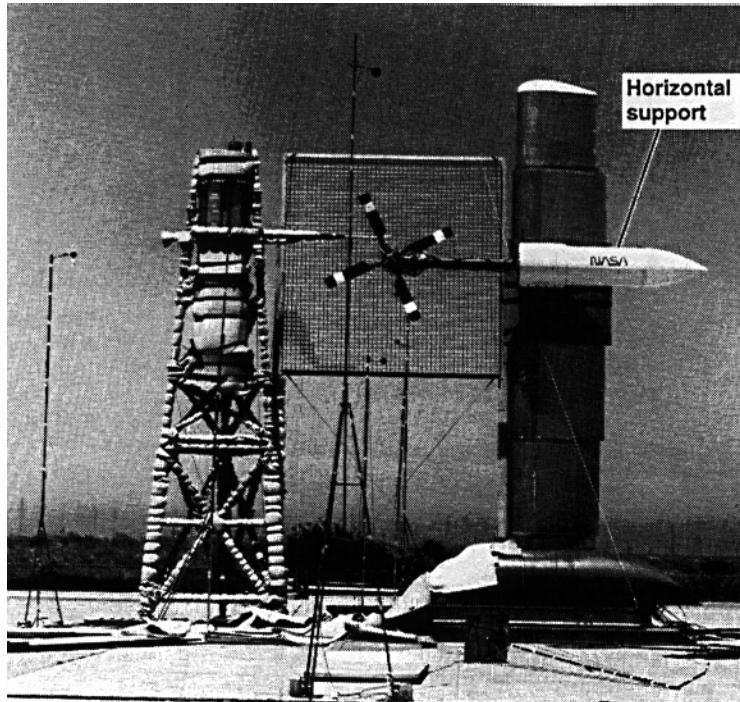


Figure 5. Turbulence-generating grid installation.

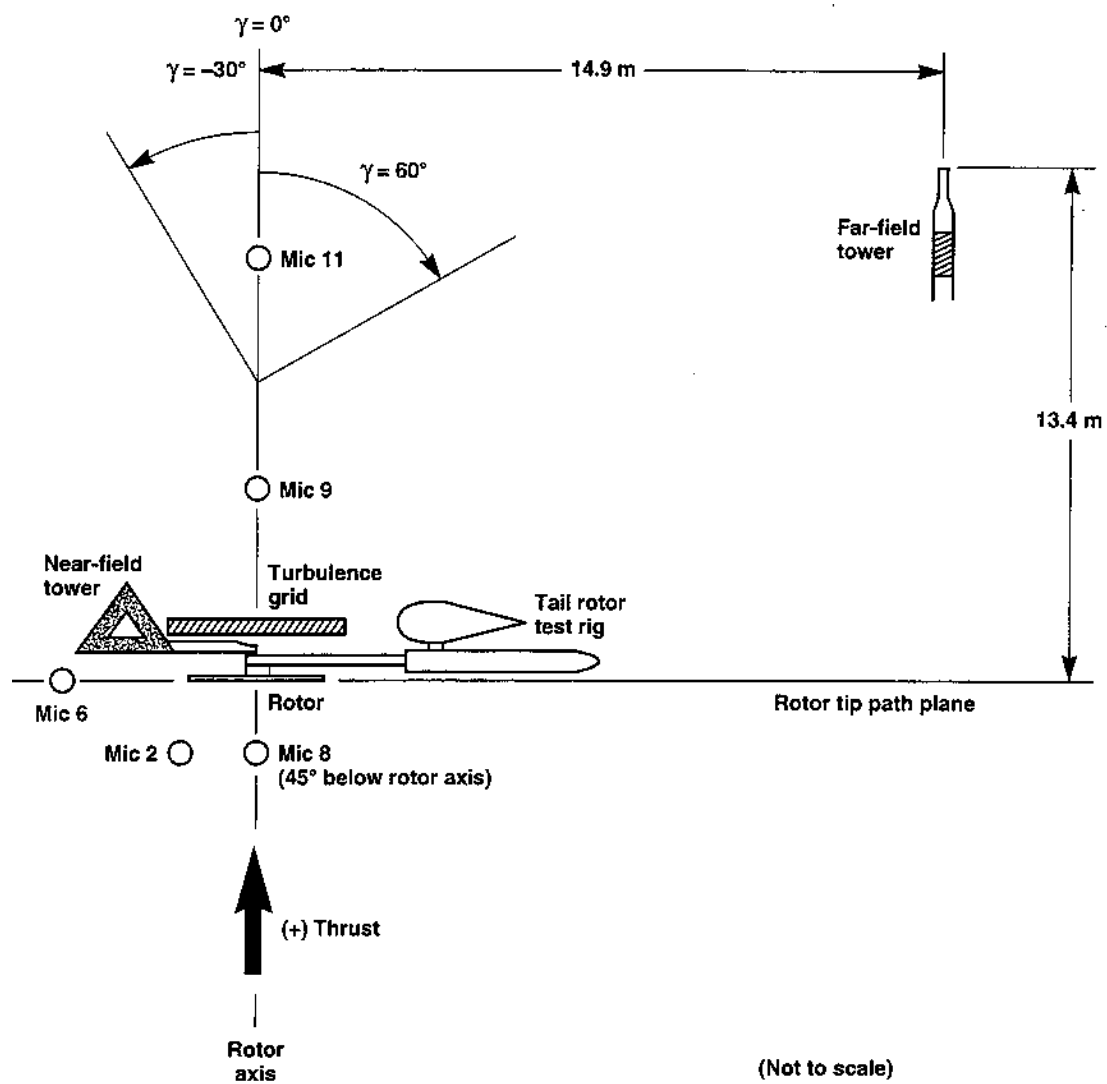


Figure 6. Plan view of experimental setup.

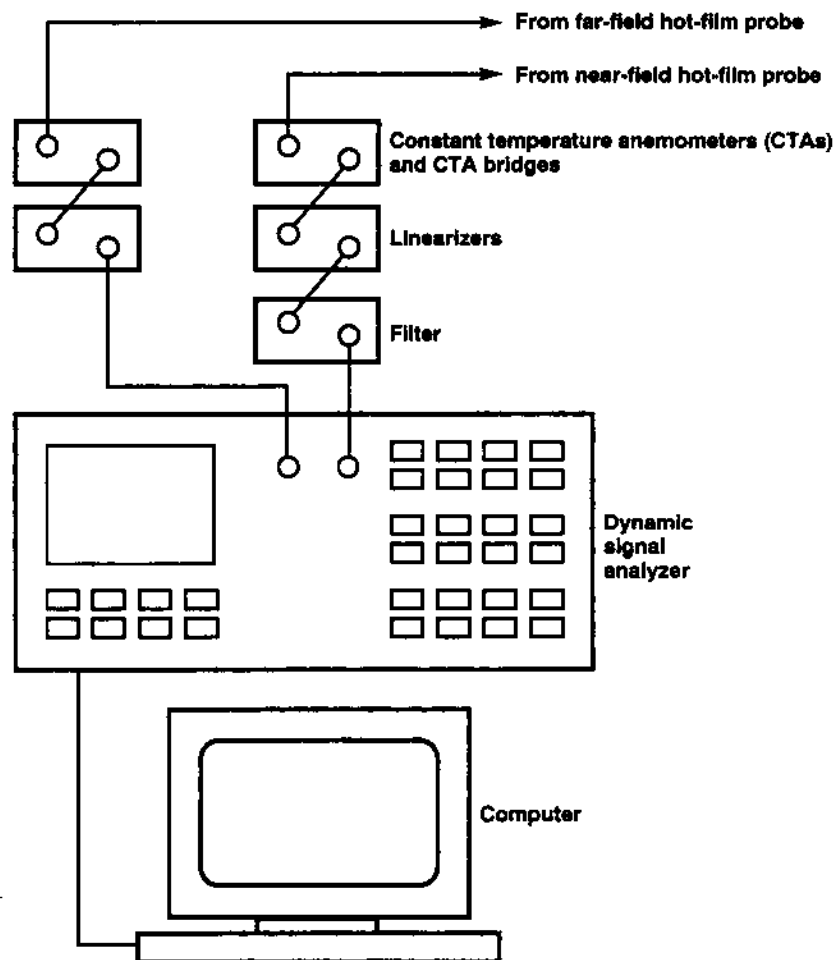


Figure 7. Hot-film data acquisition system.

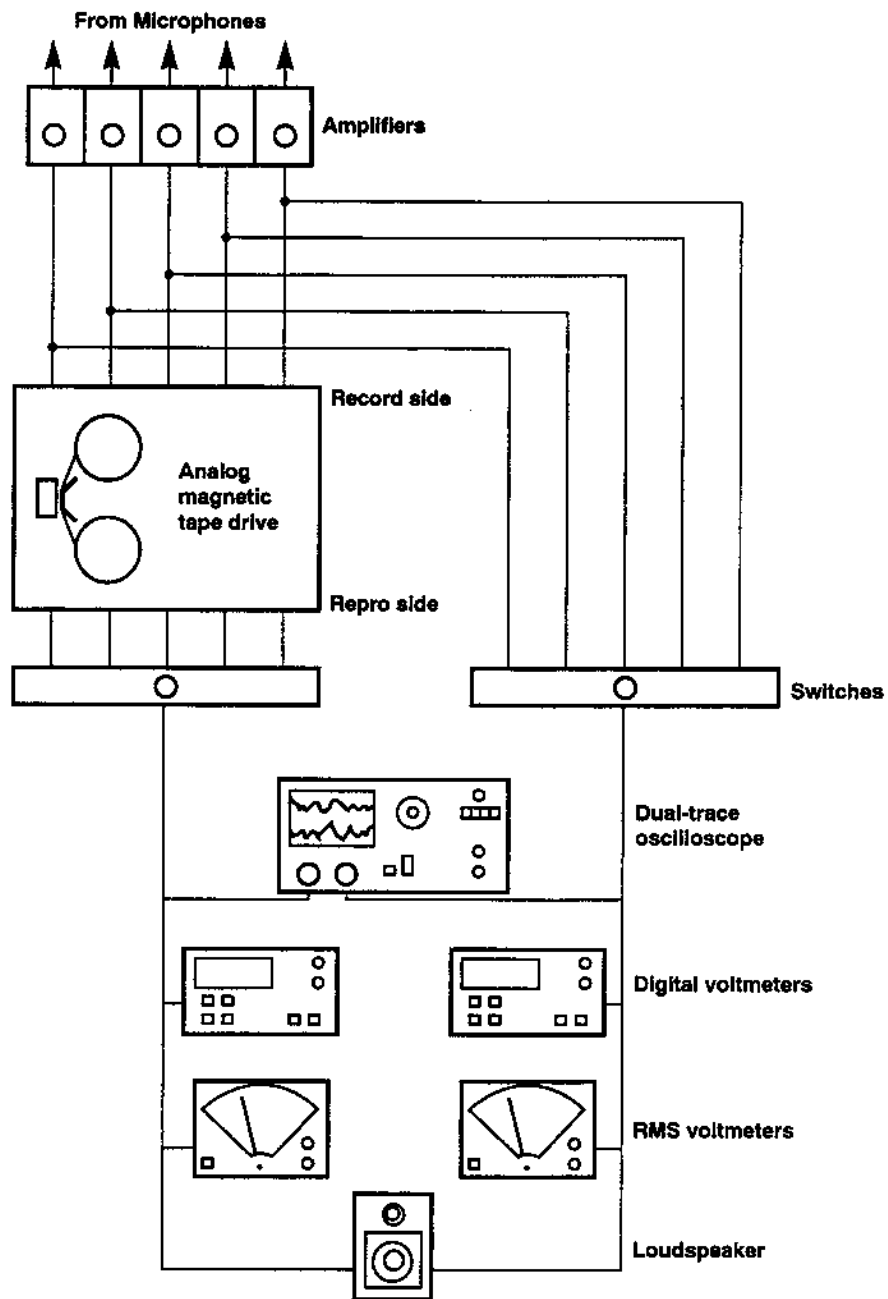


Figure 8. Acoustic data acquisition system.

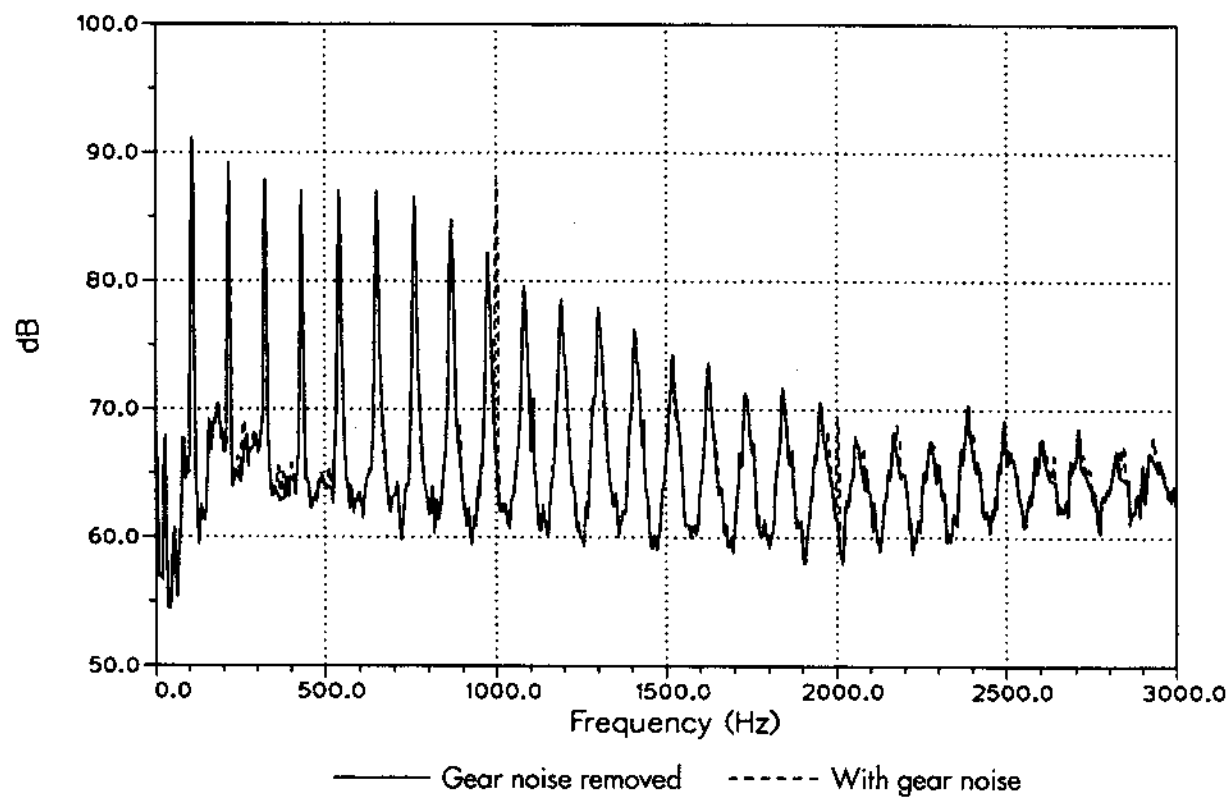


Figure 9. Power spectrum showing effect of gear noise removal at microphone 9, $O_r = 4.5$, Run 44 Point 5, $M_{tip} = 0.56$, $\theta = 11^\circ$, $U_\infty = 0.00$ m/s, near-field tower not installed, grid not installed.

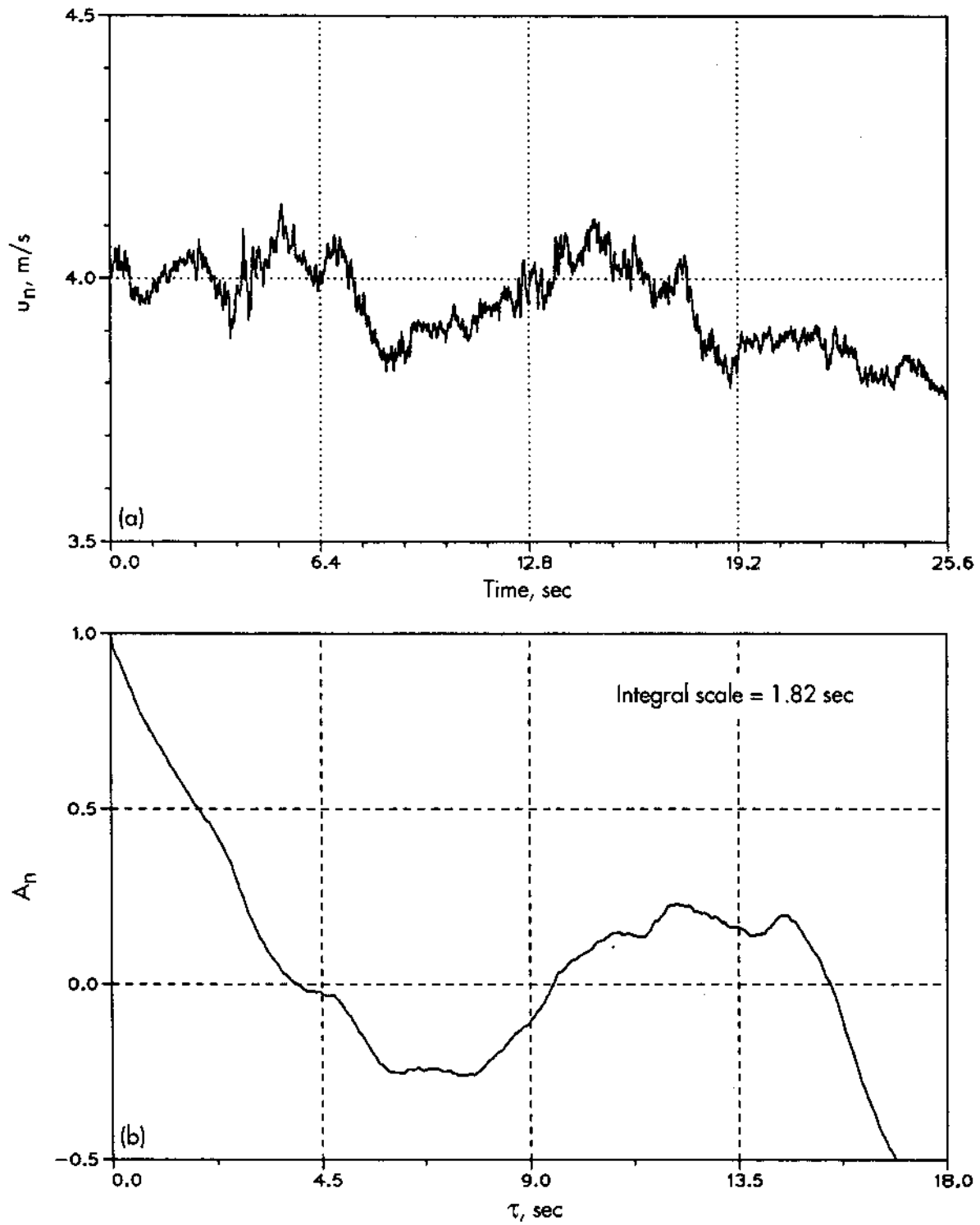


Figure 10. Example of near-field hot-film data for Run 147 Point 3, $\bar{u}_n = 3.96$ m/s, $u'_n = 0.083$ m/s, $\Lambda_n = 7.2$ m, near-field tower installed, grid not installed. (a) Time history, (b) autocorrelation.

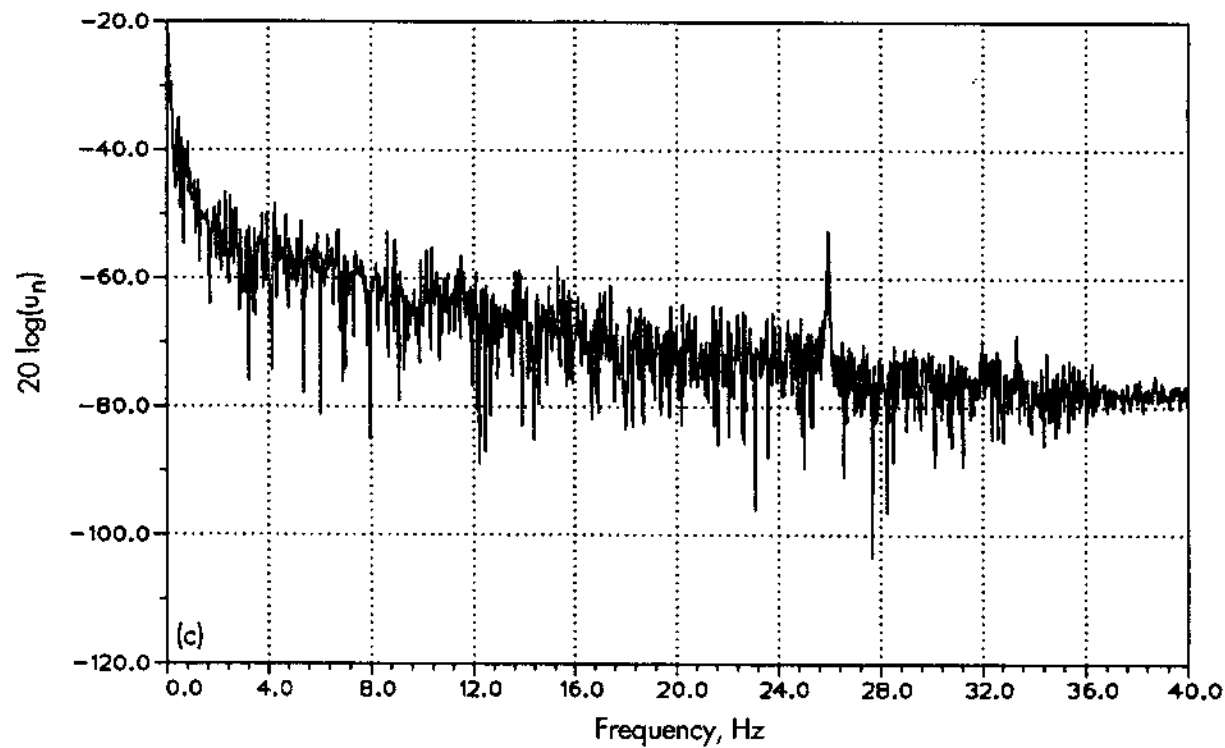


Figure 10 (concluded). (c) Spectrum.

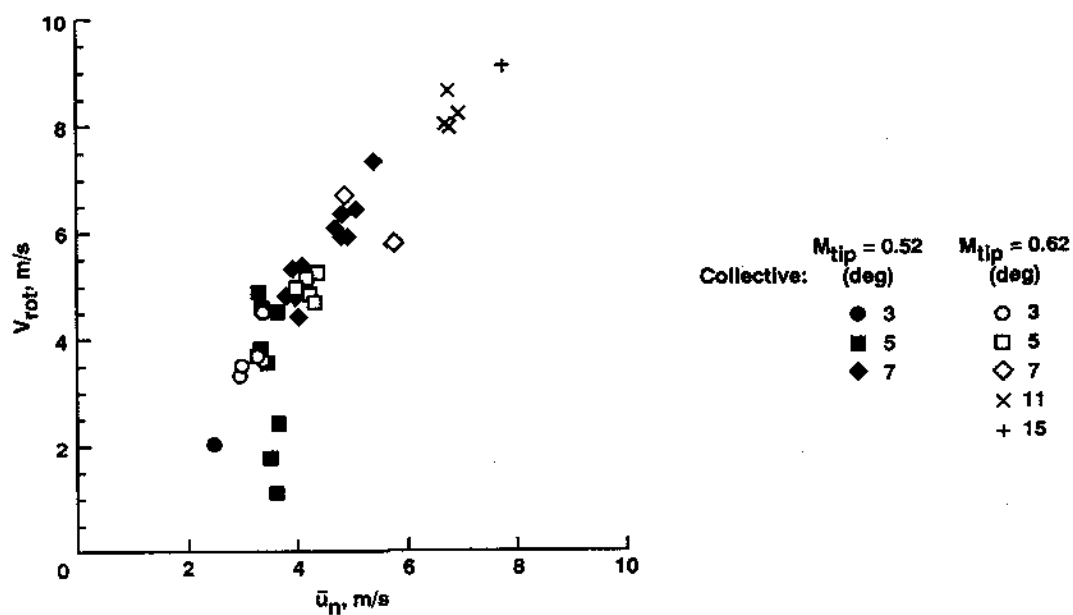


Figure 11. Rotor inflow velocity.

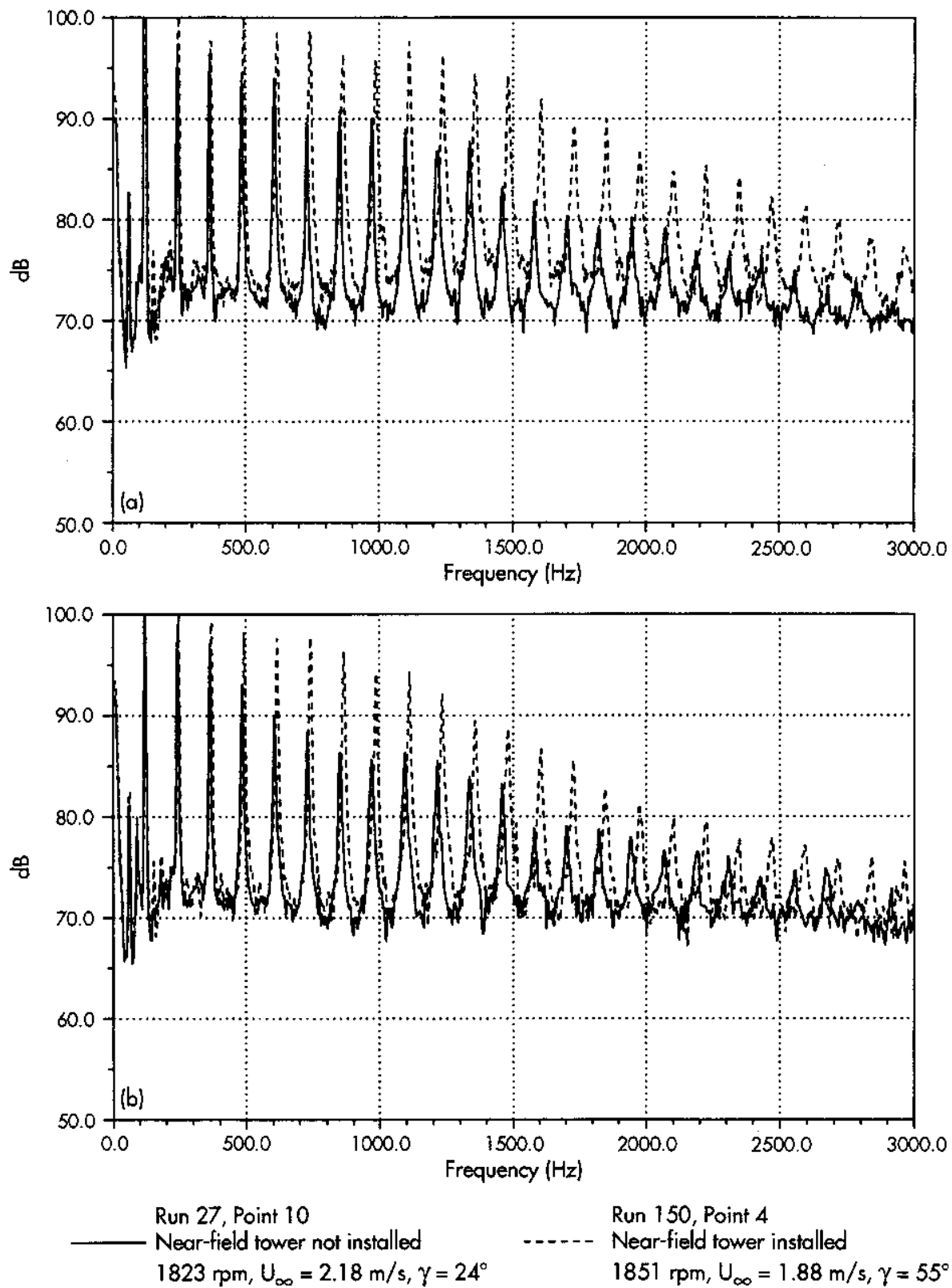


Figure 12. Effect of near-field tower on acoustic power spectra for $\theta = 15^{\circ}$, grid not installed. (a) Microphone 2, (b) microphone 8.

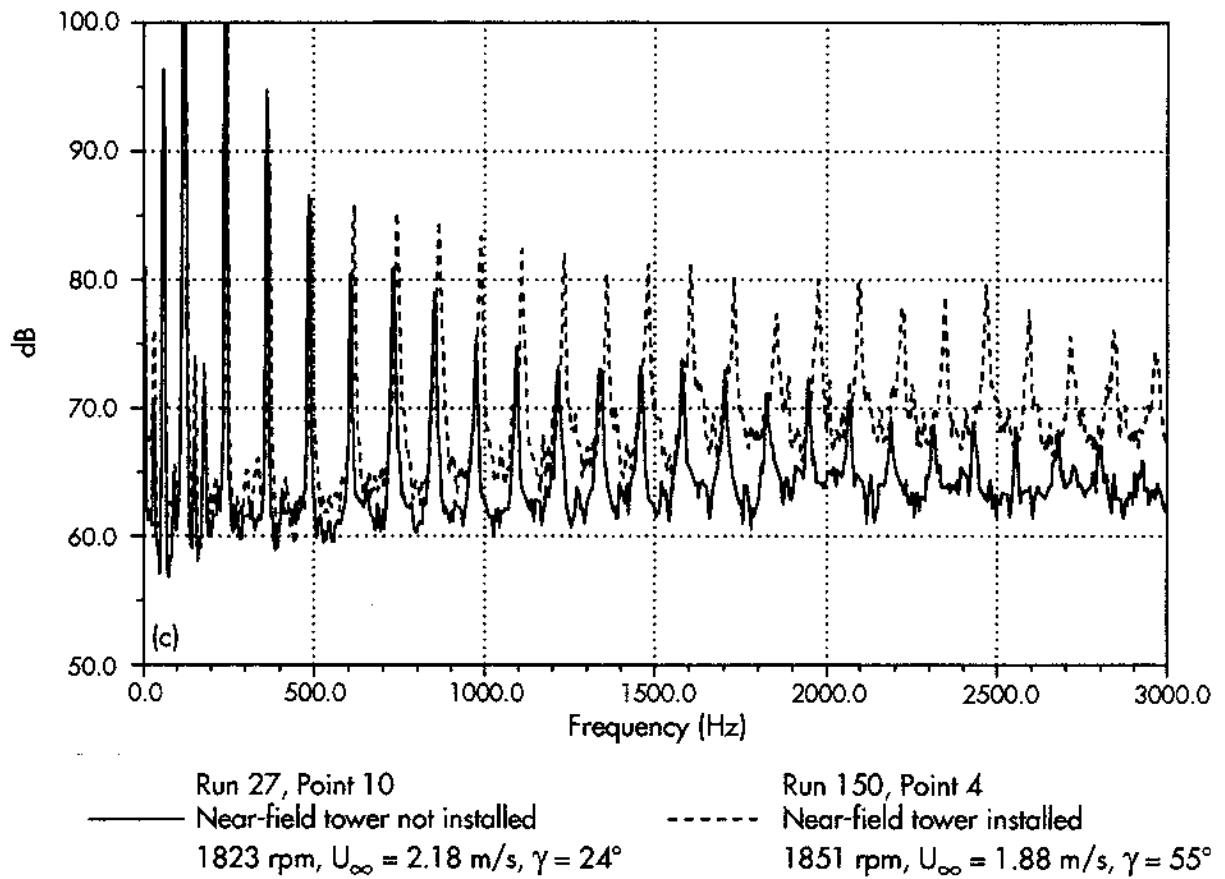
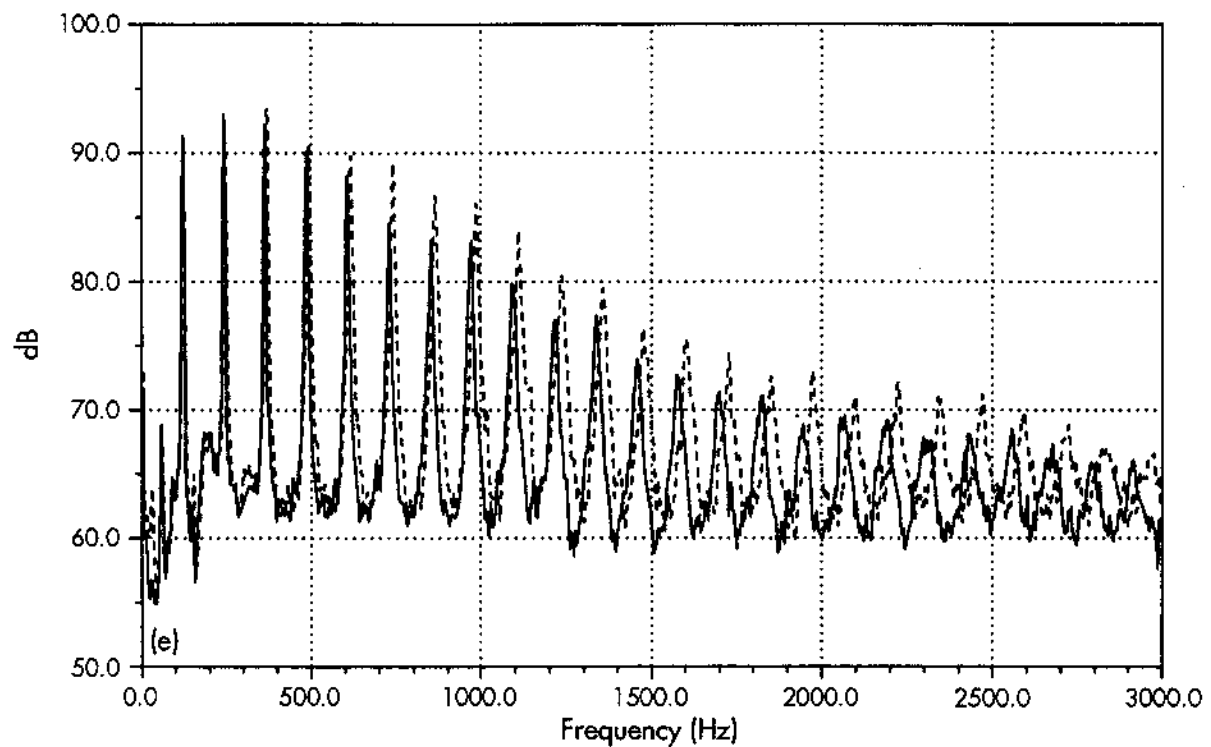
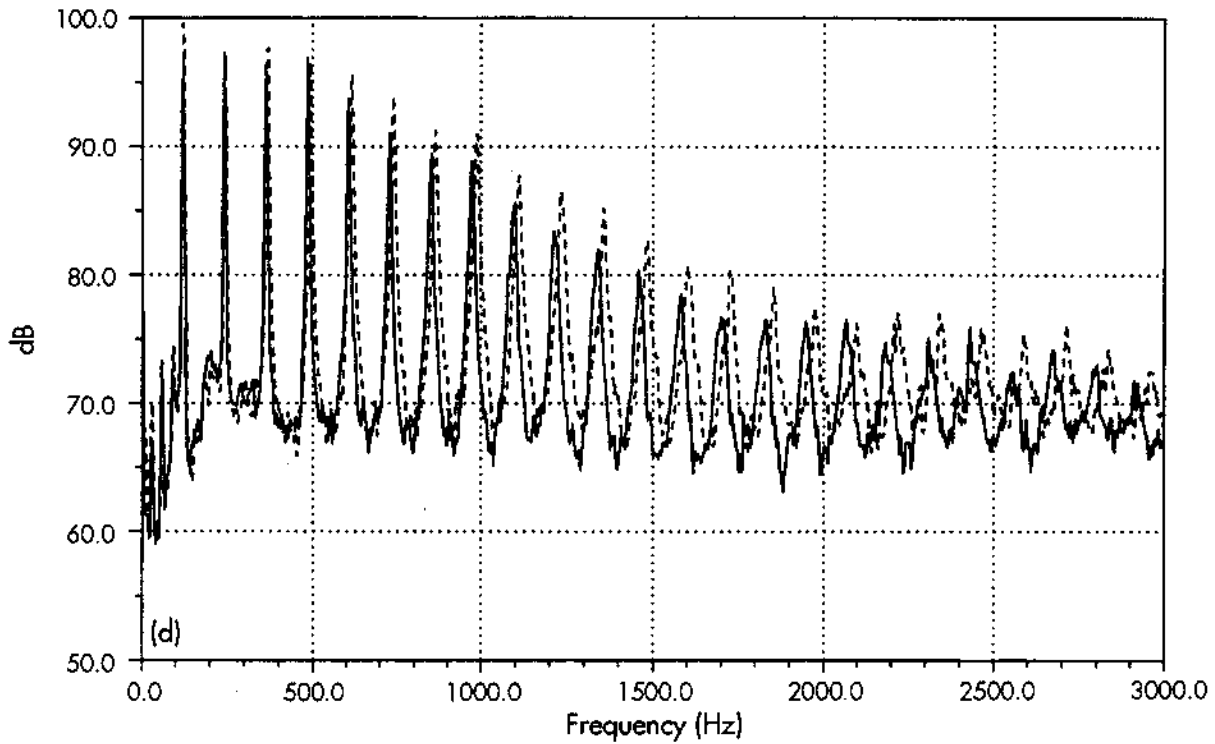


Figure 12 (continued). (c) Microphone 6.



Run 27, Point 10	Run 150, Point 4
— Near-field tower not installed	----- Near-field tower installed
1823 rpm, $U_\infty = 2.18$ m/s, $\gamma = 24^\circ$	1851 rpm, $U_\infty = 1.88$ m/s, $\gamma = 55^\circ$

Figure 12 (concluded). (d) Microphone 9, (e) microphone 11.

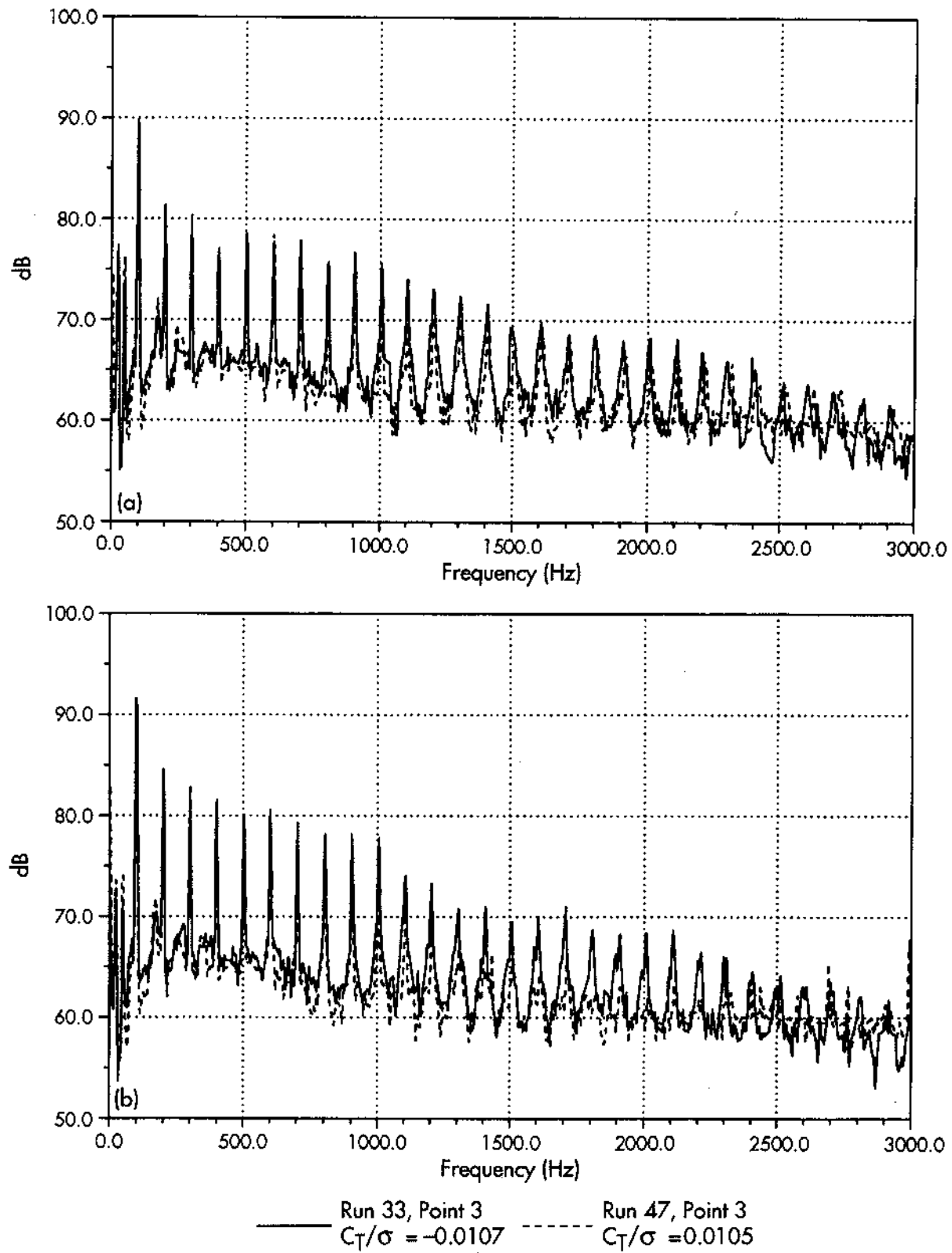
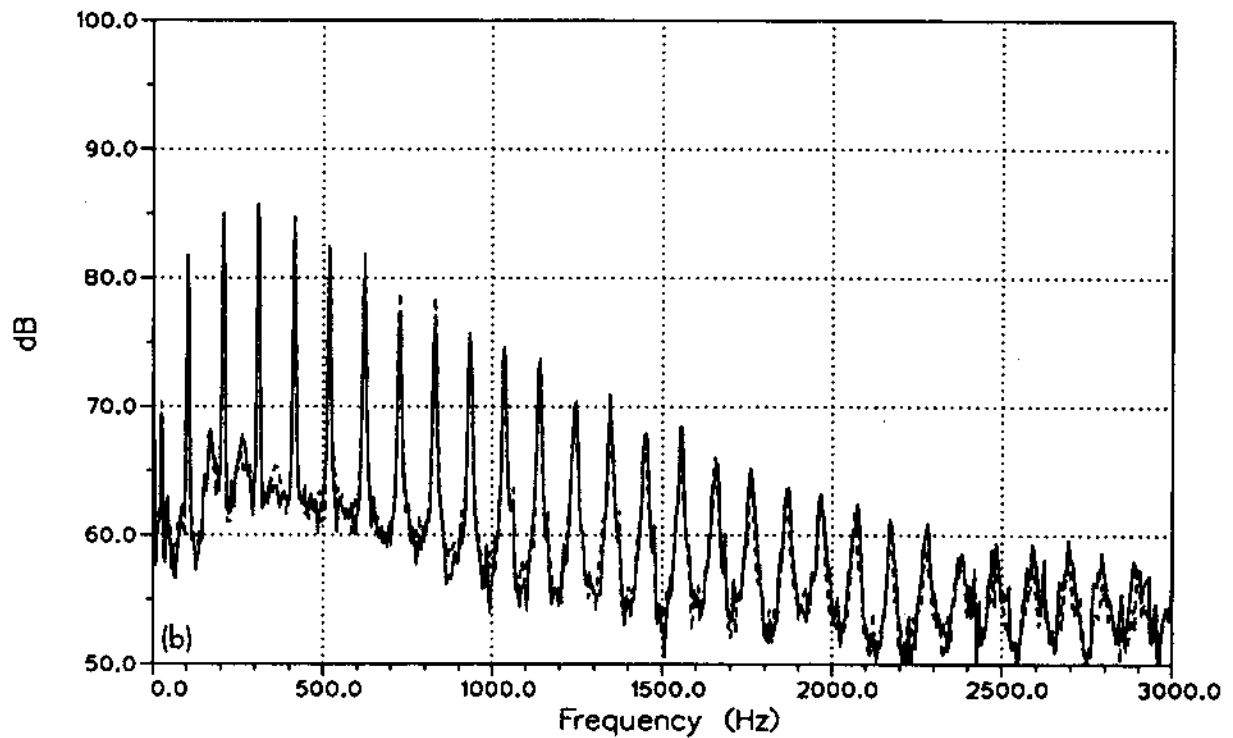
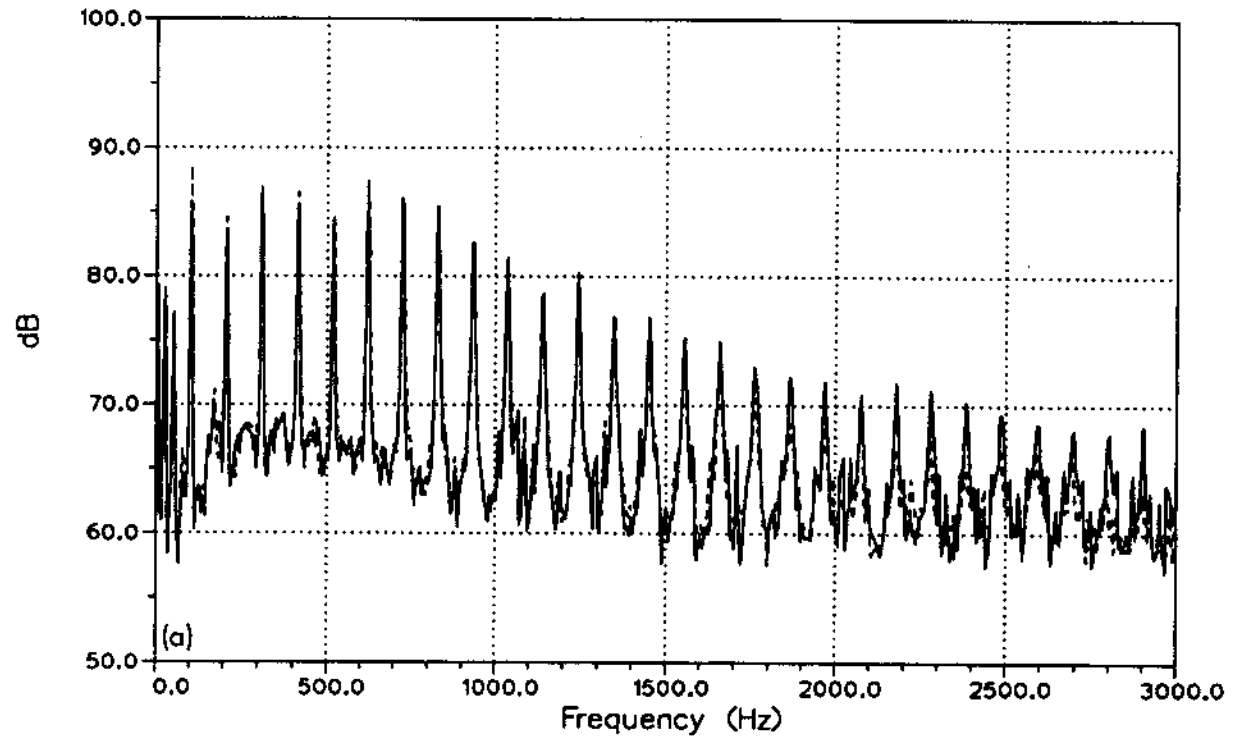


Figure 13. Effect of horizontal support on acoustic power spectra for $M_{tip} = 0.52$, near-field tower not installed, grid not installed. (a) Microphone 2, (b) microphone 8.



— Run 141, Point 4
 $U_{\infty} = 1.61 \text{ m/s}, \gamma = 35^{\circ}$

- - - Run 141, Point 5
 $U_{\infty} = 1.53 \text{ m/s}, \gamma = 30^{\circ}$

Figure 14. Consistency of acoustic power spectra for $\theta = 5^{\circ}$, $M_{tip} = 0.52$, near-field tower installed, grid not installed. (a) Microphone 2, (b) microphone 9.

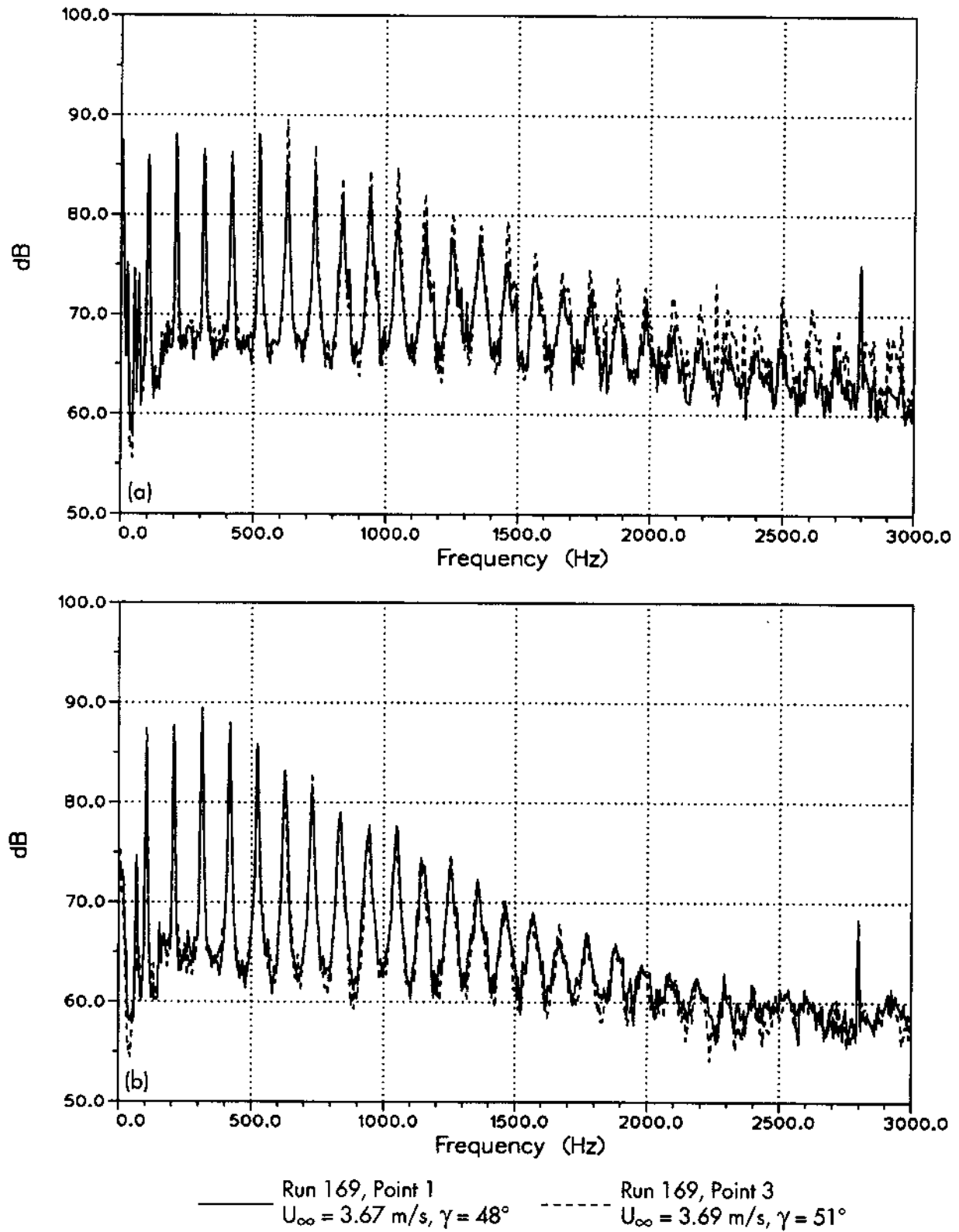


Figure 15. Consistency of acoustic power spectra for $\theta = 7^{\circ}$, $M_{tip} = 0.52$, near-field tower installed, grid not installed. (a) Microphone 2, (b) microphone 9.

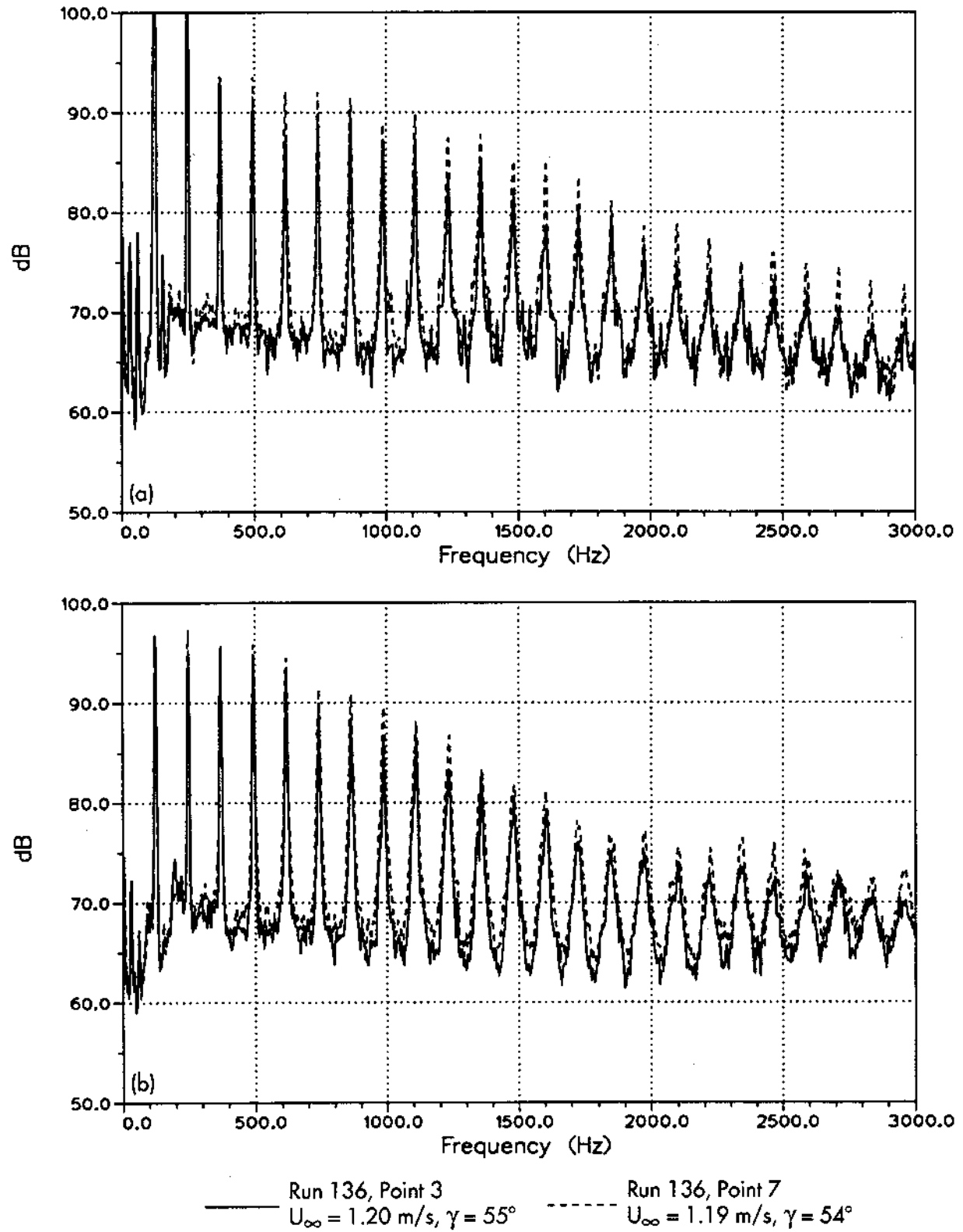


Figure 16. Consistency of acoustic power spectra for $\theta = 11^{\circ}$, $M_{tip} = 0.62$, near-field tower installed, grid not installed. (a) Microphone 2, (b) microphone 9.

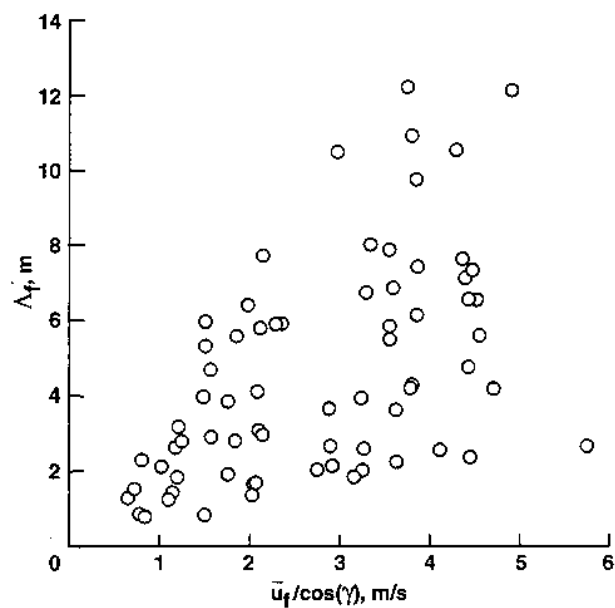


Figure 17. Far-field eddy lengths.

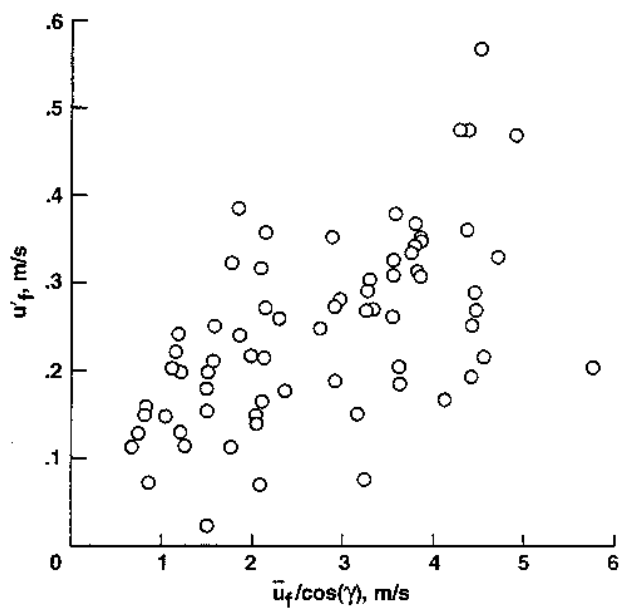


Figure 18. Far-field rms turbulence velocity.

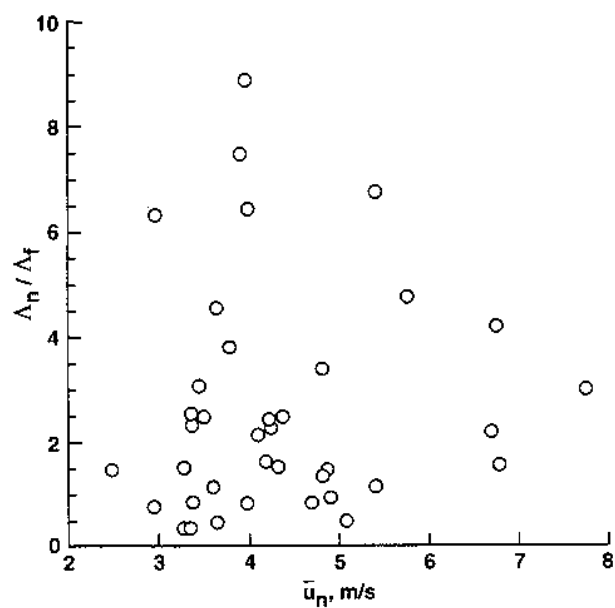


Figure 19. Longitudinal eddy length stretching ratio.

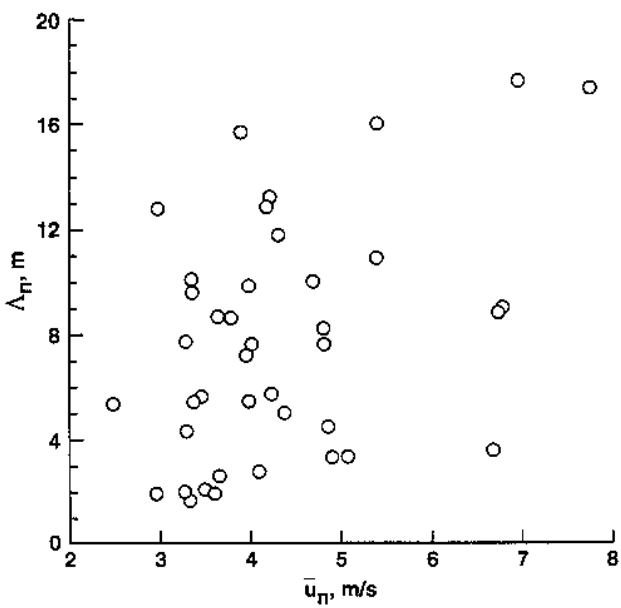


Figure 20. Near-field longitudinal eddy length.

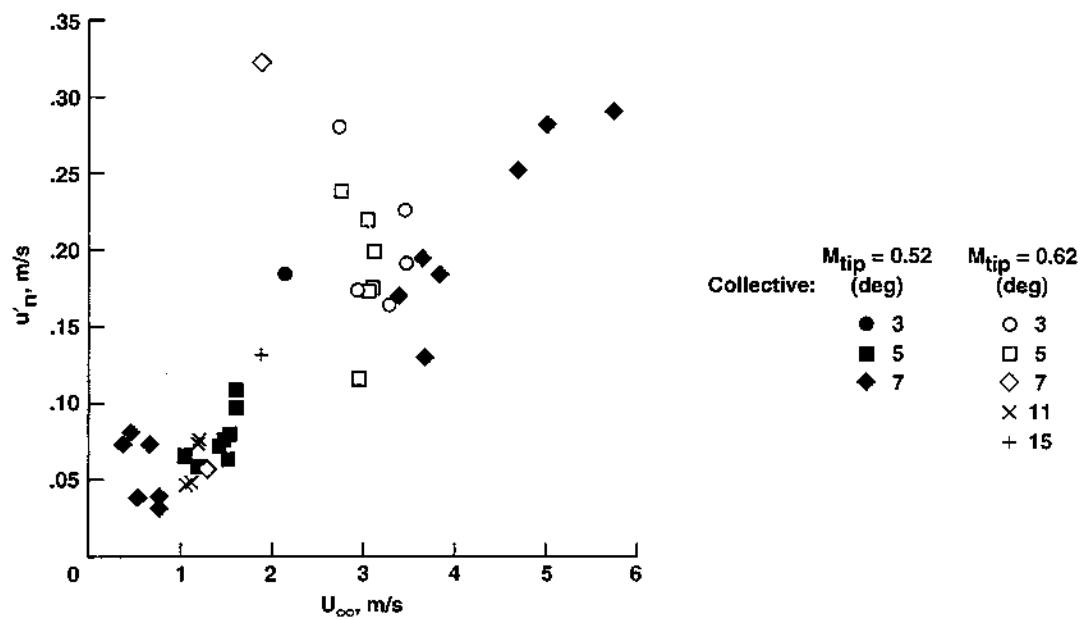


Figure 21. Near-field rms turbulence velocity.

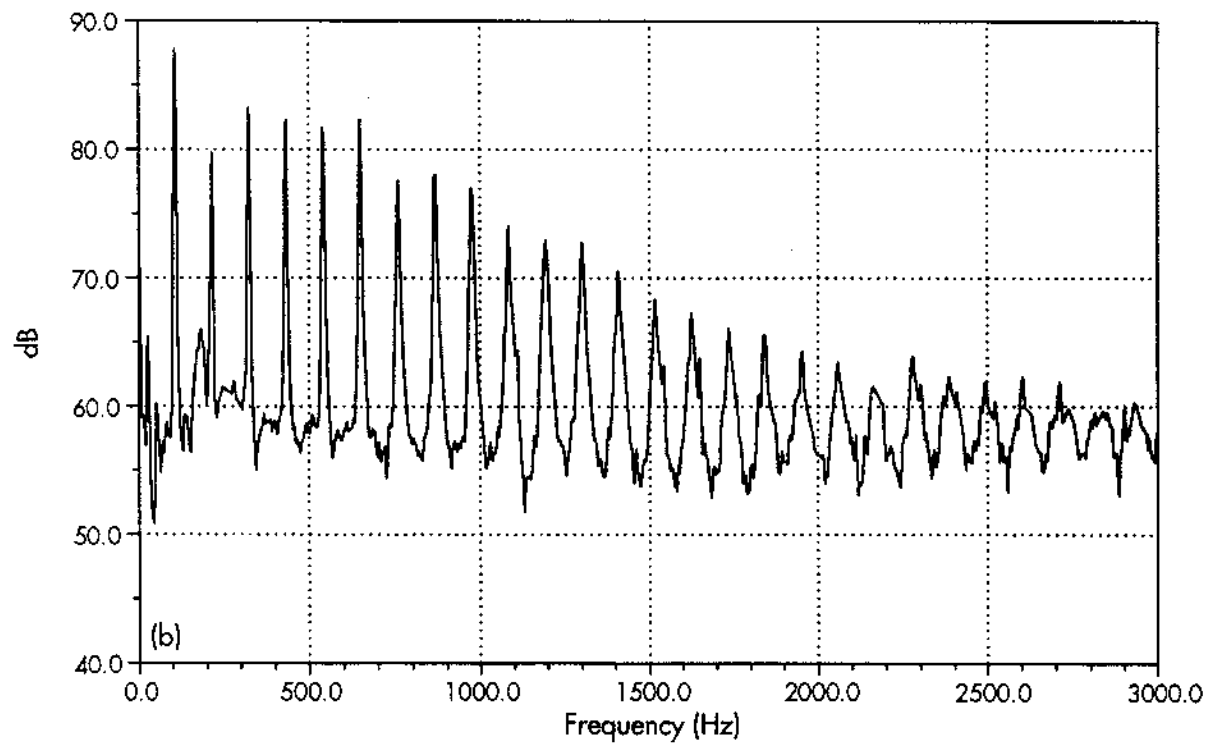
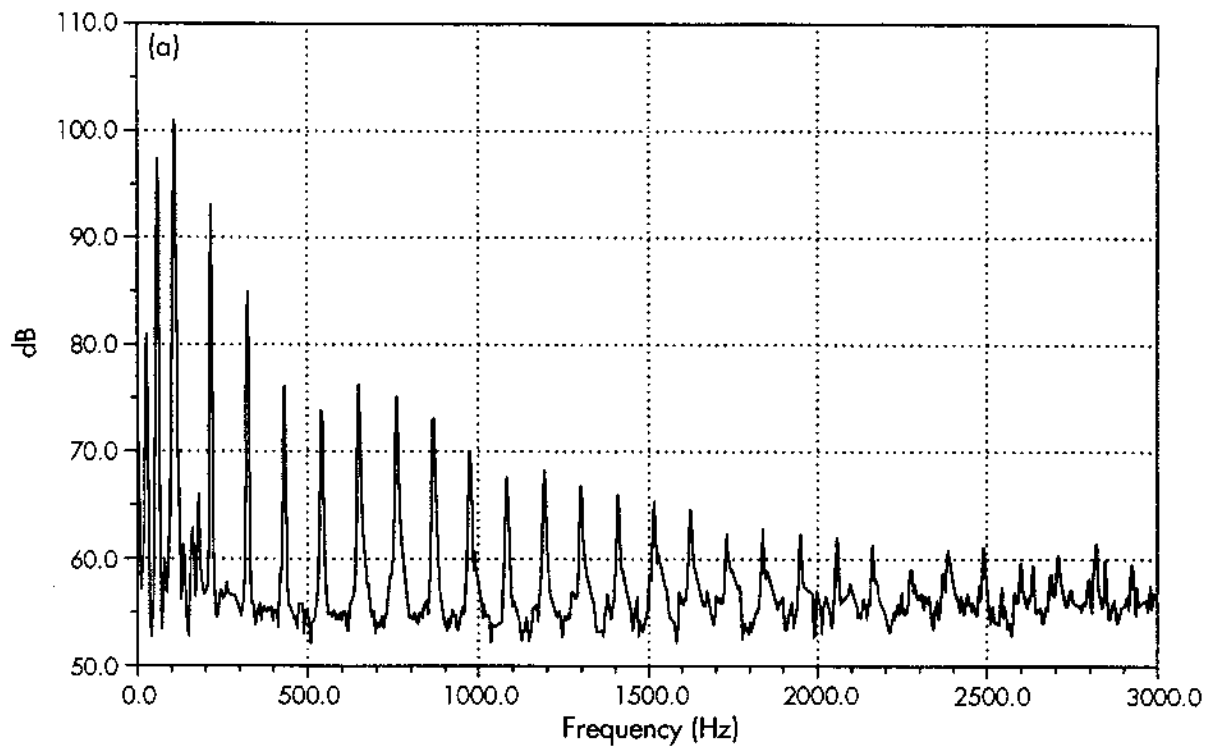


Figure 22. Power spectrum for Run 44 Point 5, $M_{tip} = 0.56$, $\theta = 11^\circ$, $U_\infty = 0.00$ m/s, near-field tower not installed, grid not installed. (a) Microphone 6, (b) microphone 11.

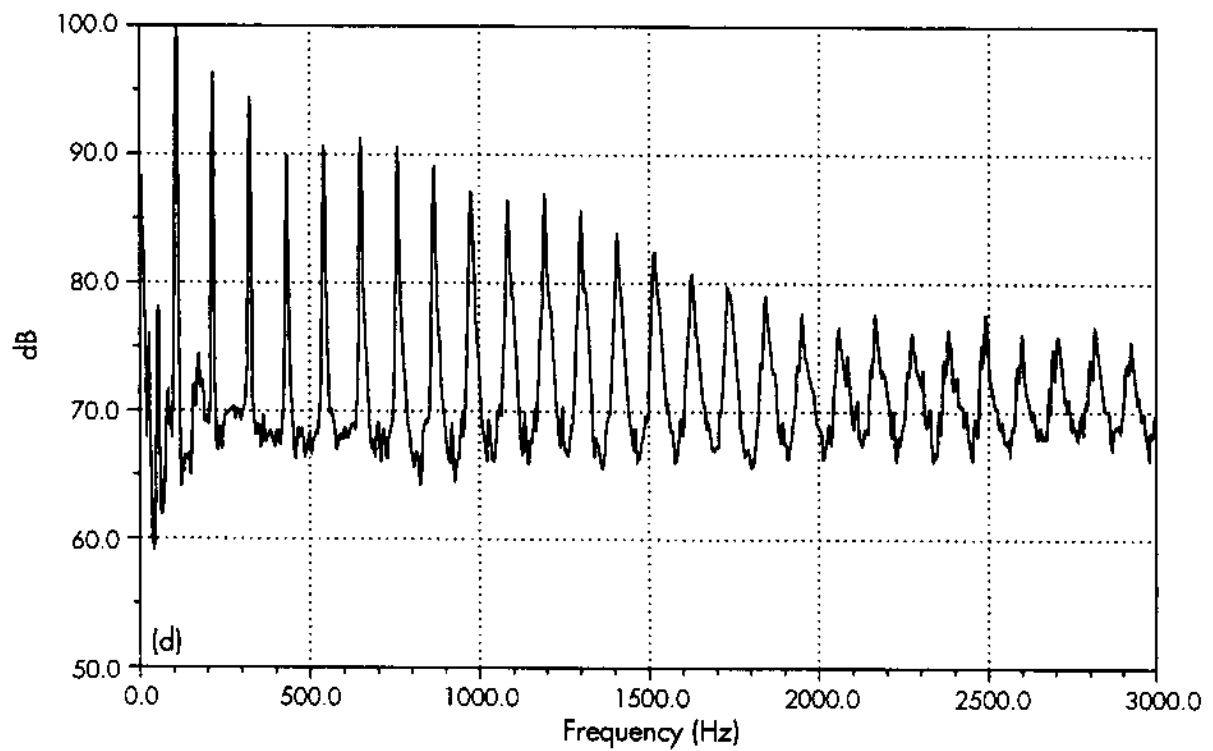
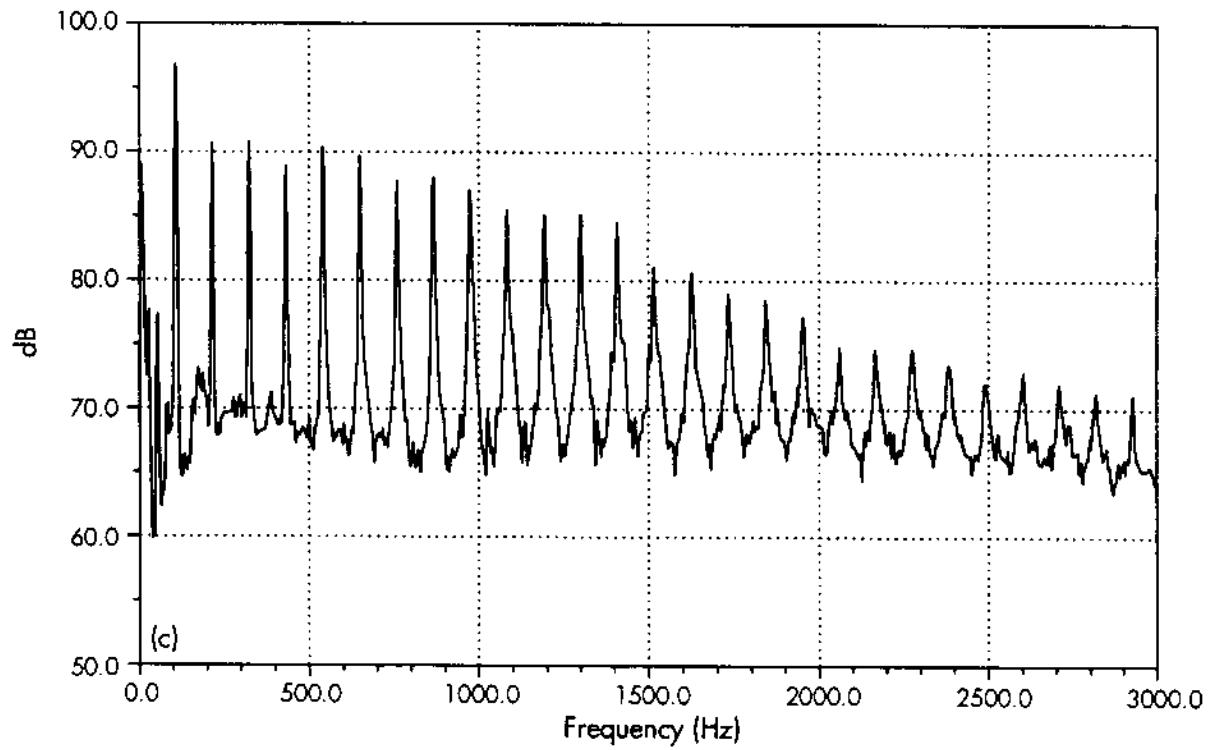


Figure 22 (concluded). (c) Microphone 2, (d) microphone 8.

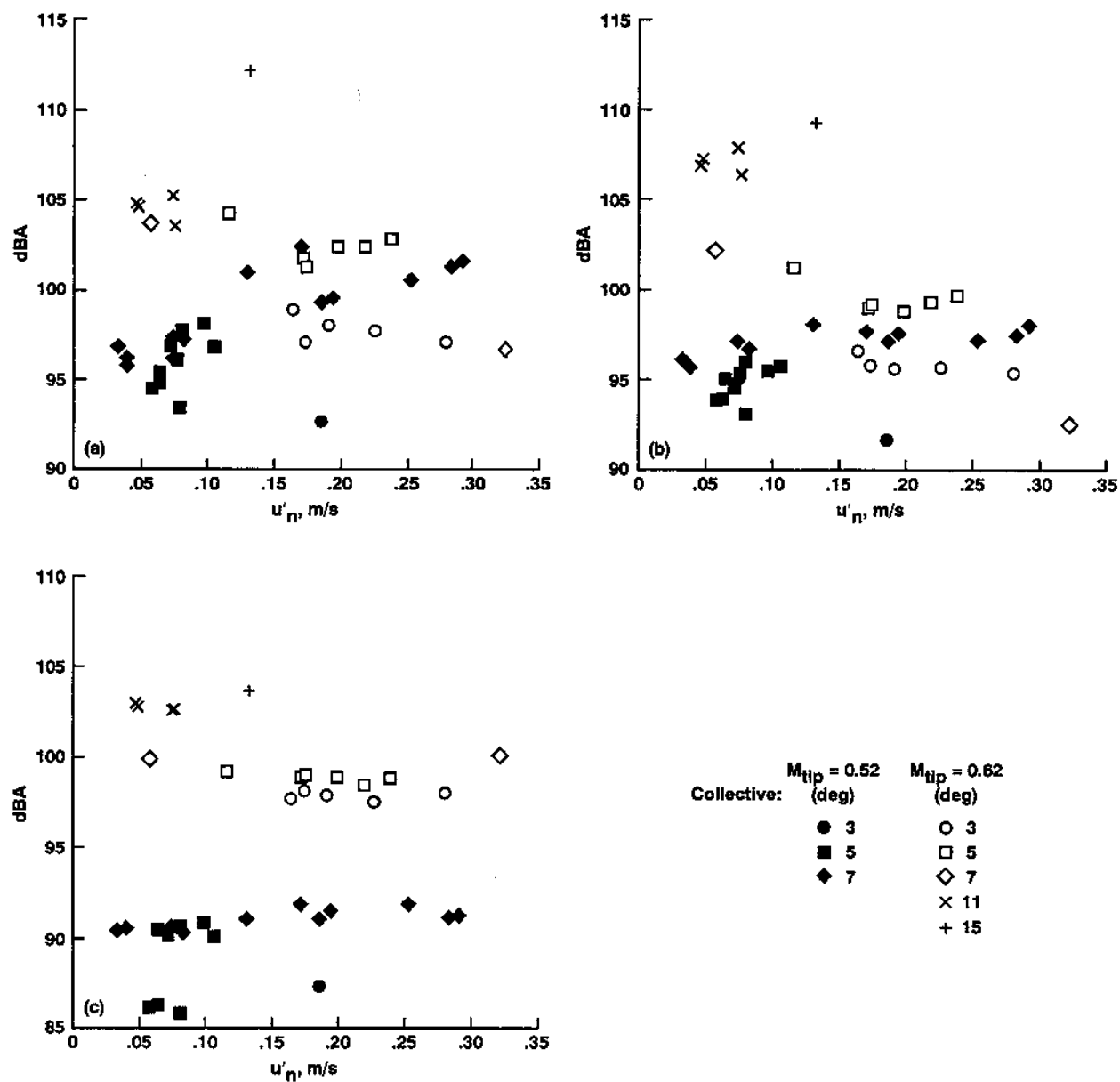


Figure 23. Measured sound level variation with rms turbulence velocity, near-field tower installed, grid not installed. (a) Microphone 2, (b) microphone 8, (c) microphone 6.

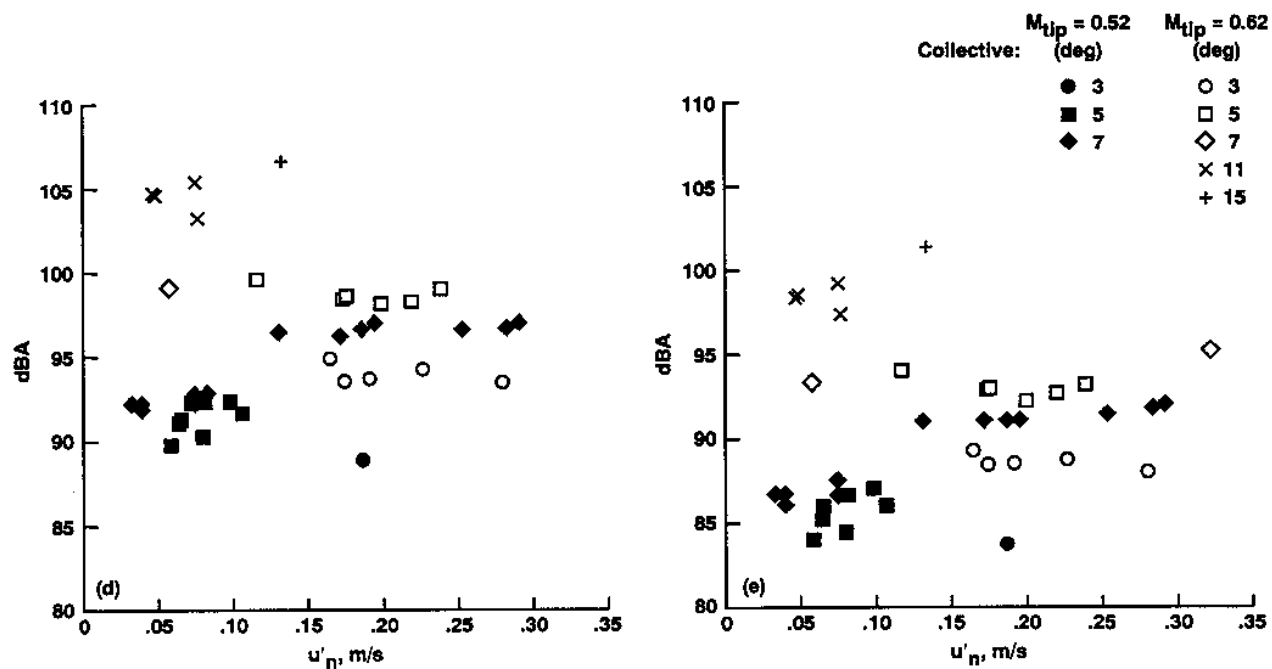


Figure 23 (concluded). (d) Microphone 9, (e) microphone 11.

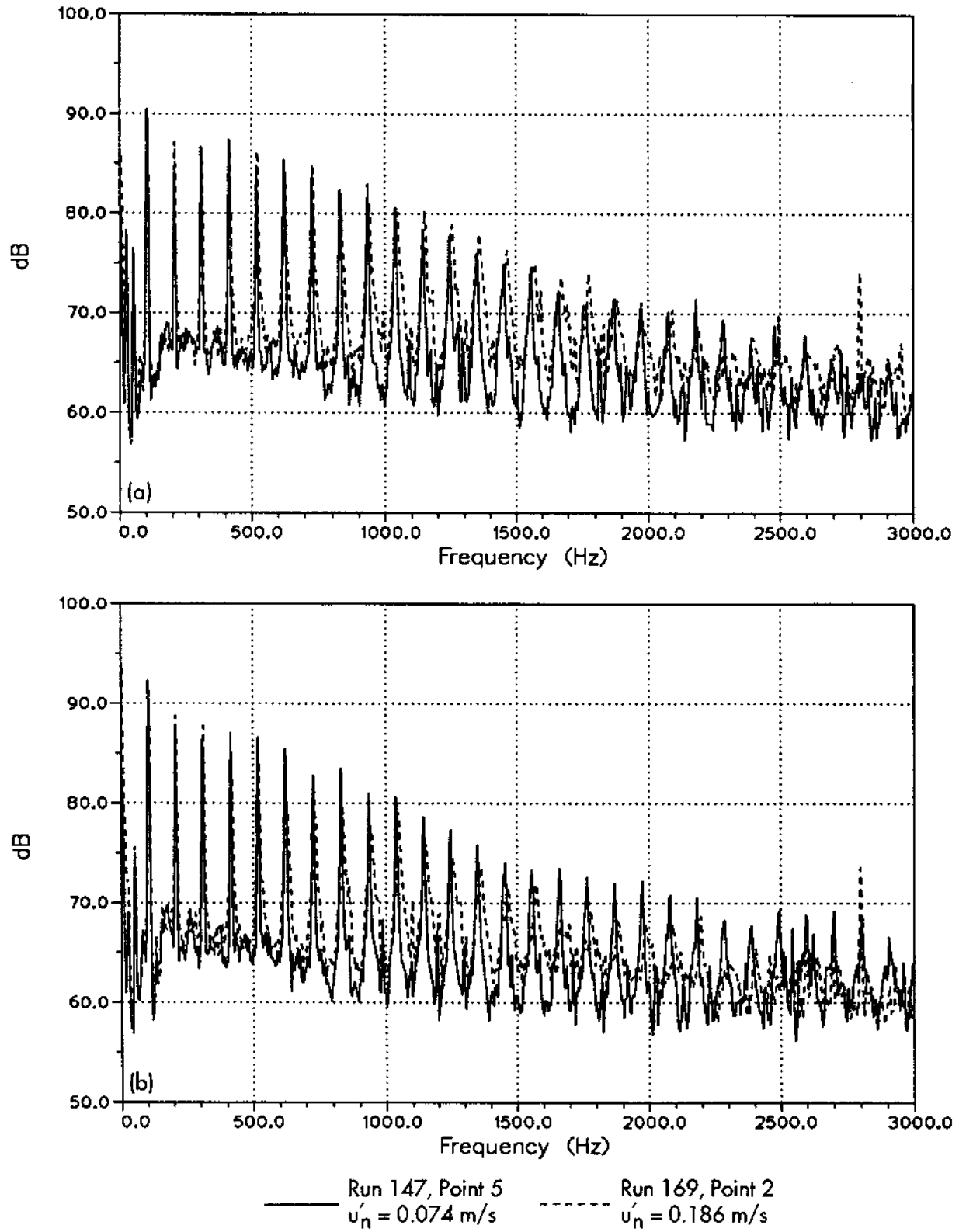


Figure 24. Effect of near-field rms turbulence velocity on acoustic power spectra for $\theta = 7^\circ$, $M_{tip} = 0.52$, near-field tower installed, grid not installed. (a) Microphone 2, (b) microphone 8.

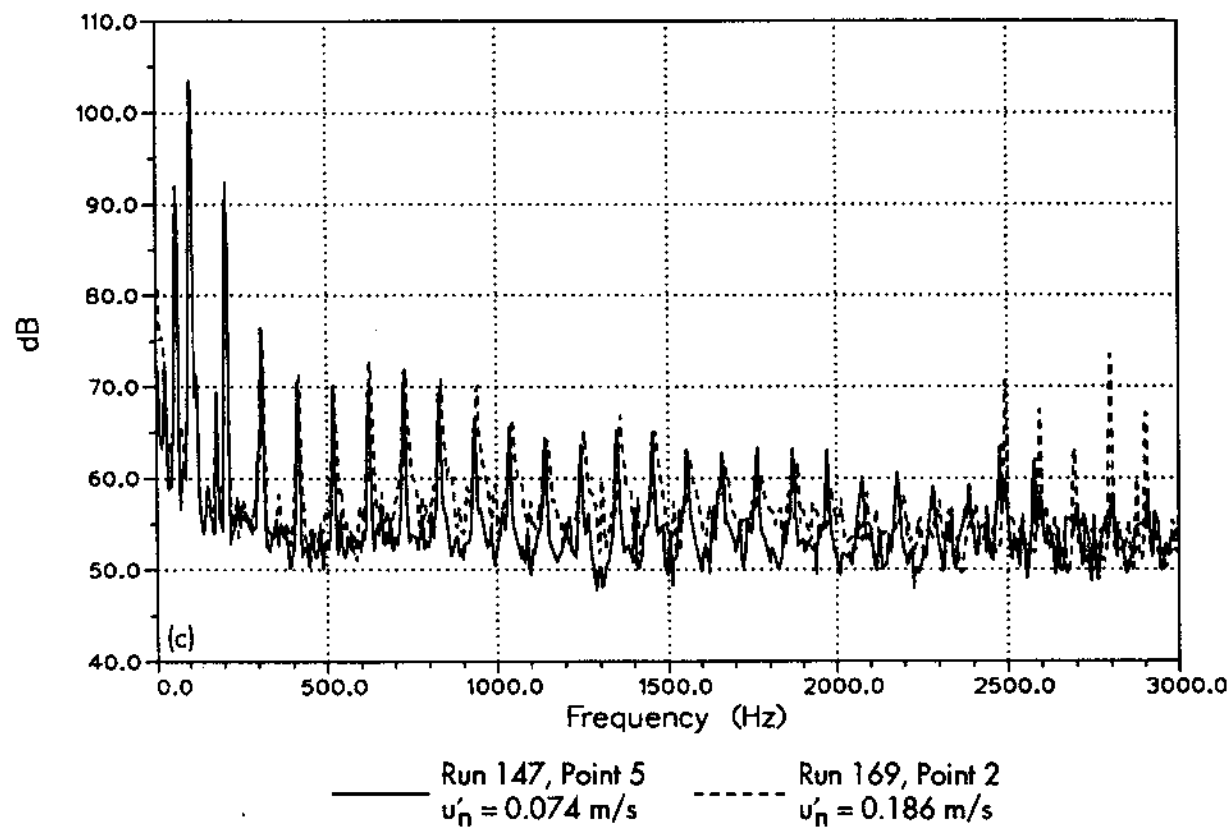
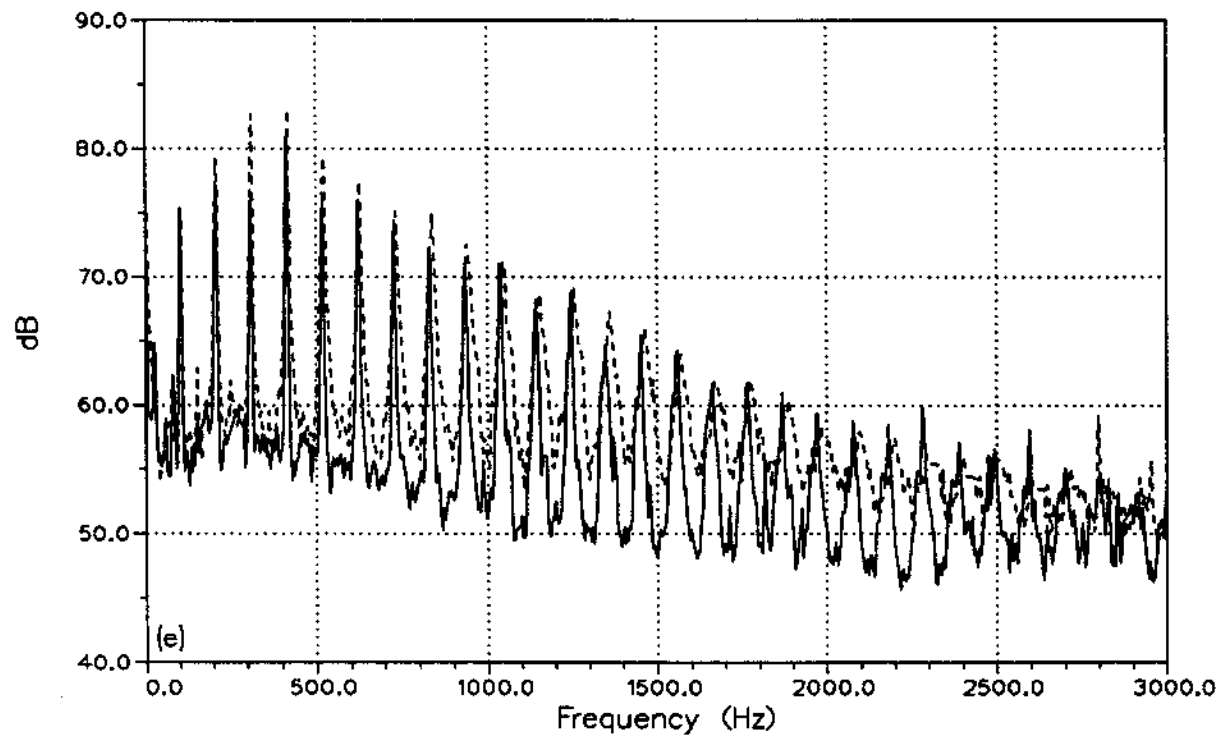
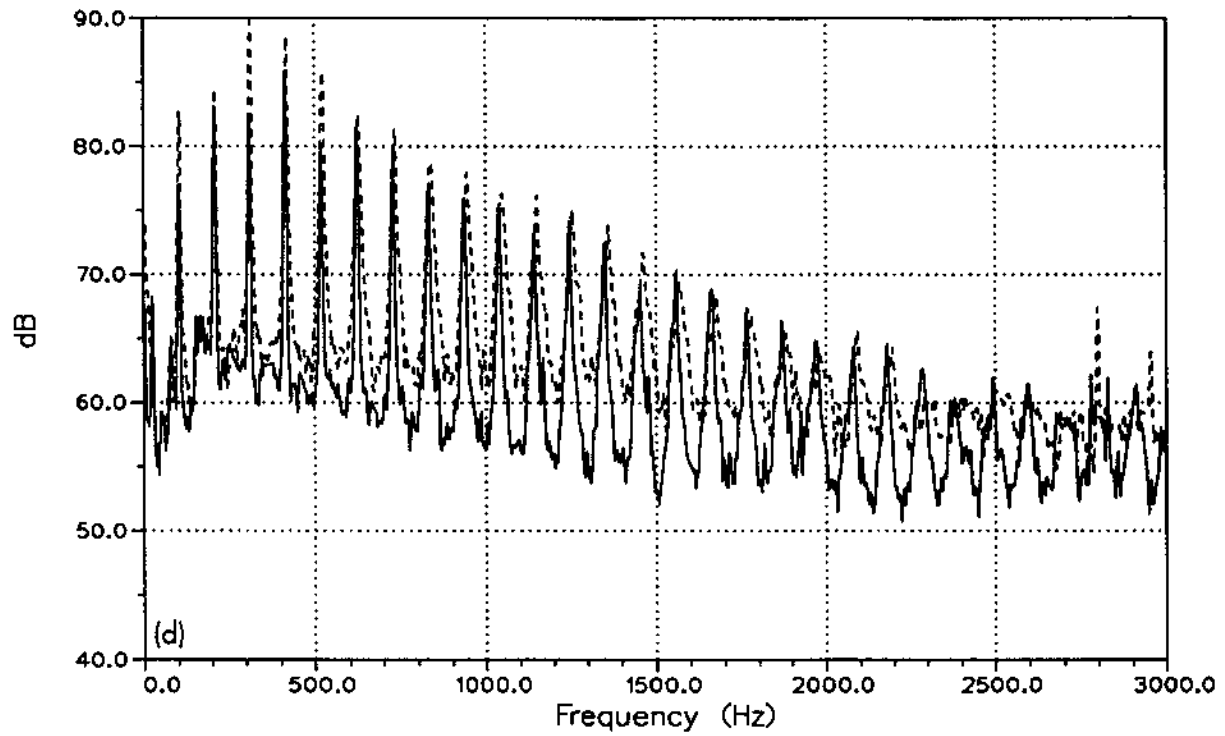


Figure 24 (continued). (c) Microphone 6.



— Run 147, Point 5
 $u'_n = 0.074 \text{ m/s}$

- - - Run 169, Point 2
 $u'_n = 0.186 \text{ m/s}$

Figure 24 (concluded). (d) Microphone 9, (e) microphone 11.

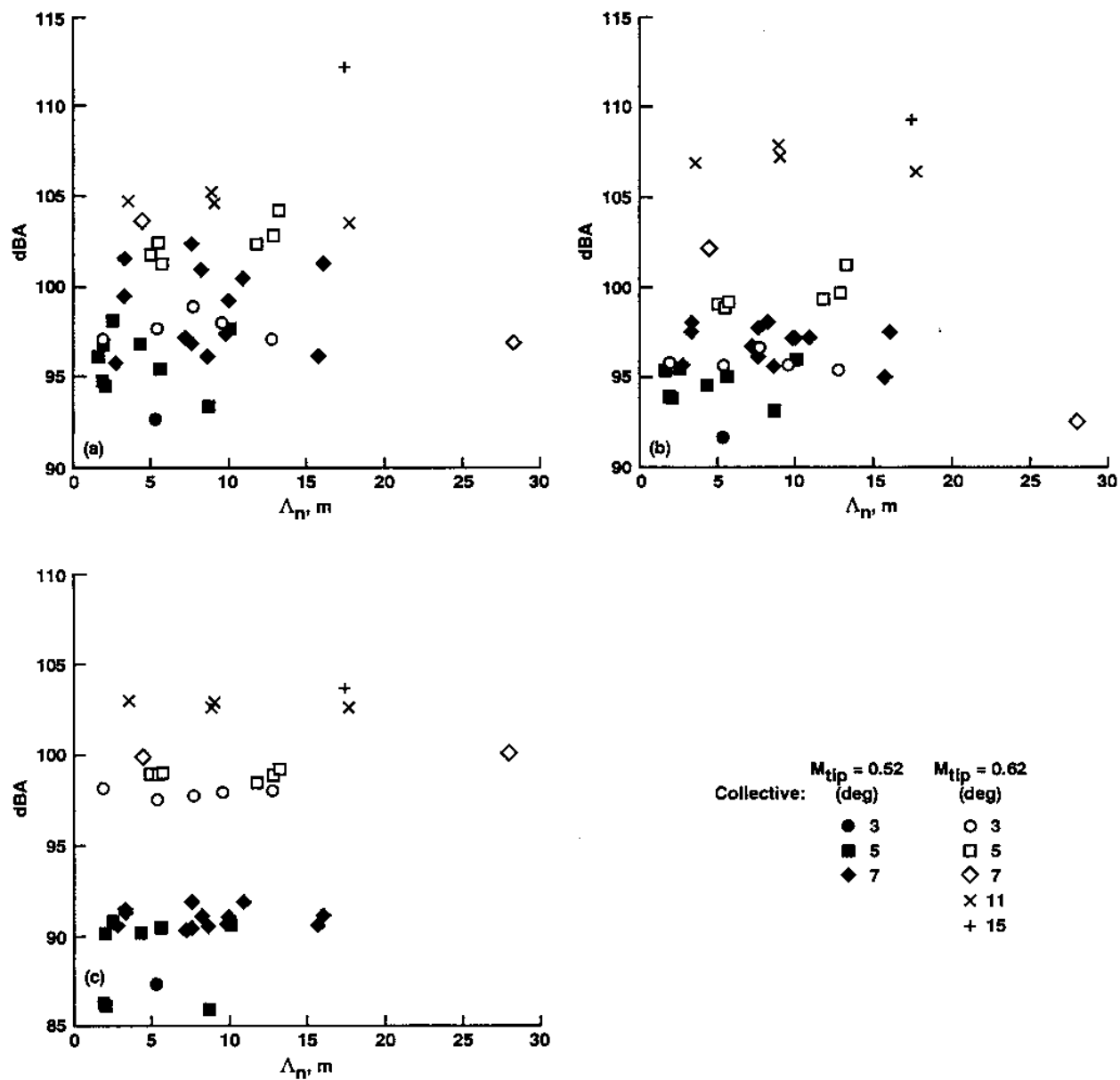
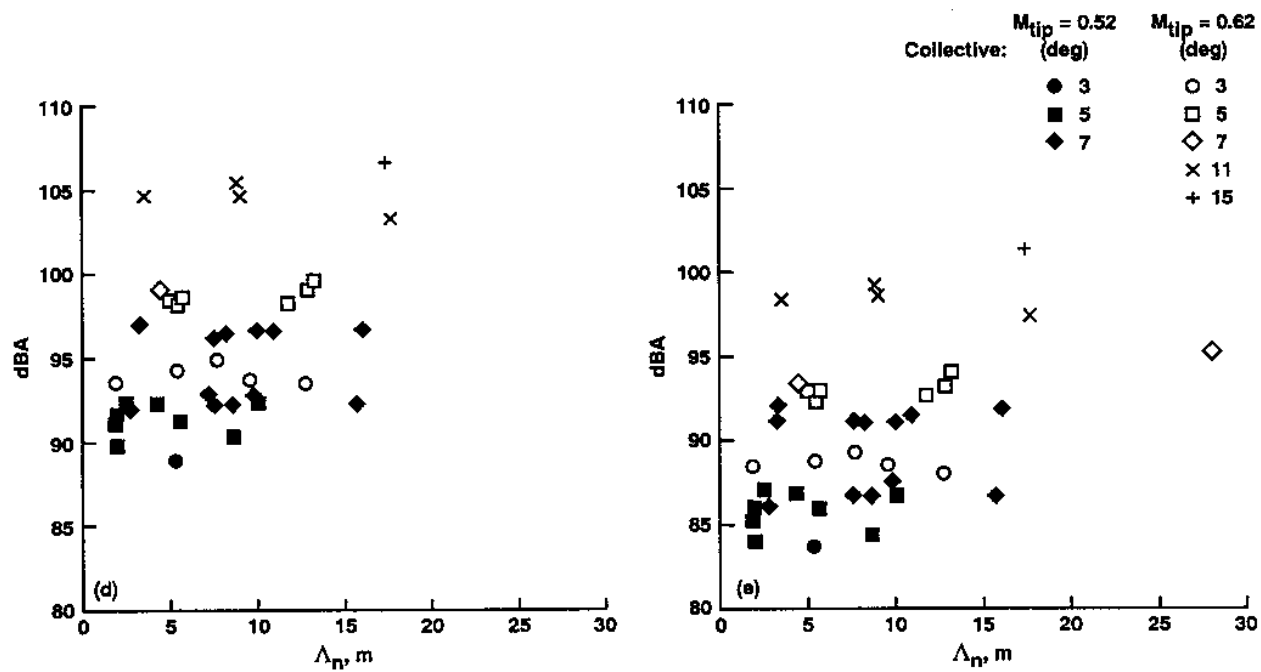


Figure 25. Measured sound level variation with near-field eddy length, near-field tower installed, grid not installed. (a) Microphone 2, (b) microphone 8, (c) microphone 6.



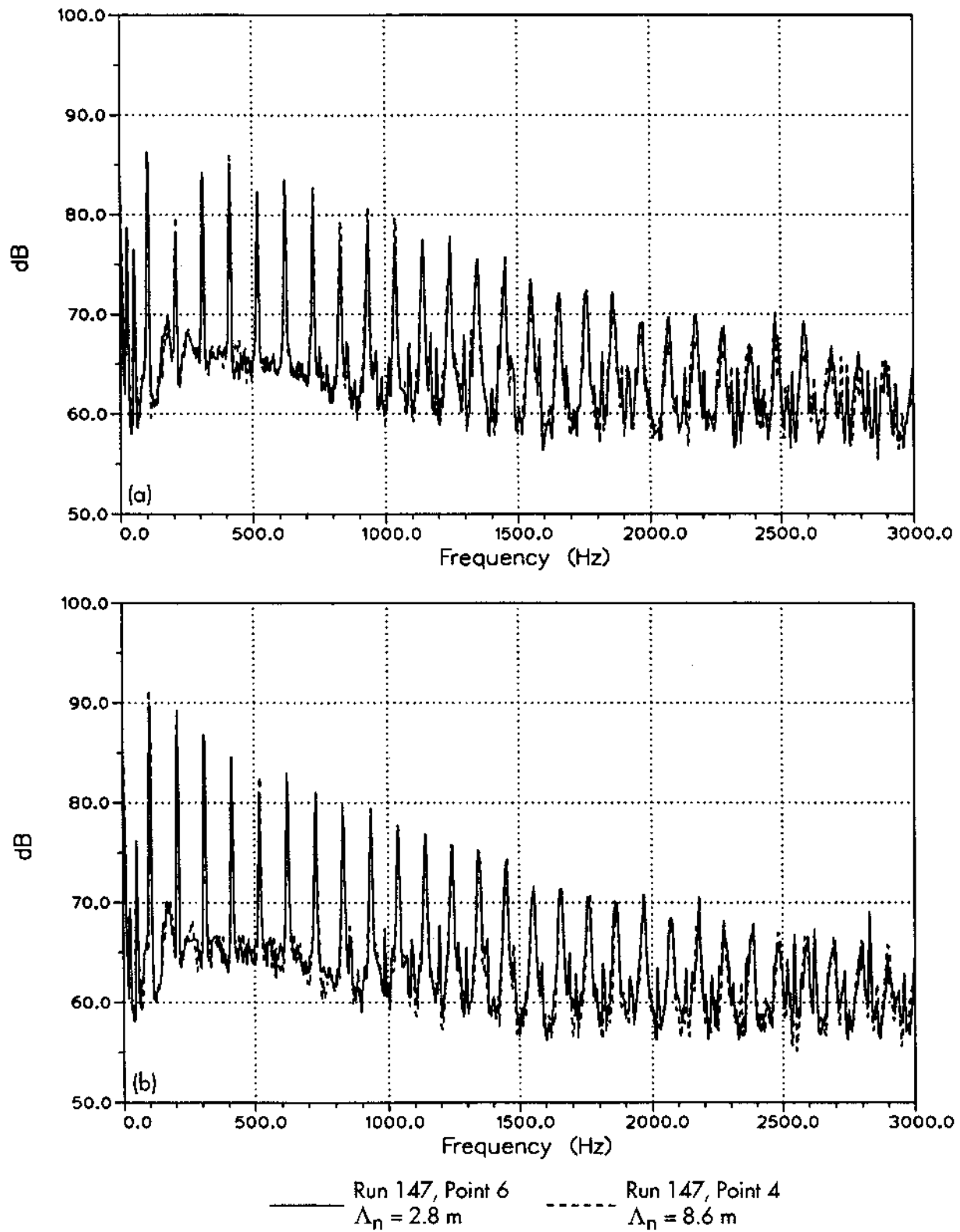


Figure 26. Effect of near-field eddy length on acoustic power spectra for $\theta = 7^\circ$, $M_{tip} = 0.52$. Near-field tower installed, grid not installed. (a) Microphone 2, (b) microphone 8.

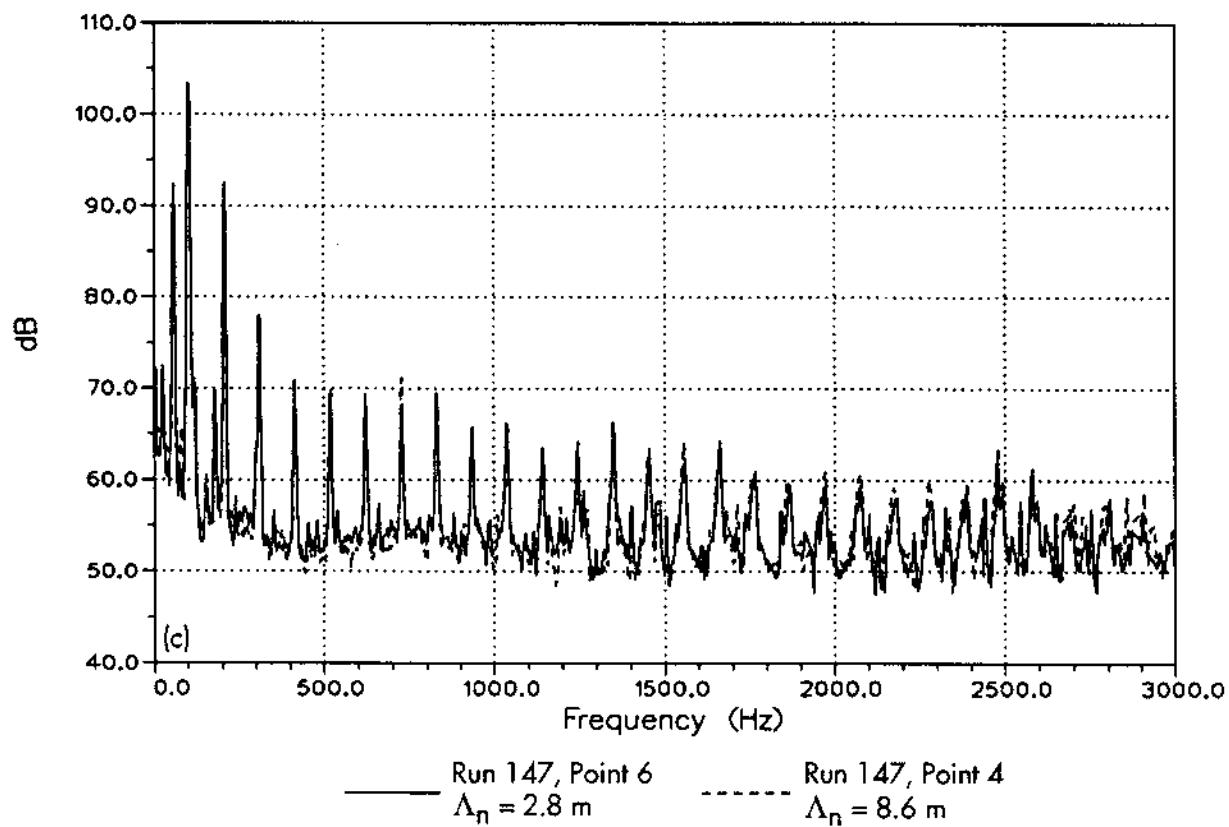


Figure 26 (continued). (c) Microphone 6.

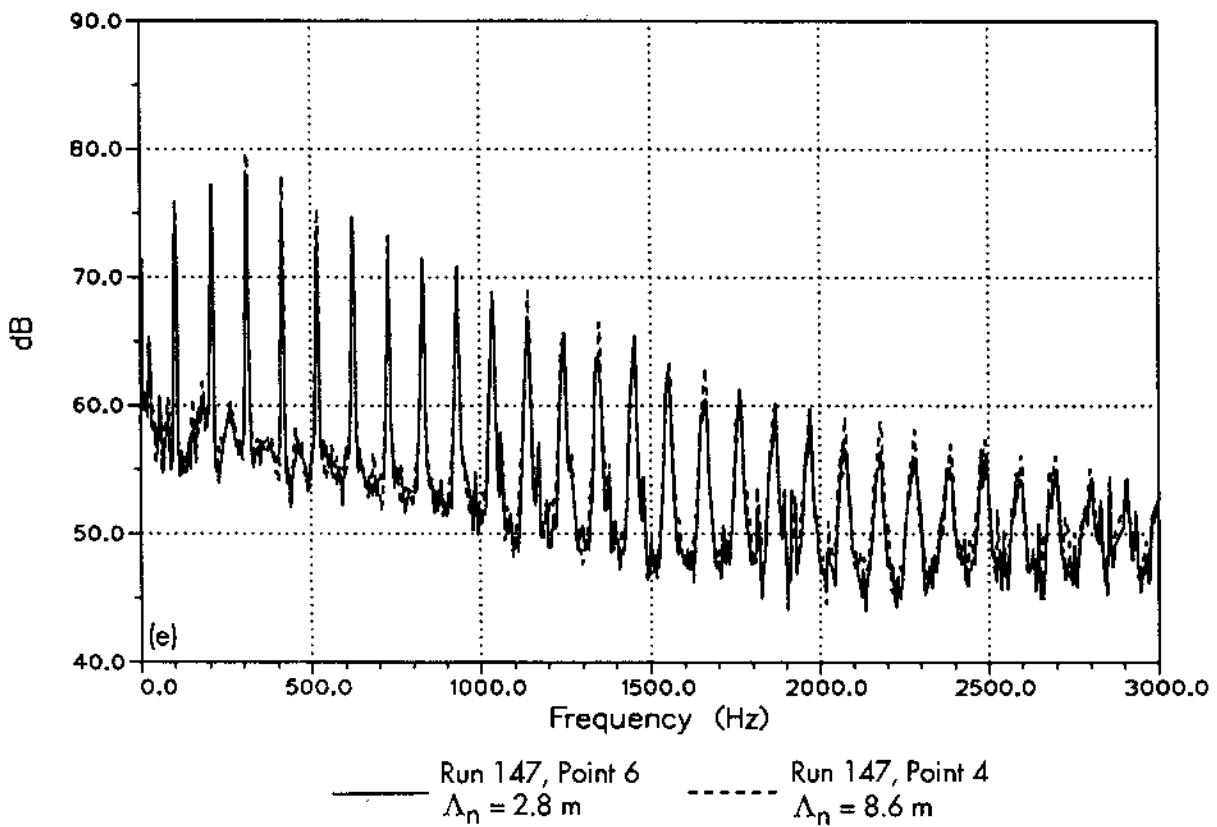
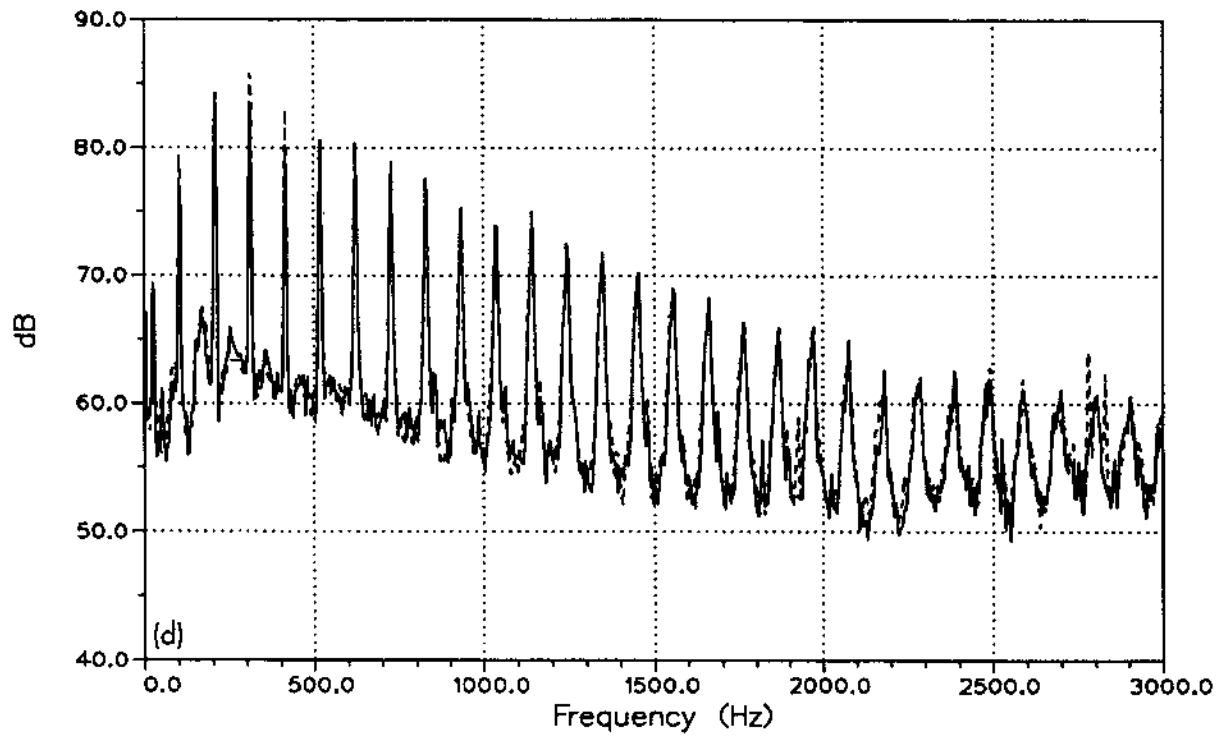


Figure 26 (concluded). (d) Microphone 9, (e) microphone 11.

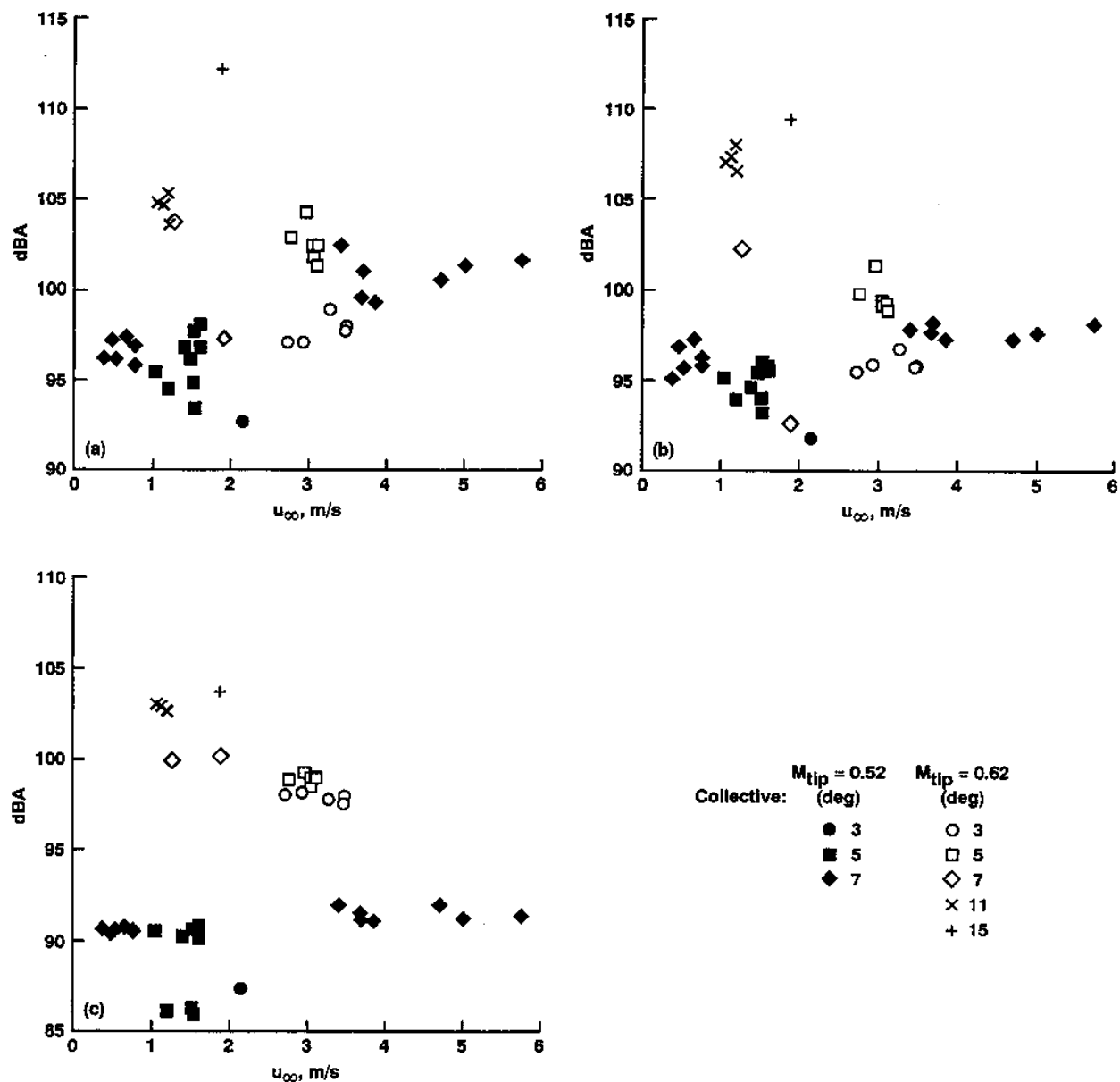


Figure 27. Measured sound level variation with atmospheric wind speed. Near-field tower installed, grid not installed.
 (a) Microphone 2, (b) microphone 8, (c) microphone 6.

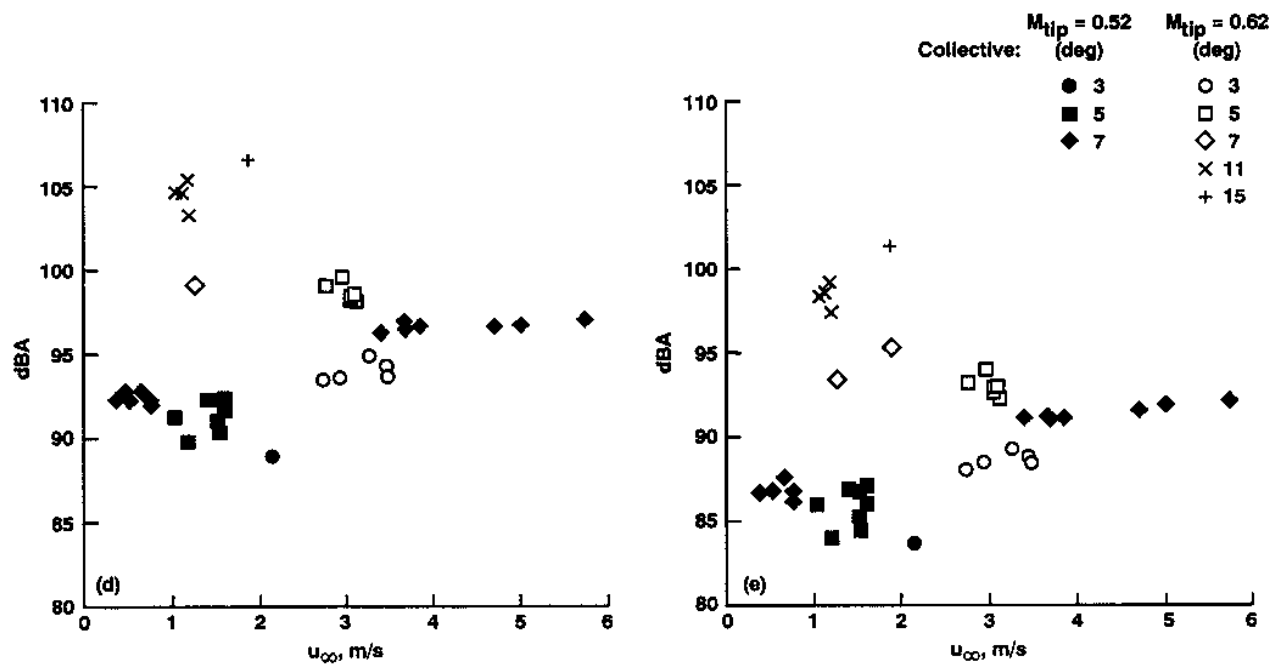


Figure 27 (concluded). (d) Microphone 9, (e) microphone 11.

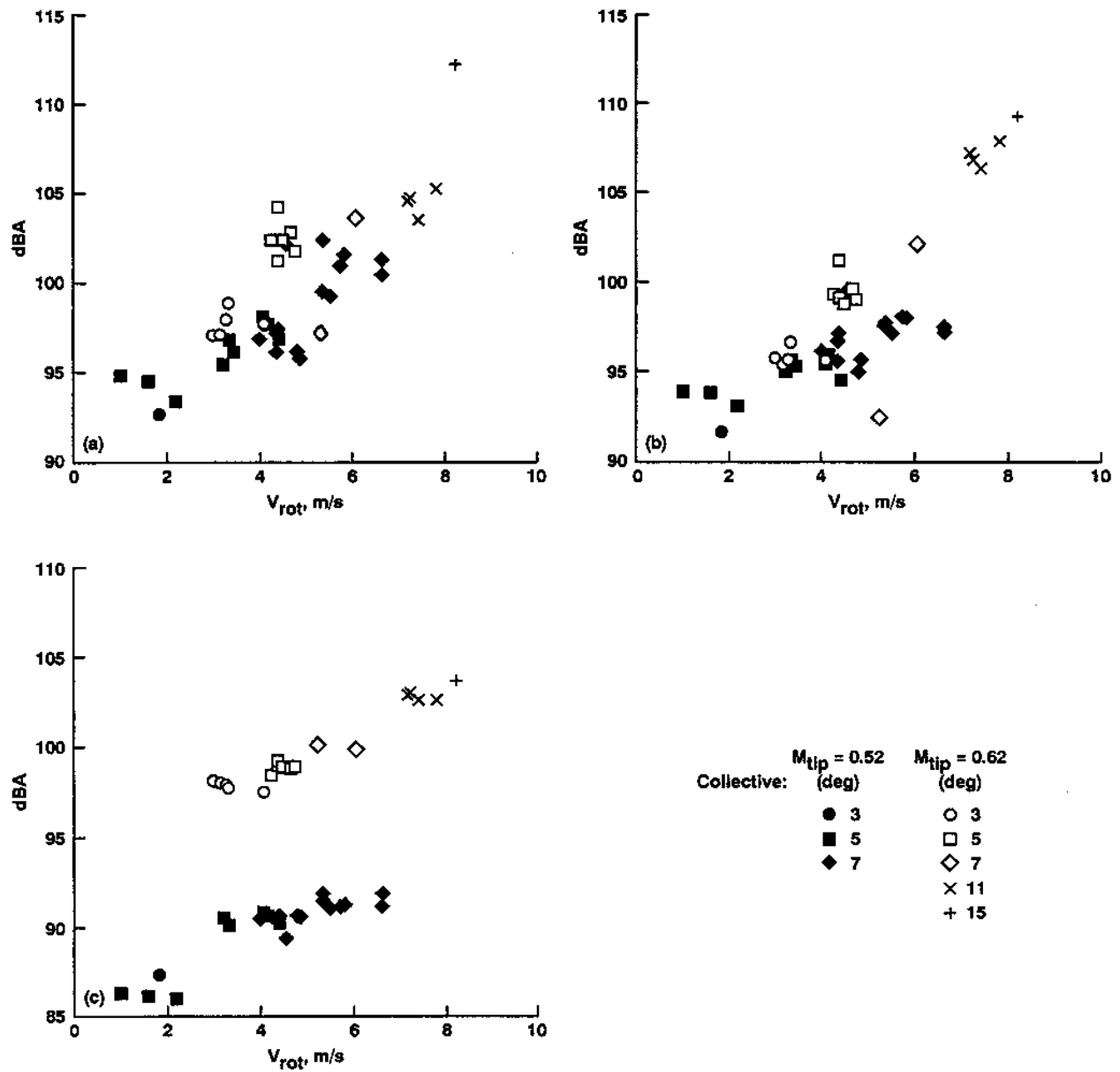


Figure 28. Measured sound level variation with rotor inflow velocity. Near-field tower installed, grid not installed. (a) Microphone 2, (b) microphone 8, (c) microphone 6.

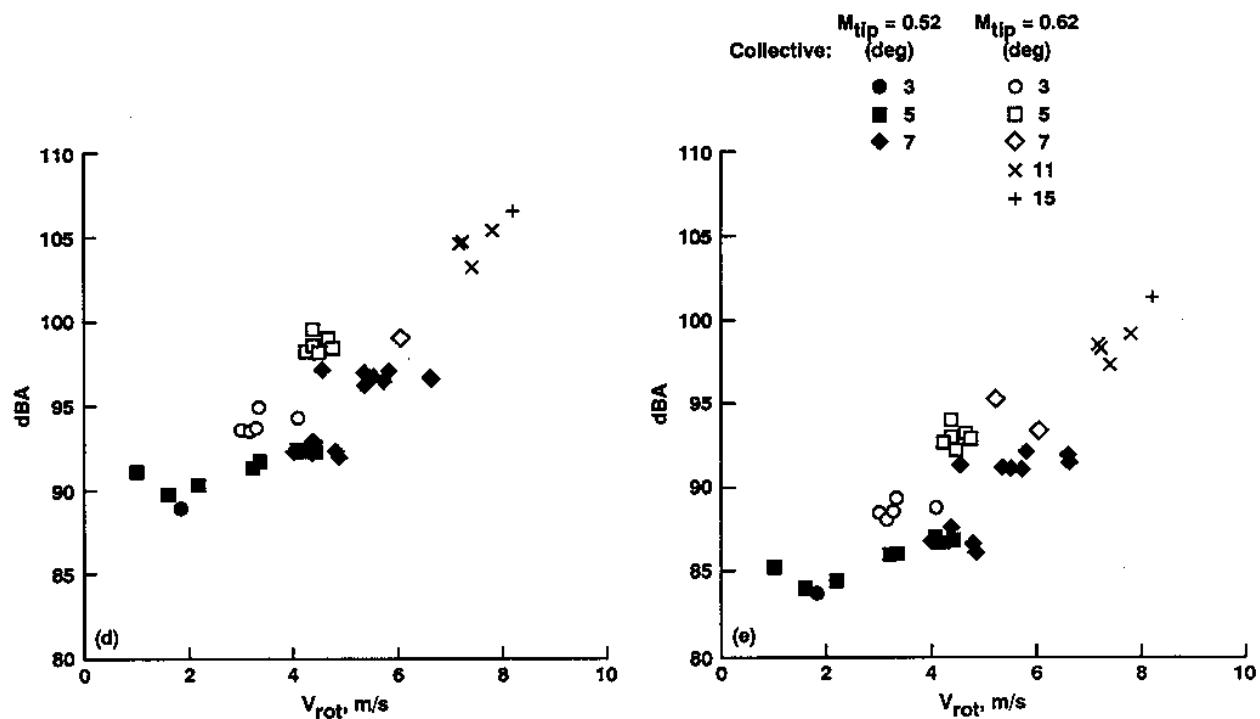


Figure 28 (concluded). (d) Microphone 9, (e) microphone 11.

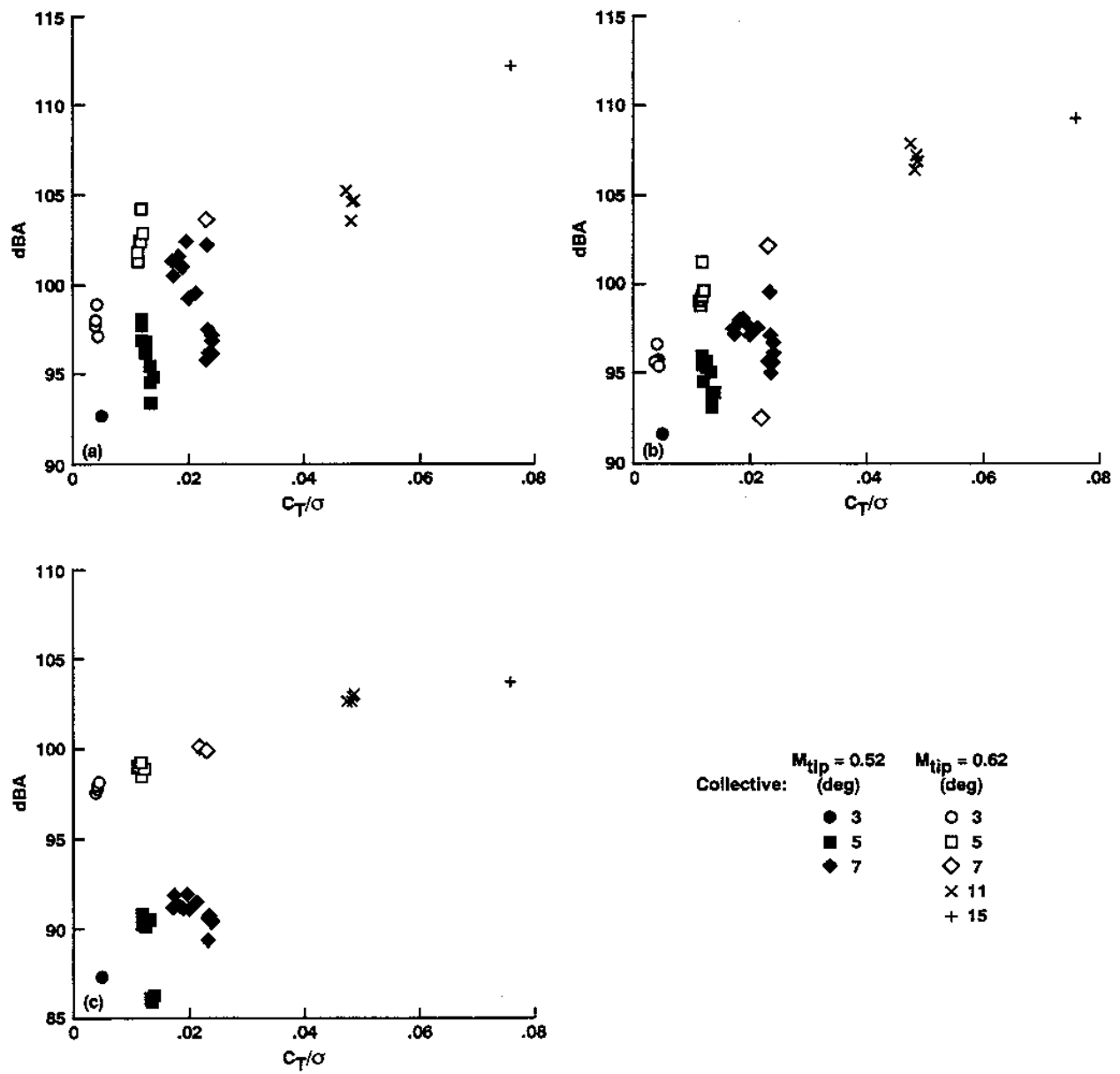


Figure 29. Measured sound level variation with C_T/s , near-field tower installed, grid not installed. (a) Microphone 2, (b) microphone 8, (c) microphone 6.

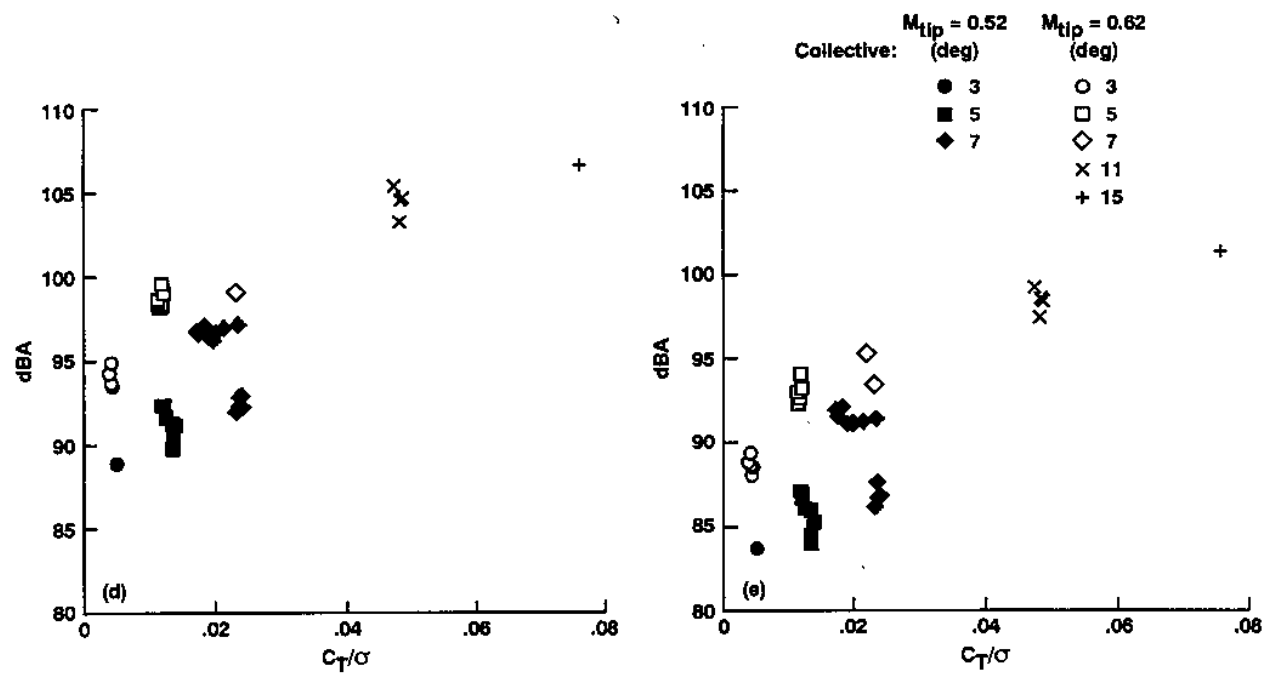


Figure 29 (concluded). (d) Microphone 9, (e) microphone 11.

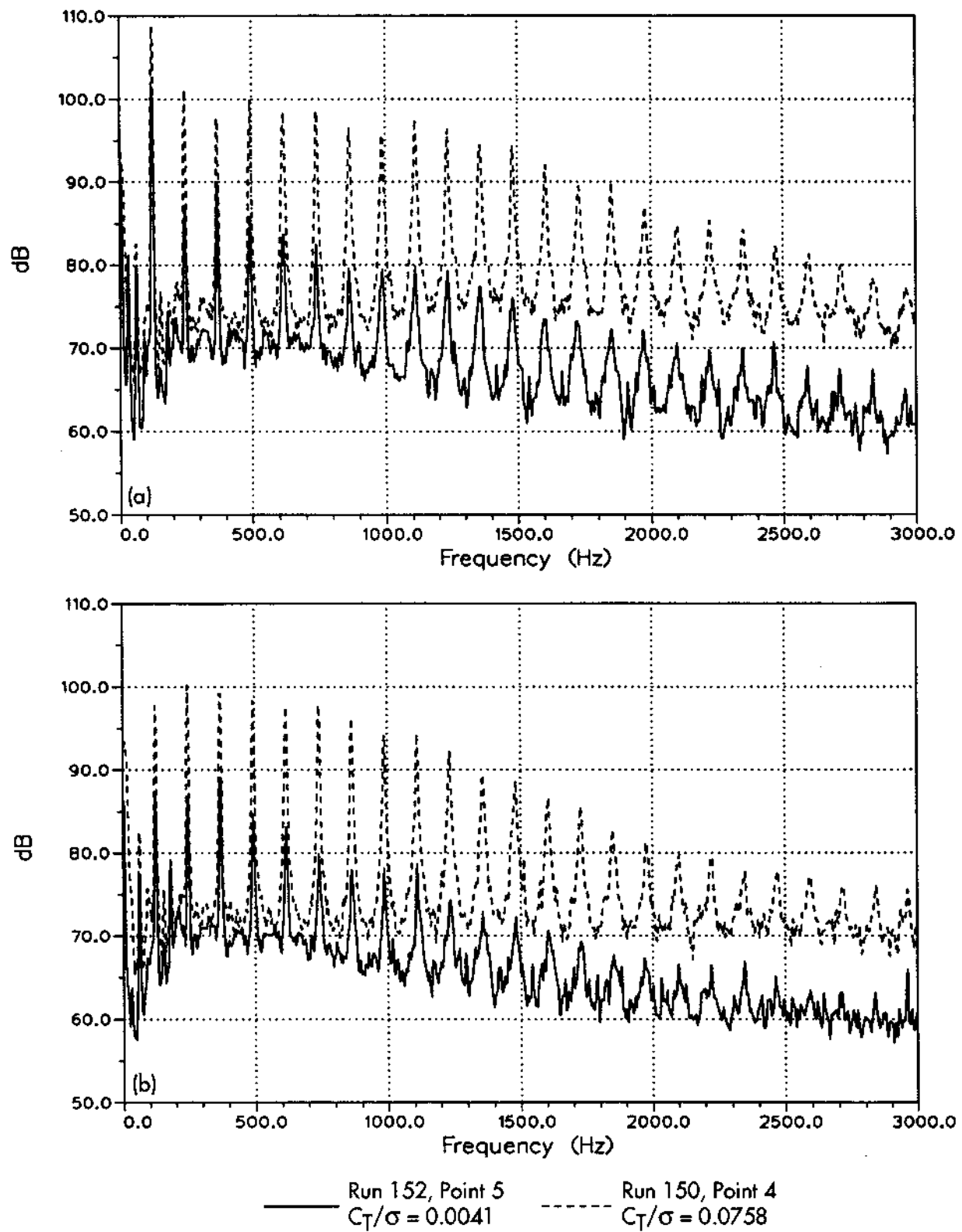


Figure 30. Effect of C_T/s on acoustic power spectra. Near-field tower installed, grid not installed. (a) Microphone 2, (b) microphone 8.

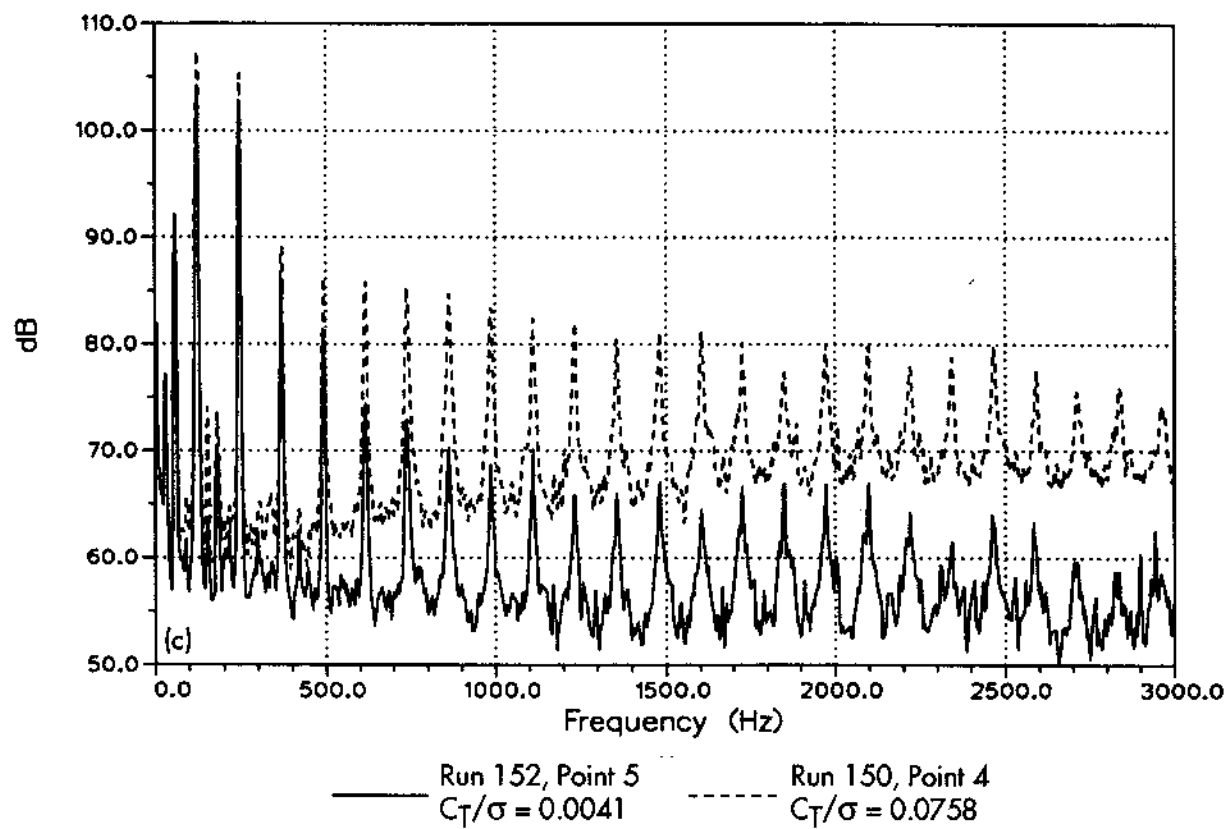


Figure 30 (continued). (c) Microphone 6.

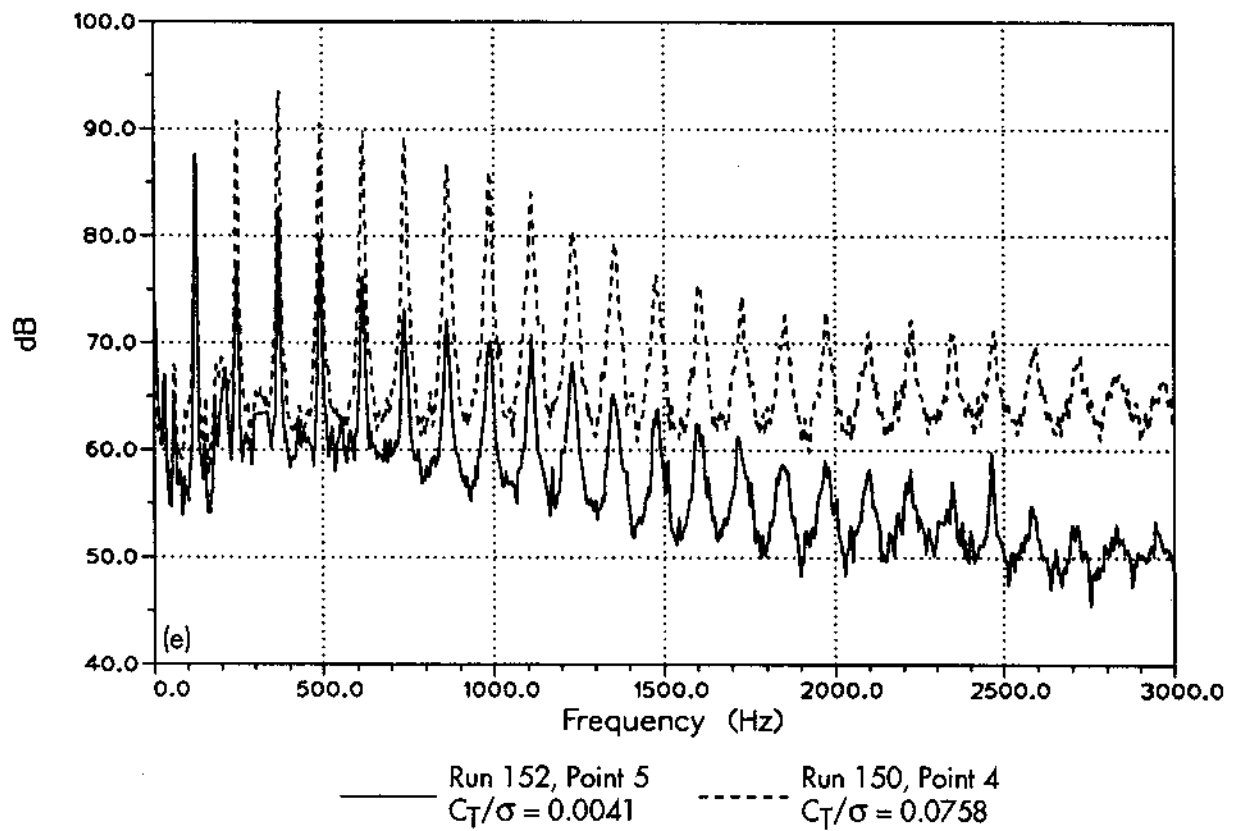
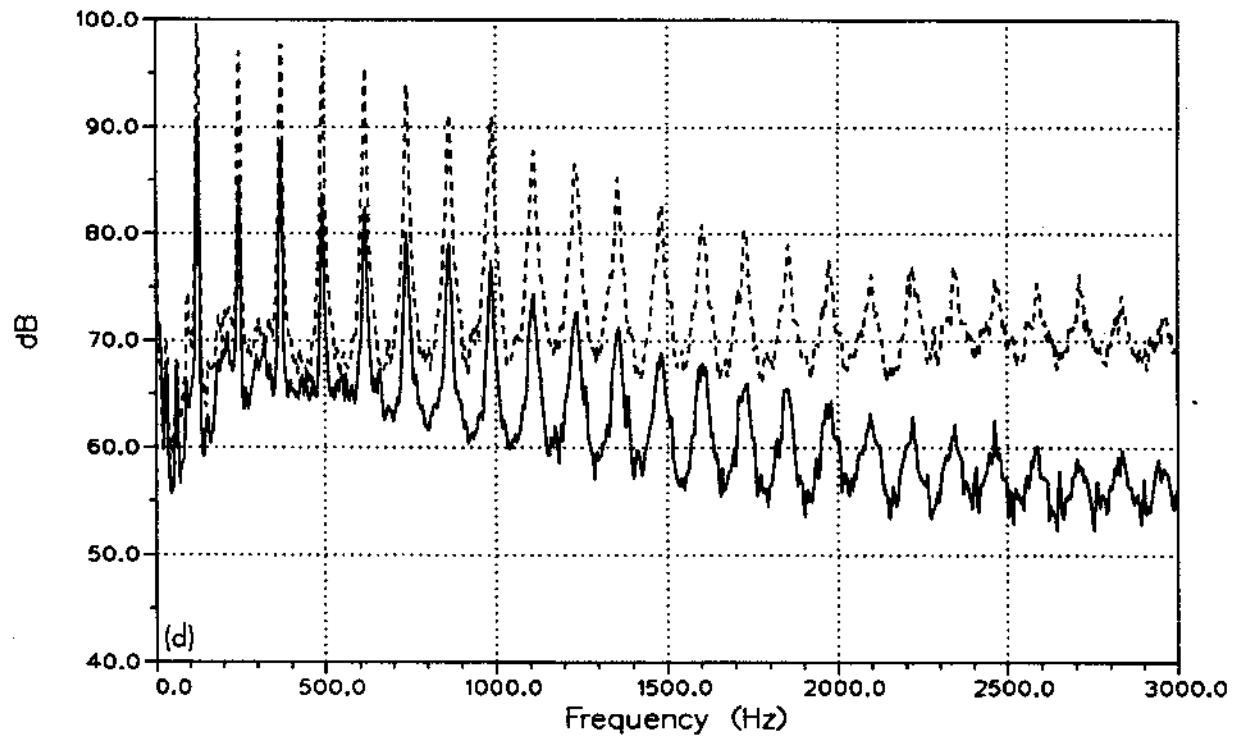


Figure 30 (concluded). (d) Microphone 9, (e) microphone 11.

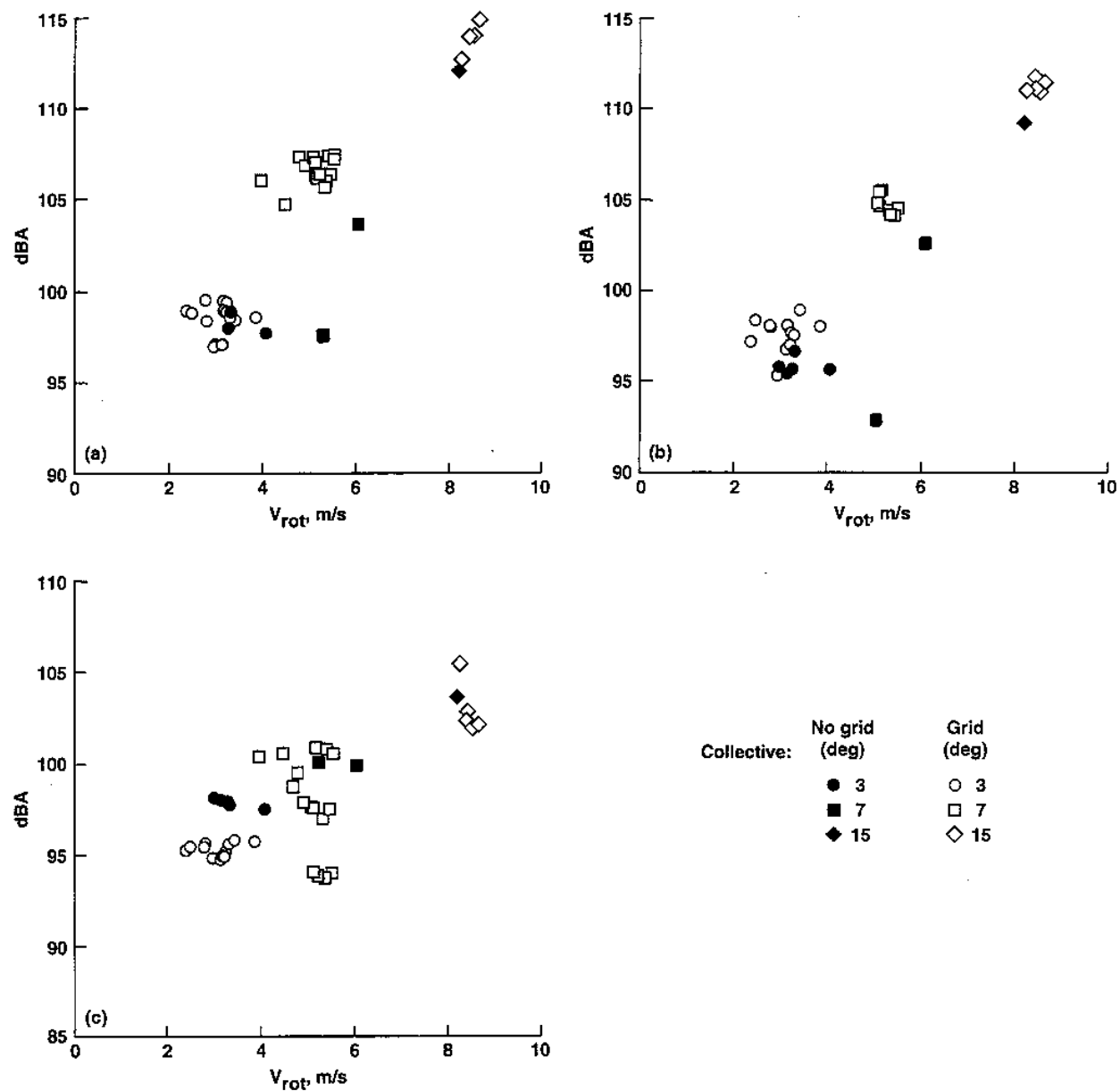


Figure 31. Effect of grid on measured sound level variation. Near-field tower installed. (a) Microphone 2, (b) microphone 8, (c) microphone 6.

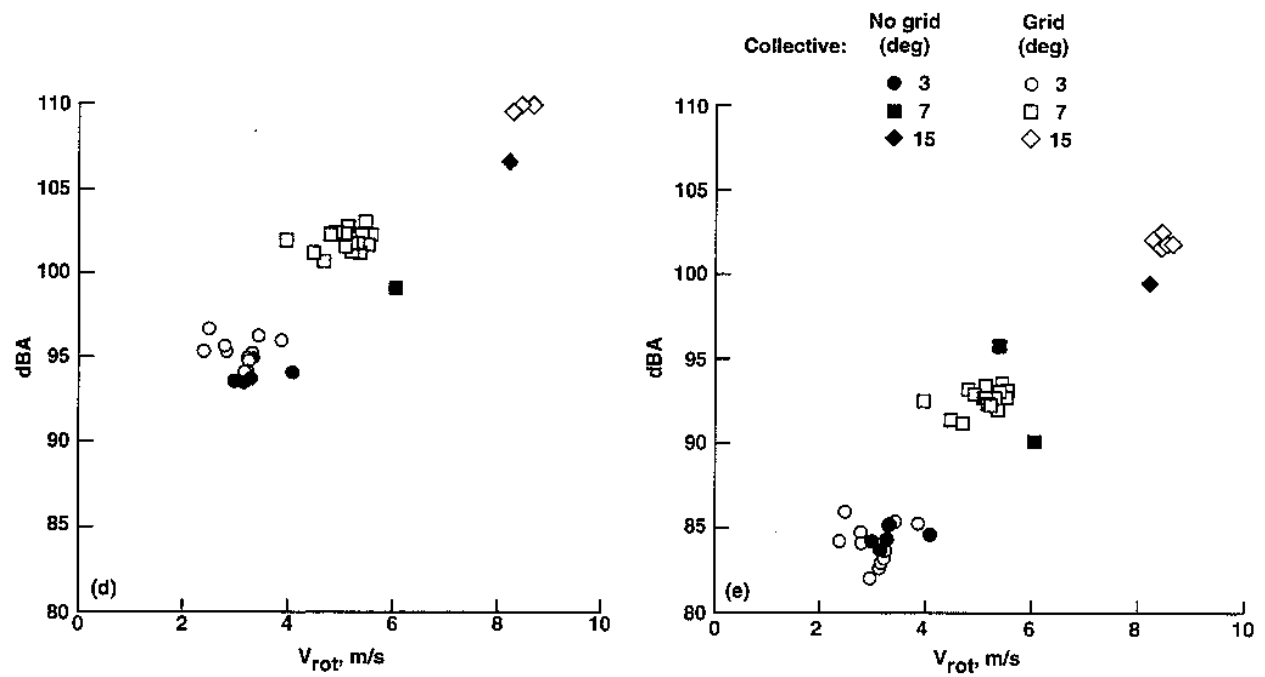


Figure 31 (concluded). (d) Microphone 9, (e) microphone 11.

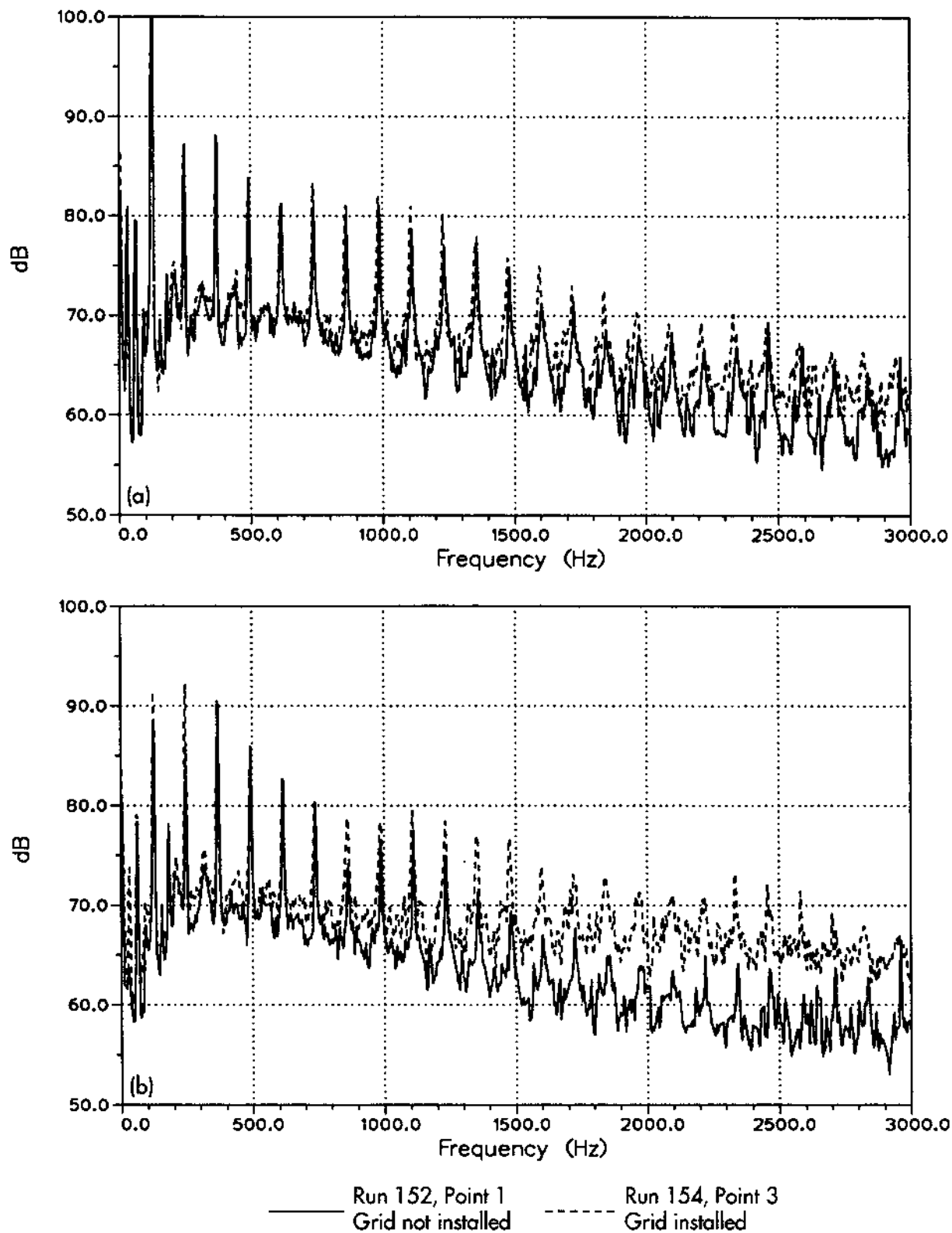


Figure 32. Effect of grid on acoustic power spectra for $\theta = 3^\circ$. Near-field tower installed. (a) Microphone 2, (b) microphone 8.

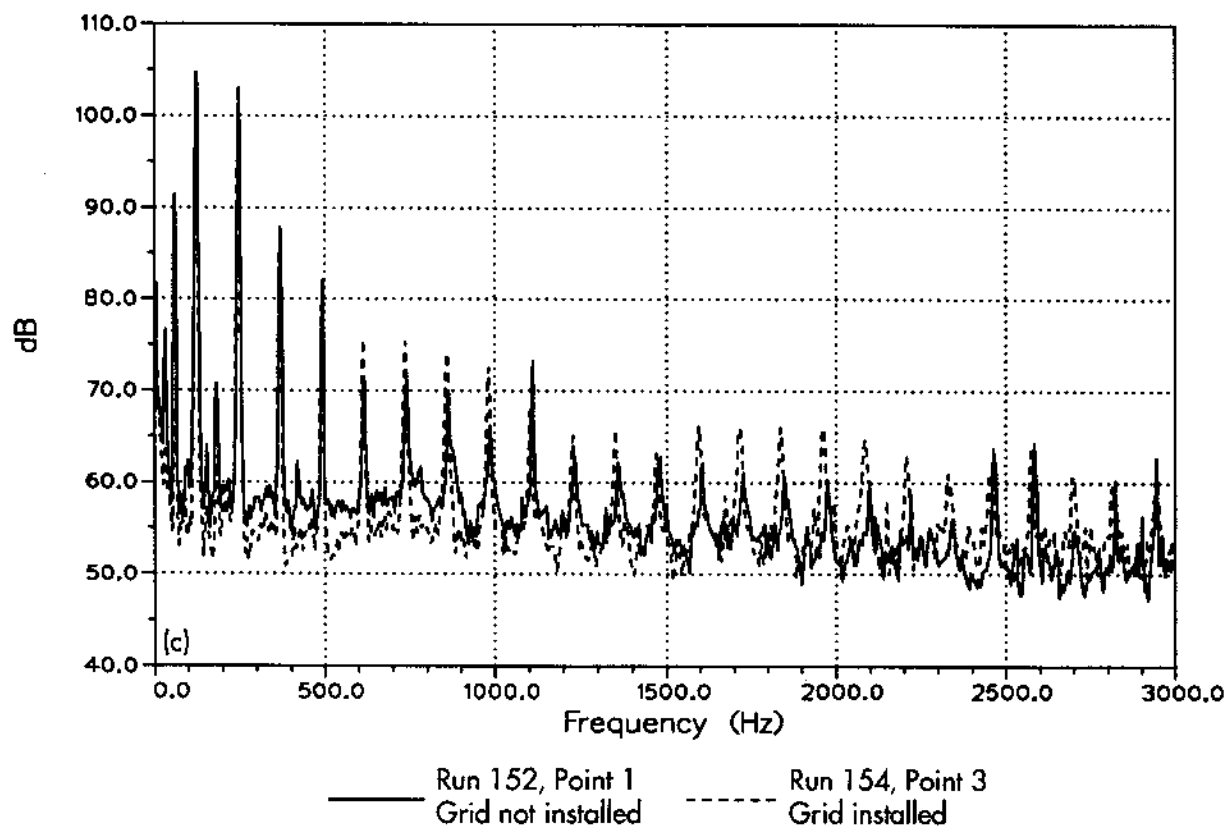


Figure 32 (continued). (c) Microphone 6.

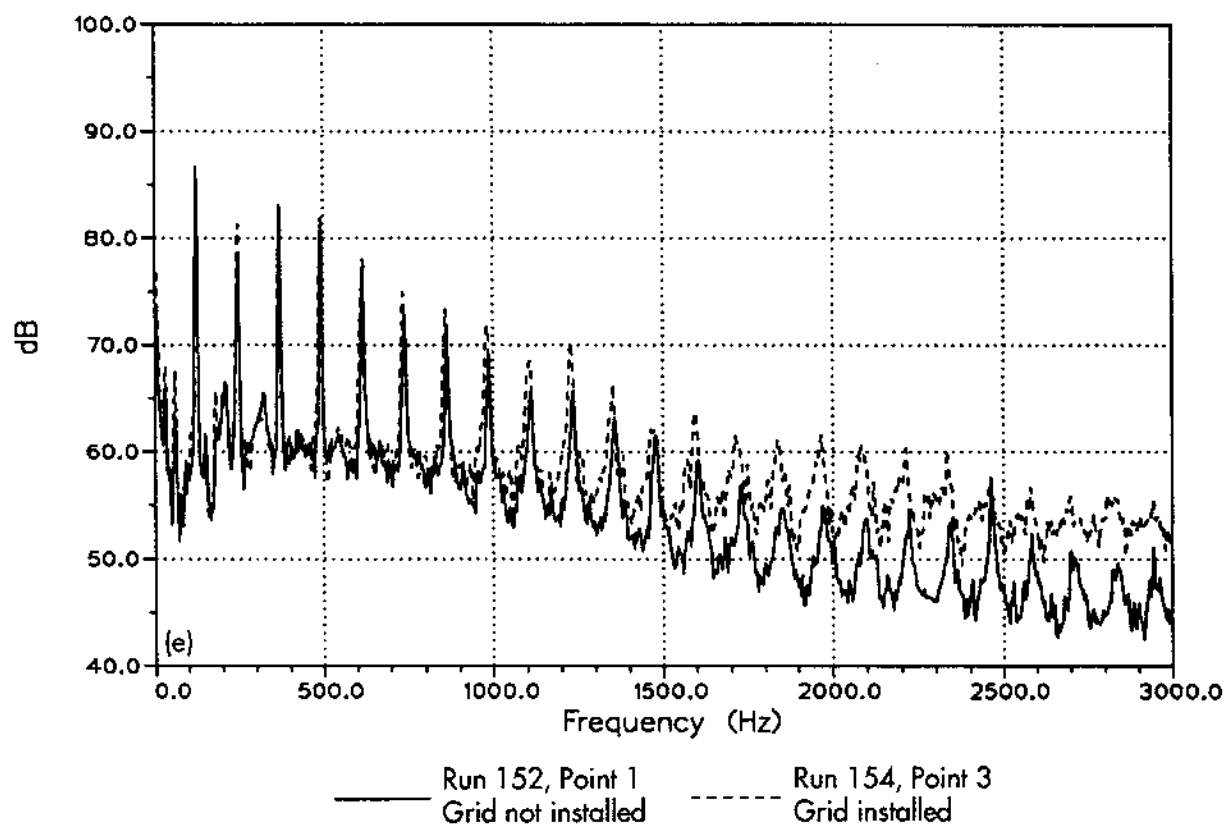
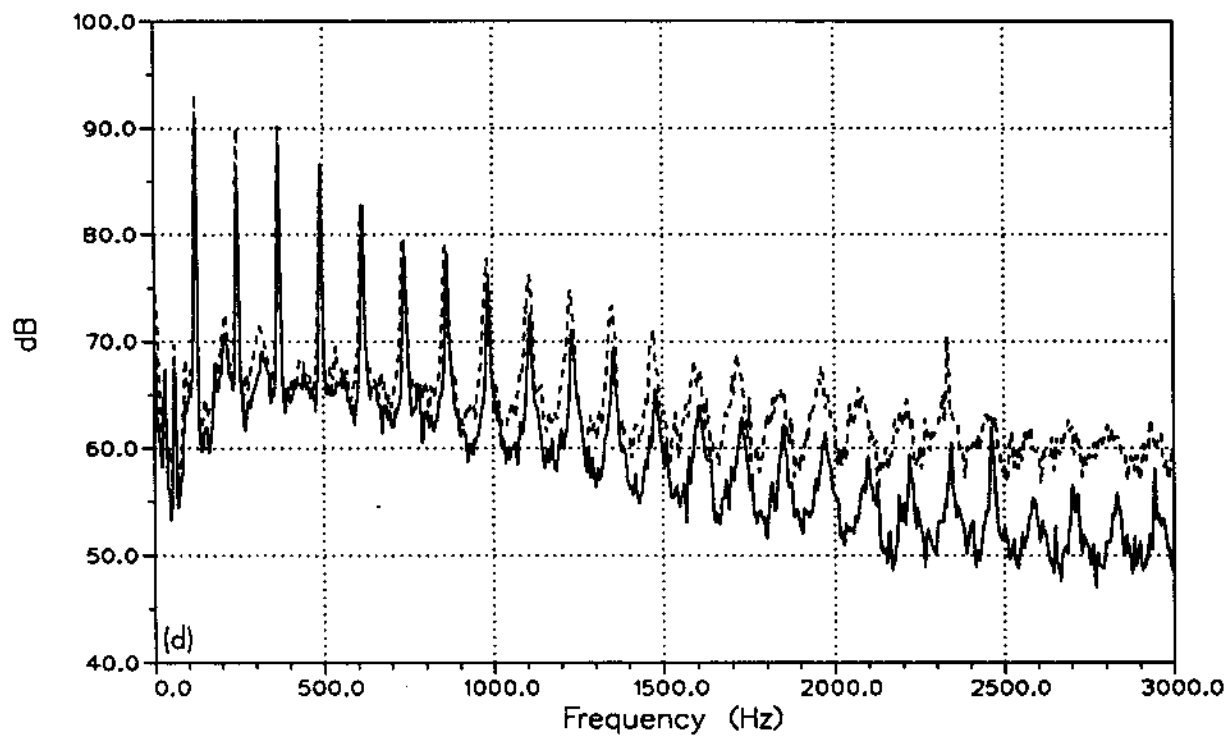


Figure 32 (concluded). (d) Microphone 9, (e) microphone 11.

REPORT DOCUMENTATION PAGE			Form Approved OMB No. 0704-0188	
Public reporting burden for this collection of information is estimated to average 1 hour per response, including the time for reviewing instructions, searching existing data sources, gathering and maintaining the data needed, and completing and reviewing the collection of information. Send comments regarding this burden estimate or any other aspect of this collection of information, including suggestions for reducing this burden, to Washington Headquarters Services, Directorate for Information Operations and Reports, 1215 Jefferson Davis Highway, Suite 1204, Arlington, VA 22202-4302, and to the Office of Management and Budget, Paperwork Reduction Project (0704-0188), Washington, DC 20503.				
1. AGENCY USE ONLY (Leave blank)		2. REPORT DATE September 1994		3. REPORT TYPE AND DATES COVERED Technical Memorandum
4. TITLE AND SUBTITLE Measurements of Atmospheric Turbulence Effects on Tail Rotor Acoustics			5. FUNDING NUMBERS 505-59-36	
6. AUTHOR(S) Martin J. Hagen,* Gloria K. Yamauchi, David B. Signor, and Marianne Mosher				
7. PERFORMING ORGANIZATION NAME(S) AND ADDRESS(ES) Ames Research Center Moffett Field, CA 94035-1000			8. PERFORMING ORGANIZATION REPORT NUMBER A-94122	
9. SPONSORING/MONITORING AGENCY NAME(S) AND ADDRESS(ES) National Aeronautics and Space Administration Washington, DC 20546-0001			10. SPONSORING/MONITORING AGENCY REPORT NUMBER NASA TM-108843	
11. SUPPLEMENTARY NOTES Point of Contact: Gloria K. Yamauchi, Ames Research Center, MS T12-B, Moffett Field, CA 94035-1000 (415) 604-6719 *California Polytechnic State University, San Luis Obispo, California				
12a. DISTRIBUTION/AVAILABILITY STATEMENT Unclassified — Unlimited Subject Category 02			12b. DISTRIBUTION CODE	
13. ABSTRACT (Maximum 200 words) Results from an outdoor hover test of a full-scale Lynx tail rotor are presented. The investigation was designed to further the understanding of the acoustics of an isolated tail rotor hovering out-of-ground effect in atmospheric turbulence, without the effects of the main rotor wake or other helicopter components. Measurements include simultaneous rotor performance, noise, inflow, and far-field atmospheric turbulence. Results with grid-generated inflow turbulence are also presented. The effects of atmospheric turbulence ingestion on rotor noise are quantified. In contradiction to current theories, increasing rotor inflow and rotor thrust were found to increase turbulence ingestion noise. This is the final report of Task 13A—Helicopter Tail Rotor Noise, of the NASA/United Kingdom Defense Research Agency cooperative Aeronautics Research Program.				
14. SUBJECT TERMS Measurements, Turbulence, Rotor acoustics			15. NUMBER OF PAGES 82	
			16. PRICE CODE A05	
17. SECURITY CLASSIFICATION OF REPORT Unclassified	18. SECURITY CLASSIFICATION OF THIS PAGE Unclassified	19. SECURITY CLASSIFICATION OF ABSTRACT	20. LIMITATION OF ABSTRACT	